

Contents

1	HI shells and super-shells	5
1.1	HI shells and super-shells in observations	5
1.2	Origin of the HI shells and super-shells	6
1.3	Triggered star formation	7
2	Theoretical models of expanding shells	9
2.1	The Sedov solution	9
2.2	Weaver's model of SWB	12
2.3	The thin-shell approximation	15
2.4	The self-gravitating thin shell	18
2.5	Numerical models	20
2.5.1	The thin-shell approximation	20
2.5.2	HD and MHD simulations	21
3	The gravitational instability	23
3.1	Fluid equations on the shell surface	23
3.2	Linear analysis	25
3.3	Solution with quadratic terms	29
3.4	The mass spectrum of fragments	33
4	The ZEUS code	39
4.1	Introduction	39
4.2	Basic equations	40
4.3	The HD algorithm	41
4.4	The coordinate system	43
4.5	Artificial viscosity	44
4.6	Boundary conditions	45
4.7	Time-step control	46
4.8	Radiative cooling	47
4.9	Heating	49
4.10	Additional pressure	50

4.11	Patches	51
5	Poisson solver	53
5.1	Overview of methods	53
5.2	Iterative methods	55
5.2.1	Problem definition	55
5.2.2	Basic iterative schemes	58
5.2.3	The convergence rate	60
5.2.4	The DADI method	62
5.3	The multigrid method	64
5.3.1	Basic ideas	64
5.3.2	Intergrid transfers	66
5.3.3	Multigrid schemes	67
5.3.4	Implementation of the multigrid method	69
6	Hydrodynamic model of the shell	71
6.1	The SHELL module	71
6.2	Expansion of 1D adiabatic bubble	73
6.2.1	The Sedov problem	73
6.2.2	Expanding adiabatic super-shell	74
6.3	Energy conservation	75
6.4	The thermal instability	78
6.5	1D self-gravitating expanding shell	80
7	Self-gravitating shells in 3D	83
7.1	1D to 3D transition	84
7.2	Perturbation growth in the linear regime	86
7.3	The mass spectrum of fragments	88
7.4	Conclusions	93

Introduction

In this work we study the formation of stars and galactic molecular clouds triggered by HI shells and super-shells. We investigate the gravitational instability evolving in these objects using the analytical and numerical models. The 3D numerical model is based on the hydrodynamic code ZEUS and the multigrid Poisson solver Šemík. Both analytical and numerical models are used to obtain the mass spectrum of fragments created by the gravitational instability. The obtained spectrum is compared to the initial mass function of stars and to the mass spectrum of Galactic giant molecular clouds.

The work is divided into seven chapters. In the first chapter we introduce the HI shells and super-shells, their observations and theories of their origin.

The second chapter deals with the theoretical models which describe the evolution of the expanding shells. The models are based either on the direct solution of the hydrodynamic equations or on the thin-shell approximation.

In the third chapter we present the theory of the gravitational instability of the expanding shell. We give the procedure of obtaining the mass spectrum of fragments and show the obtained spectra.

The ZEUS hydrocode, including our add-ons and modifications, is described by Chapter 4.

Chapter 5 describes the Poisson solver Šemík, which we have developed to compute the gravitational potential in the numerical model of the expanding shell. It is based on the multigrid method – one of the fastest and most progressive method of solving the elliptic equations.

The numerical model of the expanding shell is described in Chapter 6. It also includes the tests of the code against the analytical models.

In the last Chapter 7 we present the 3D numerical simulations of the expanding self-gravitating shell. We follow the evolution of the gravitational instability and compare it to the analytical results. Finally, we determine the mass spectrum of fragments.

Finally, we attach the published (or accepted) papers which includes the results presented in this work:

Wünsch, R., Palouš, J., 2001, *A&A*, 374, 746

- Wünsch, R., Palouš, J., 2001, in Dynamics of star clusters and the Milky Way, ed.: Deiters, S., Fuchs, B., Just, A., Spurzem, R., Wielen, R., San Francisco, ASP 228, 557
- Wünsch, R., Palouš, J., Ehlerová, S., 2003, in From Observations to Self-consistent Modelling of the ISM in Galaxies, eds. M. A. de Avillez, D. Breitschwerdt, Kluwer Acad. Publishers, in press
- Palouš, J., Ehlerová, S., Wünsch, R., 2003, in The Evolution of Galaxies III - From Simple Approaches to Self-consistent Models, eds. G. Hensler, G. Stasinska, S. Harfst, P. Kroupa, Ch. Theis, Kluwer Academic Publishers, Astrophysics and Space Science 284, 873

Chapter 1

HI shells and super-shells

1.1 HI shells and super-shells in observations

HI shells are structures in the neutral hydrogen in galaxies observed in the 21 cm line. They are regions of the low density surrounded by the dense thin shell. The scales of these objects are from 10 pc to 1 – 2 kpc. They may expand supersonically, with velocities up to several tens of km/s. The typical density in the cavity is by 3 – 4 orders less than the density of the ambient medium, the typical surface density of the shell is $10^{20} - 10^{22}$ hydrogen atoms per cm^2 . Their expansion energies are $10^{51} - 10^{54}$ ergs, objects with energy greater than 5×10^{52} ergs are referred as super-shells.

First HI shell in the Milky Way was discovered by Menon (1958). Later, many shells and super-shells were discovered by Heiles (1979, 1984, 1990) in the Weaver and Williams (1973) HI survey of the Milky Way. Among many recent observations of HI shells in the Milky Way we mention Ehlerová et al. (2001) and McClure-Griffiths et al. (2002). Ehlerová & Palouš (2003) apply the automatic search algorithm to the Leiden-Dwingeloo survey of the Milky Way (Hartmann & Burton, 1997) and found ~ 300 HI shells in the 2nd Galactic quadrant.

HI shells were also found in many of the nearby galaxies within 10 Mpc. Examples can be LMC (Kim et al. 1998), SMC (Stanimirovic et al., 1999), M 31 (Brinks & Bajaja, 1986), M 33 (Deul & den Hartog, 1990), Holmberg II (Puche et al., 1992), M 101 and NGC 6946 (Kamphuis, 1993) and IC 10 (Wilcots & Miller, 1998).

Fig. 1.1, left panel, shows the observation of the HI shell made by Ehlerová et al. (2001). We can see the hole surrounded by the dense wall. We should note that this is the ideal case – in many cases only an arc of the wall or no wall is observed. The shape of the real shells may be complicated, they

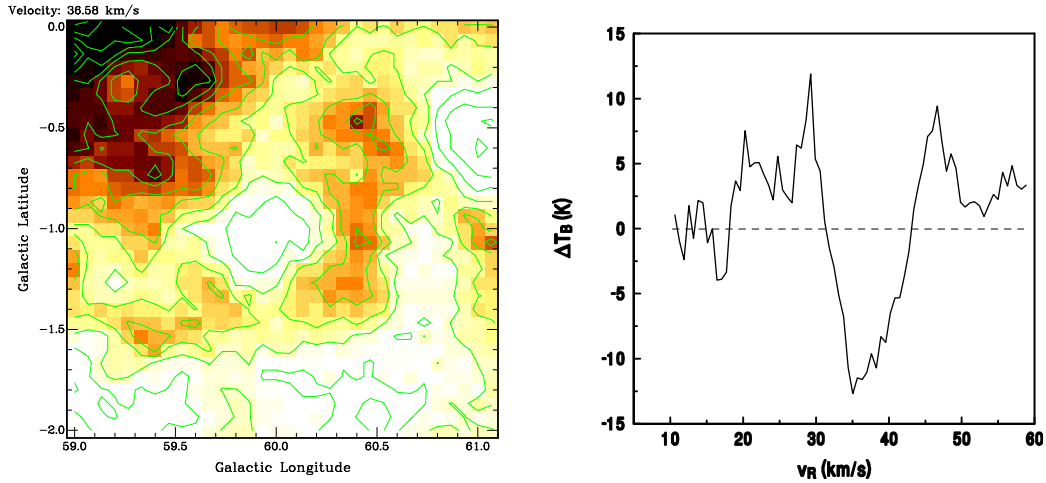


Figure 1.1: The galactic HI shell GS59.9-1.0+38 observed by Ehlerová et al (1997) with 100 m Effelsberg radiotelescope. Left: The lb -cut of the data-cube in velocity channel $v = 36.6$ km/s. Right: The spectrum through the centre of the shell. The average spectrum of the surrounding area was subtracted.

can even contain clouds inside the structure (real or only projected). This all makes their identification in the radio observation really difficult. The spectrum in the centre of the shell is shown by Fig. 1.1, right panel. The two distinct peaks (structure typical for the HI shell spectra) represent the front and back walls of the shell, the half of their distance is the expansion velocity.

Shapes of shells are affected by the spatial distribution of the ambient mass and by its possible motion (e.g. due to the galactic differential rotation). In galaxies with thin gaseous disks, for instance in rapidly rotating disk galaxies, the cylindrical, z -elongated structures may be formed. They are called *worms*. Some of these worms may break through the galactic disk and even open to the galactic halo – these ones are called *chimneys*. In this case the hot gas from the shell interior, which is enriched by metals made by stars, may escape to the galactic halo. This may be the way, how to explain the observed hot metal rich halo gas (Cox & Smith, 1974; McKee & Ostriker, 1977). Fig. 1.2 shows an example of the chimney.

1.2 Origin of the HI shells and super-shells

In the most common concept, HI shells are results of the shock waves created by a great amount of energy inserted into the interstellar medium (ISM). For

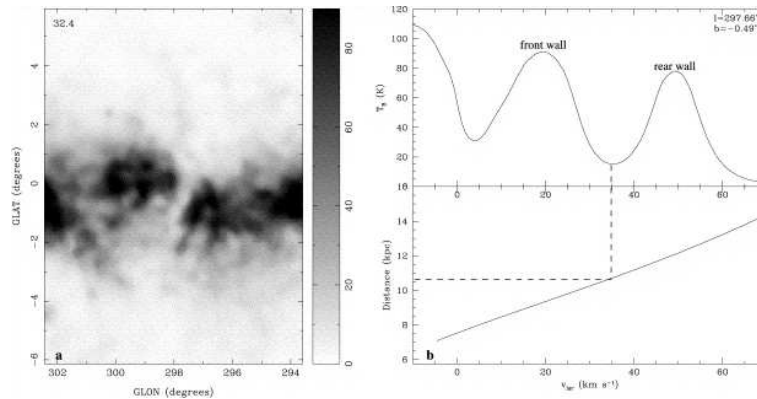


Figure 1.2: The chimney or worm GSH298-01+35 found by McClure-Griffiths et al (2002) in the Southern Galactic Plane Survey made by 64 m Parkes telescope. The kinematical distance of this structure is 10.5 kpc, its dimensions are 75 pc \times 1 kpc. Estimated energy required to create this object is 1.1×10^{52} ergs.

the review see Tenorio-Tagle & Bodenheimer (1988) or van der Hulst (1996). The smallest structures with energies $\sim 10^{51}$ ergs may be created by a single O- or B-type star with the powerful stellar wind (they are called stellar wind bubbles) or by a single supernovae explosion (i.e. they are later stages of the supernovae remnants). The OB-associations with 10-100 massive stars may be responsible for the larger shells and super-shells. These stars add with their stellar winds and SN explosions the energy into the cavity during a time period 10–20 Myr. The most energetic super-shells (with energy $> 10^{53}$ erg) may be formed by the group of several OB association with ~ 1000 young stars. Recently, also explosions connected to the gamma ray bursts (GRB) are considered (see Efremov et al.).

Alternative theories assume that the arc of the shell can be created by the encounter of the galactic HI disk with the high velocity cloud (HVC) or a dwarf galaxy (Tenorio-Tagle et al., 1987). This theory may explain the existence of the shell-like structures with high energies in locations, where other energy sources are difficult to find.

1.3 Triggered star formation

One of the most interesting thing about the HI shells is that they can trigger the star formation (see Elmegreen, 1998 for the review on the triggered star formation in general).

During the expansion into the ambient medium, new mass is accreted

to the shell while its expansion velocity and temperature are decreasing. At a certain time the efficiency of the radiative cooling in the shell rapidly grows and the shell collapses into the thin layer (Falle, 1981). The cold and thin shell may become gravitationally unstable and break into fragments (Elmegreen, 1994, Ehlerová et al., 1997).

The masses of these fragments depend, in particular, on the density of the ambient medium. In the typical density of the galactic ISM 1 hydrogen atom per cm^3 the fragments with masses $10^4 - 10^6 M_\odot$ are formed, which correspond to the masses of galactic molecular clouds. In densities $10^6 - 10^7$ hydrogen atoms per cm^3 , which can be found in the cores of molecular clouds, the gravitational instability creates the fragments with stellar masses $1 - 10^3 M_\odot$.

The HI shells, on the one hand, may be created by the young stars and the groups of stars; the gravitational instability of these shells, on the other hand, can trigger the new star formation. Thus, HI shells may be the mechanism which propagates the star formation in galaxies from one place to another. (Mueller & Arnett, 1976; Jungwirth & Palouš, 1994).

Chapter 2

Theoretical models of expanding shells

In this chapter we describe theoretical models of expanding shells. These models can be used in various scales, including supernovae remnants (SNR), stellar wind bubbles (SWB) and larger HI shells and super-shells – the objects which we are interested in.

In the first two sections we deal with the spherically symmetric analytical solutions of the hydrodynamic equations – the Sedov and Weaver solutions. We give a bit detailed description, this is because we use these solutions for the tests of our numerical model, and also due to the mathematical beauty of these self-similar solutions.

Section 2.3 deals with the thin-shell approximation, which describes the expansion of the thermally collapsed shell. This approach can also be used in numerical codes for simulations of the expanding shells in the more complicated physical situations.

Section 2.4 describes the models of the spherically symmetric thin shell with the self-gravity as described by Whitworth & Francis (2002).

In the last section we give the list of the several numerical simulations of the expanding shells. However, this list cannot be considered to be complete.

2.1 The Sedov solution

The Sedov solution is 1D analytical solution of hydrodynamic equations for the problem of an explosion. It was obtained by Sedov (1959) to describe the shock-wave spreading in the atmosphere after the explosion of an atomic bomb. Later, it was used by Straka (1973) and other authors to describe the second (energy conserving) phase of supernovae remnants. A detailed

discussion of the Sedov solution can be found in many texts (e.g. Shore, 1992; Bicknell, 2001), so we suggest only key points of its derivation.

Let us assume that energy E_0 is released in a homogeneous medium of density ρ_0 . If the amount of energy is sufficient, the spherical expanding shock is created. We search for the spherically symmetric solution of hydrodynamic equations, i.e. density ρ , radial velocity v and pressure p as functions of distance from the centre r and time t . The physical quantities have no characteristic values in such generally defined problem. Therefore, we can search for a solution in a *self-similar* form – the independent variables r and t are combined in one dimensionless parameter ξ and the hydrodynamic equations are solved for this parameter. A specific solution with a certain E_0 and ρ_0 in a certain time t can be then obtained by a simple scaling.

Since E_0 has dimensions ML^2T^{-2} and ρ_0 has dimensions ML^{-3} (M denotes mass, L length and T time), the dimensionless parameter ξ is

$$\xi = \beta \left(\frac{E_0}{\rho_0} \right)^{-1/5} r t^{-2/5}, \quad (2.1)$$

where β is a constant, which can be chosen so that the shock-front is at $\xi = 1$. Then, the position of the shock is given by the equation

$$r_{\text{sh}} = \beta^{-1} \left(\frac{E_0}{\rho_0} \right)^{1/5} t^{2/5} \quad (2.2)$$

and the shock expansion velocity is

$$v_{\text{sh}} = \frac{dr_{\text{sh}}}{dt} = \frac{2}{5} \beta^{-1} \left(\frac{E_0}{\rho_0} \right)^{1/5} t^{-3/5}. \quad (2.3)$$

If we use the polytropic equation of state $p \sim \rho^\gamma$, spherically symmetric hydrodynamic equations have a form

$$\begin{aligned} \frac{\partial \rho}{\partial t} + \frac{1}{r^2} \frac{\partial}{\partial r} (r^2 \rho v) &= 0 \\ \frac{\partial v}{\partial t} + v \frac{\partial v}{\partial r} + \frac{1}{\rho} \frac{\partial p}{\partial r} &= 0 \\ \frac{\partial}{\partial t} (p \rho^{-\gamma}) + v \frac{\partial}{\partial r} (p \rho^{-\gamma}) &= 0 \end{aligned} \quad (2.4)$$

We can replace the dependent variables $\rho(r, t)$, $v(r, t)$ and $p(r, t)$ by dimensionless variables G , U and Z defined by the relations

$$\rho = \rho_0 G(\xi), \quad v = \frac{2r}{5t} U(\xi), \quad c_s^2 = \frac{\gamma p}{\rho} = \frac{4r^2}{25t^2} Z(\xi), \quad (2.5)$$

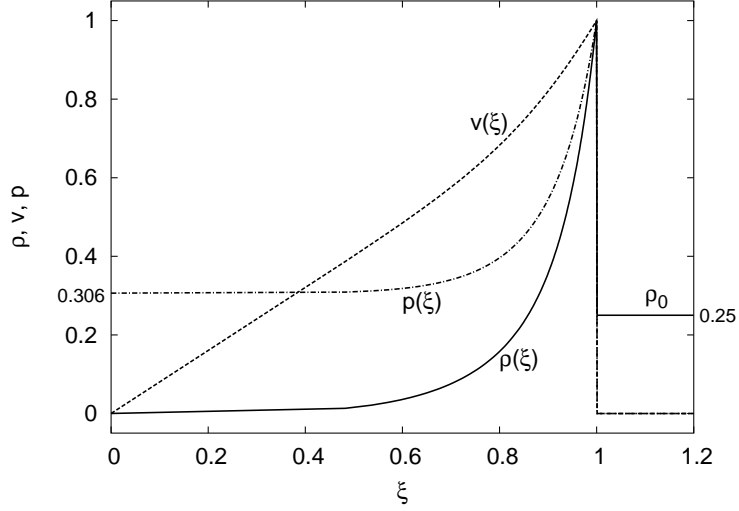


Figure 2.1: The Sedov solution.

which are functions of only one similarity variable ξ . The Eqs. 2.4 will take a form

$$\begin{aligned}
 (U - 1) \frac{d \ln G}{d \ln \xi} + \frac{dU}{d \ln \xi} + 3U &= 0 \\
 (U - 1) \frac{dU}{d \ln \xi} + U[U - 5/2] + Z \frac{d \ln G}{d \ln \xi} &= 0 \\
 \frac{d \ln Z}{d \ln \xi} - (\gamma - 1) \frac{d \ln G}{d \ln \xi} + \frac{2(U - 5/2)}{U - 1} &= 0.
 \end{aligned} \tag{2.6}$$

Boundary conditions at the shock are given by Rankine-Hugoniot conditions for the infinitely strong shock (e.g. Shore, 1992)

$$\rho_2 = \frac{\gamma + 1}{\gamma - 1} \rho_1, \quad v_2 = \frac{2}{\gamma + 1} v_{\text{sh}}, \quad p_2 = \frac{2}{\gamma + 1} \rho_1 v_{\text{sh}}^2 \tag{2.7}$$

where ρ_2 , v_2 and p_2 denote the post-shock quantities, while $\rho_1 \equiv \rho_0$ is the pre-shocked density. The boundary conditions in dimensionless variables have a form

$$U(1) = \frac{2}{\gamma + 1}, \quad G(1) = \frac{\gamma + 1}{\gamma - 1}, \quad Z(1) = \frac{2\gamma(\gamma - 1)}{(\gamma + 1)^2}. \tag{2.8}$$

The system 2.6 – 2.8 can be solved analytically, the explicit solution as given by Sedov (1972) has a form

$$\begin{aligned}
\frac{r}{r_2} &= \left[\frac{(\nu+2)(\gamma+1)}{4} V \right]^{-\frac{2}{2+\nu}} \left[\frac{\gamma+1}{\gamma-1} \left(\frac{(\nu+2)\gamma}{2} V - 1 \right) \right]^{-\alpha_2} \times \\
&\times \left[\frac{(\nu+2)(\gamma+1)}{(\nu+2)(\gamma+1) - 2[2+\nu(\gamma-1)]} \left(1 - \frac{2+\nu(\gamma-1)}{2} V \right) \right]^{-\alpha_1}, \\
\frac{v}{v_2} &= \frac{(\nu+2)(\gamma+1)}{4} V \frac{r}{r_2}, \\
\frac{\rho}{\rho_2} &= \left[\frac{\gamma+1}{\gamma-1} \left(\frac{(\nu+2)\gamma}{2} V - 1 \right) \right]^{\alpha_3} \left[\frac{\gamma+1}{\gamma-1} \left(1 - \frac{\nu+2}{2} V \right) \right]^{\alpha_5} \times \\
&\times \left[\frac{(\nu+2)(\gamma+1)}{(\nu+2)(\gamma+1) - 2[2+\nu(\gamma-1)]} \left(1 - \frac{2+\nu(\gamma-1)}{2} V \right) \right]^{\alpha_4}, \\
\frac{p}{p_2} &= \left[\frac{(\nu+2)(\gamma+1)}{4} V \right]^{-\frac{2\nu}{2+\nu}} \left[\frac{\gamma+1}{\gamma-1} \left(1 - \frac{\nu+2}{2} V \right) \right]^{\alpha_5+1} \times \\
&\times \left[\frac{(\nu+2)(\gamma+1)}{(\nu+2)(\gamma+1) - 2[2+\nu(\gamma-1)]} \left(1 - \frac{2+\nu(\gamma-1)}{2} V \right) \right]^{\alpha_4-2\alpha_1},
\end{aligned} \tag{2.9}$$

where ν is the dimension of space in which the explosion occurs (in this case $\nu = 3$). V is the parameter which takes values from $2/(\gamma(\nu+2))$ (centre of the explosion) to $4/((\nu+2)(\gamma+1))$ (the shock-front). Constants $\alpha_1 - \alpha_7$ have values

$$\begin{aligned}
\alpha_1 &= \frac{(\nu+2)\gamma}{2+\nu(\gamma-1)} \left[\frac{2\nu(2-\gamma)}{\gamma(\nu+2)^2} - \alpha_2 \right], & \alpha_2 &= \frac{1-\gamma}{2(\gamma-1)+\nu}, \\
\alpha_3 &= \frac{\nu}{2(\gamma-1)+\nu}, & \alpha_4 &= \frac{\alpha_1(\nu+2)}{2-\gamma}, \\
\alpha_5 &= \frac{2}{\gamma-2}, & \alpha_6 &= \frac{\gamma}{2(\gamma-1)+\nu}, \\
\alpha_7 &= \frac{[2+\nu(\gamma-1)]\alpha_1}{\nu(2-\gamma)}.
\end{aligned} \tag{2.10}$$

The Sedov solution 2.9 with $\nu = 3$ and $\gamma = 5/3$ is shown by Fig. 2.1. The constant β can be obtained by the numerical integration (see e.g. Bicknell, 2001). For $\gamma = 5/3$ it has a value

$$\beta \doteq 0.868. \tag{2.11}$$

2.2 Weaver's model of SWB

The semi-analytical model of the expanding shell with the continuous energy input was developed by Castor et al. (1975) and Weaver et al. (1977) for the case of stellar wind bubble (SWB). The authors assume an early type star which blows a steady, spherically symmetric stellar wind which interacts

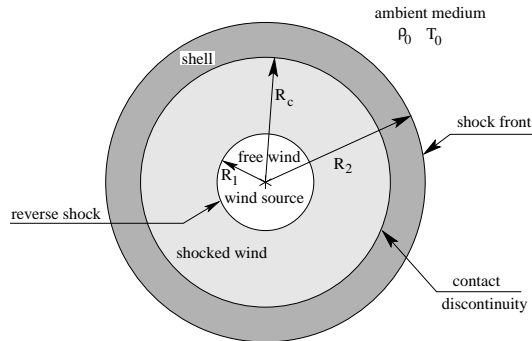


Figure 2.2: Structure of the stellar wind bubble as described in Weaver et al. (1977).

with the homogeneous interstellar medium of density ρ_0 . The mechanical luminosity of the wind L_w is given as

$$L_w = \frac{1}{2} \frac{dM_w}{dt} V_w^2, \quad (2.12)$$

where V_w and dM_w/dt are the constant terminal velocity and mass-loss rate of the wind, respectively.

The stellar wind creates the structure which is suggested by Fig. 2.2. It consists of four distinct regions: a free wind region (a), a shocked stellar wind region (b), a shell of shocked interstellar gas (c) and an ambient interstellar medium (d). The evolution of the bubble may be divided into three stages: in the initial, adiabatic stage the bubble expands so fast that the radiative cooling is unimportant; in the second stage the radiative loss from the shell causes it to collapse into a thin layer; and in the third stage the radiative cooling in region (b) starts to be important affecting the dynamics of the whole bubble. In this section we are interested in particular in the first adiabatic stage where the solution is self-similar and can be easily scaled to the problem of the expanding super-shell. In Section 6.2.2, we use it to test our numerical model. The self-similar solution exists also in the second stage, it is described in the following section on the thin-shell approximation.

The hydrodynamic equations, which describe the problem are the same as the Eqs. 2.4 describing the Sedov problem. The dimensionless self-similar variable, which is composed of independent variables r and t and problem parameters L_w and ρ_0 , has a form

$$\xi = \beta \left(\frac{L_w}{\rho_0} \right)^{-1/5} r t^{-3/5}, \quad (2.13)$$

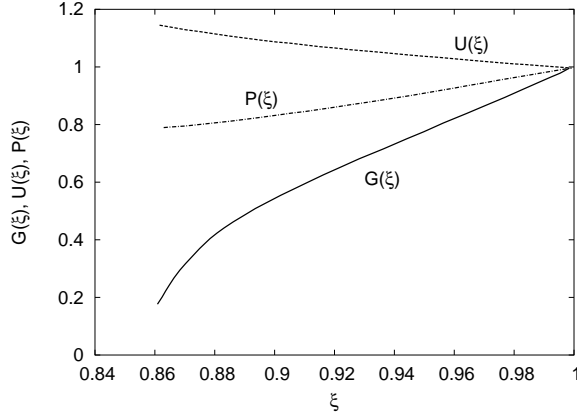


Figure 2.3: Radial distributions of the normalised density, velocity and pressure in the shell given by the set of Eqs. 2.17. The figure was taken from Weaver et al., 1977.

where β is a constant of order of unity which can be chosen so, that shock-front is at the position $\xi = 1$. Then we get

$$R_2(t) = \beta^{-1} \left(\frac{L_w}{\rho_0} \right)^{1/5} t^{3/5} \quad (2.14)$$

and

$$V_2(t) = \frac{dR_2}{dt} = \frac{3}{5} \beta^{-1} \left(\frac{L_w}{\rho_0} \right)^{1/5} t^{-2/5} . \quad (2.15)$$

If we define the dimensionless variables $G(\xi)$, $U(\xi)$ and $P(\xi)$ by relations

$$\rho(r, t) = \rho_0 G(\xi), \quad v(r) = V_2 U(\xi), \quad p(r) = \rho_0 V_2^2 P(\xi) , \quad (2.16)$$

the set of hydrodynamic equations will take a form

$$\begin{aligned} 3(U - \xi)U' - 2U + 3P'/G &= 0 \\ (U - \xi)G'/G + U' + 2U/\xi &= 0 \\ 3(U - \xi)P' - 3\gamma P(U - \xi)G'/G - 4P &= 0 \end{aligned} \quad (2.17)$$

Using the Rankine-Hugoniot conditions for the strong shock ($G(1) = 4$, $U(1) = 3/4$, and $P(1) = 3/4$), the eqs. 2.17 can be solved numerically in region (c) (the solution can be found in Weaver et al., 1977). The remarkable

property of the solution is that the function $G(\xi)$ drops suddenly to zero at $\xi_c = 0.86$, determining the position of the contact discontinuity (see Fig. 2.3). The solution in region (c) is self-similar, bounded by the shock-front at R_2 and the contact discontinuity at

$$R_c = 0.86R_2 . \quad (2.18)$$

The numerical integration shows that the constant β has a value

$$\beta \doteq 1.14 \quad (2.19)$$

for the polytropic index $\gamma = 5/3$.

The solution in region (b) is not self-similar (the ratio R_1/R_c does not remain constant during the evolution), but it is possible to obtain an analytical solution using some approximations (see Weaver et al., 1977) – the position of the reverse shock R_1 is determined by the balance between ram pressure of the stellar wind and the internal energy density in region (b). The most interesting property of this solution is that the region is almost isobaric, with the steady flow of mass.

The Weaver's model gives also the energy fractions in particular regions. They remain constant during the whole adiabatic stage. In region (b) the kinetic energy is negligible and internal energy is

$$E_b = \frac{5}{11}L_w t \quad (2.20)$$

and in region (c) the total energy is

$$E_c = \frac{6}{11}L_w t , \quad (2.21)$$

which is the work done across the contact discontinuity surface up to the time t . The numerical integration of the solution of the system 2.17 shows that 40.4% of E_c is the kinetic energy and 59.6% is the internal energy.

2.3 The thin-shell approximation

Let us assume a spherically symmetric infinitesimally thin shell of radius r_{sh} expanding with velocity v_{sh} into the homogeneous medium of density ρ_0 . The energy can be inserted either initially (initial explosion with energy E_0), or continuously with rate L . If we neglect the gravity, the momentum equation for the shell has a form

$$\frac{d}{dt}(m_{\text{sh}}v_{\text{sh}}) = 4\pi r_{\text{sh}}^2(P_{\text{int}} - P_{\text{ext}}) , \quad (2.22)$$

where $m_{\text{sh}} = 4/3\pi r_{\text{sh}}^3\rho_0$ is the mass of the shell, P_{int} and P_{ext} are pressures in the shell interior and the ambient medium, respectively. Neglecting the external pressure P_{ext} and assuming the isobaric shell interior with the pressure given by the equation of state in a form

$$P_{\text{int}} = \frac{2}{3} \frac{E_{\text{th}}}{V} , \quad (2.23)$$

where E_{th} is the thermal energy in the shell interior of the volume $V = 4/3\pi r_{\text{sh}}^3$, the Eq. 2.22 will take a form

$$r_{\text{sh}}^3(3\dot{r}_{\text{sh}}^2 + r_{\text{sh}}\ddot{r}_{\text{sh}}) = \frac{3E_{\text{th}}}{2\pi\rho_0} , \quad (2.24)$$

where dots denote derivatives with respect to time. A solution of Eq. 2.24 is a power-law in a form

$$r_{\text{sh}} = at^b , \quad (2.25)$$

where a and b are constants to be determined. Inserting Eq. 2.25 into Eq. 2.24 we get

$$a^5b(4b-1)t^{5b-2} = \frac{3E_{\text{th}}}{2\pi\rho_0} . \quad (2.26)$$

The classical infinitesimally thin-shell approximation (see e.g. Ehlerová, 2000) assumes that the total energy of the system is conserved (i.e. the radiative cooling of the shell has no effect on the shell dynamics) and consists of only the thermal energy of the shell interior and the kinetic energy of the shell

$$E_{\text{tot}} = E_{\text{th}} + \frac{1}{2}m_{\text{sh}}v_{\text{sh}}^2 . \quad (2.27)$$

If we insert this relation in Eq. 2.26, we get

$$a^5[5b^2 - 2]t^{5b-2} = \frac{3E_{\text{tot}}}{2\pi\rho_0} . \quad (2.28)$$

In the case of the abrupt energy input $E_{\text{tot}} \equiv E_0$ is simply the energy of the initial explosion. The constants a and b can be easily determined from Eq. 2.28 by demanding the LHS to be independent on time. The solution of Eq. 2.22 has a form

$$\begin{aligned}
r_{\text{sh}} &= \left(\frac{15}{4\pi}\right)^{1/5} \left(\frac{E_0}{\rho_0}\right)^{1/5} t^{2/5} \\
v_{\text{sh}} &= \frac{2}{5} \left(\frac{15}{4\pi}\right)^{1/5} \left(\frac{E_0}{\rho_0}\right)^{1/5} t^{-3/5}
\end{aligned} \tag{2.29}$$

and in astrophysical units

$$\begin{aligned}
r_{\text{sh}} &= 72.2 \left(\frac{E_0}{10^{51} \text{ erg}}\right)^{1/5} \left(\frac{\mu}{1.3 \text{ cm}^{-3}} \frac{n_0}{\text{cm}^{-3}}\right)^{-1/5} \left(\frac{t}{\text{Myr}}\right)^{2/5} \text{ pc} \\
v_{\text{sh}} &= 28.2 \left(\frac{E_0}{10^{51} \text{ erg}}\right)^{1/5} \left(\frac{\mu}{1.3 \text{ cm}^{-3}} \frac{n_0}{\text{cm}^{-3}}\right)^{-1/5} \left(\frac{t}{\text{Myr}}\right)^{-3/5} \text{ km s}^{-1} .
\end{aligned} \tag{2.30}$$

The thermal energy in the shell interior remains constant and has a value $E_{\text{th}} = \frac{3}{5}E_0$.

In the case of the continuous energy input, where $E_{\text{tot}} = Lt$, has the solution of Eq. 2.22 a form

$$\begin{aligned}
r_{\text{sh}} &= \left(\frac{5}{4\pi}\right)^{1/5} \left(\frac{L}{\rho_0}\right)^{1/5} t^{3/5} \\
v_{\text{sh}} &= \frac{3}{5} \left(\frac{5}{4\pi}\right)^{1/5} \left(\frac{L}{\rho_0}\right)^{1/5} t^{-2/5}
\end{aligned} \tag{2.31}$$

and in astrophysical units

$$\begin{aligned}
r_{\text{sh}} &= 57.9 \left(\frac{L}{10^{51} \text{ erg Myr}^{-1}}\right)^{1/5} \left(\frac{\mu}{1.3 \text{ cm}^{-3}} \frac{n_0}{\text{cm}^{-3}}\right)^{-1/5} \left(\frac{t}{\text{Myr}}\right)^{3/5} \text{ pc} \\
v_{\text{sh}} &= 34.0 \left(\frac{L}{10^{51} \text{ erg Myr}^{-1}}\right)^{1/5} \left(\frac{\mu}{1.3 \text{ cm}^{-3}} \frac{n_0}{\text{cm}^{-3}}\right)^{-1/5} \left(\frac{t}{\text{Myr}}\right)^{-2/5} \text{ km s}^{-1} .
\end{aligned} \tag{2.32}$$

The thermal energy in the shell interior is the constant fraction of the total energy $E_{\text{th}} = \frac{7}{10}Lt$.

In Weaver (1977) the thermal energy in the shell interior is determined from the equation

$$\frac{dE_{\text{th}}}{dt} = L - 4\pi r_{\text{sh}}^2 P_{\text{int}} \frac{dr_{\text{sh}}}{dt} , \tag{2.33}$$

where the second term on the RHS has the meaning of the work done by the shell. Eqs. 2.22, 2.23 and 2.33 have a solution

$$\begin{aligned} r_{\text{sh}} &= \left(\frac{250}{308\pi}\right)^{1/5} \left(\frac{L}{\rho_0}\right)^{1/5} t^{3/5} \\ v_{\text{sh}} &= \frac{3}{5} \left(\frac{250}{308\pi}\right)^{1/5} \left(\frac{L}{\rho_0}\right)^{1/5} t^{-2/5} \\ E_{\text{th}} &= \frac{5}{11}Lt, \quad E_{\text{kin,sh}} = \frac{15}{77}Lt, \quad E_{\text{th,sh}} = \frac{27}{77}Lt, \end{aligned} \quad (2.34)$$

where $E_{\text{kin,sh}}$ and $E_{\text{th,sh}}$ are the kinetic and thermal energies of the shell.

Note that this solution is almost the same as the solution of the hydrodynamic equations in the case of the adiabatic expanding bubble. The only difference is the constant β (see Eq. 2.14), which has changed from $\beta = 1.14$ to $\beta = 1.32$.

2.4 The self-gravitating thin shell

The Weaver's solution for the infinitesimally thin shell (Eq. 2.34) was extended to the effect of self-gravity by Whitworth & Francis, 2002. They use the same model of the thin shell of radius r_{sh} expanding with velocity v_{sh} into the homogeneous medium of density ρ_0 . The energy is inserted continuously with rate L . The energy conservation law is the same as in Eq. 2.33

$$\frac{d}{dt} \left(\frac{3}{2} P_{\text{int}} V \right) = L - P_{\text{int}} S v_{\text{sh}}, \quad (2.35)$$

where $S = 4\pi r_{\text{sh}}^2$ and $V = \frac{4}{3}\pi r_{\text{sh}}^3$ denote the surface and volume of the shell, P_{int} is the pressure in the shell interior.

The momentum equation has a form

$$\frac{d}{dt} (m_{\text{sh}} v_{\text{sh}}) = S P_{\text{int}} - \frac{G m_{\text{sh}}^2}{2r_{\text{sh}}^2}, \quad (2.36)$$

where $m_{\text{sh}} = \rho_0 V$ is the mass of the shell. The second term on the RHS is the radial gravitational force which decelerates the expansion. The factor 1/2 comes from the averaging of the gravitational force experienced by the individual layers of the shell (the inner layer experiences zero gravitational force, while the outer one is decelerate by the force $Gm_{\text{sh}}/r_{\text{sh}}^2$).

If we express the pressure in the shell interior from Eq. 2.36, we get

$$P_{\text{int}} = \rho_0 \left(\frac{r_{\text{sh}} \ddot{r}_{\text{sh}}}{3} + \dot{r}_{\text{sh}}^2 + \frac{2\pi G \rho_0 r_{\text{sh}}^2}{9} \right) \quad (2.37)$$

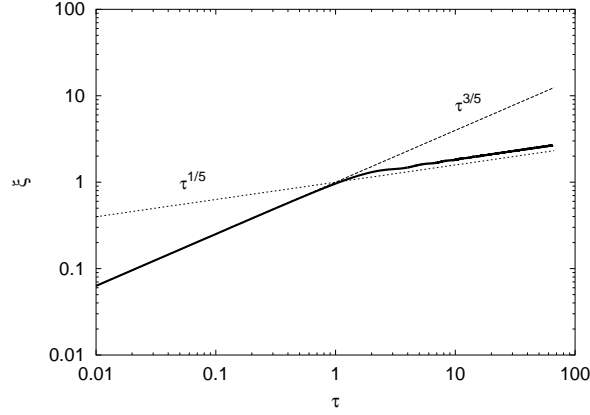


Figure 2.4: The solution of Eq. 2.41 (the thick line).

and

$$\frac{dP_{\text{int}}}{dt} = \rho_0 \left(\frac{r_{\text{sh}} \ddot{r}_{\text{sh}}}{3} + \frac{7\dot{r}_{\text{sh}} \ddot{r}_{\text{sh}}}{3} + \frac{4\pi G \rho_0 r_{\text{sh}} \dot{r}_{\text{sh}}}{9} \right), \quad (2.38)$$

where dots denote the time derivatives. By inserting Eqs. 2.37 and 2.38 into Eq. 2.35 we get

$$r_{\text{sh}}^4 \ddot{r}_{\text{sh}} + 12r_{\text{sh}}^3 \dot{r}_{\text{sh}} \ddot{r}_{\text{sh}} + 15r_{\text{sh}}^2 \dot{r}_{\text{sh}}^3 + \frac{14\pi G \rho_0 r_{\text{sh}}^4 \dot{r}_{\text{sh}}}{3} = \frac{3L}{2\pi \rho_0}. \quad (2.39)$$

If we define the dimensionless variables

$$\begin{aligned} \tau &= \frac{t}{t_0}, & t_0 &= \left(\frac{3\pi}{32G\rho_0} \right)^{1/2}, \\ \xi &= \frac{r_{\text{sh}}}{r_0}, & r_0 &= \left(\frac{2000GL}{231\pi^2} \right)^{1/5} t_0, \end{aligned} \quad (2.40)$$

the Eq. 2.39 simplifies to a form

$$\xi^4 \ddot{\xi} + 12\xi^3 \dot{\xi} \ddot{\xi} + 15\xi^2 \dot{\xi}^3 + \frac{7\pi^2}{16} \xi^4 \dot{\xi} = \frac{231}{125}. \quad (2.41)$$

This equation can be solved numerically, the solution is shown by Fig. 2.4. In the initial period of the evolution (for $t \ll t_0$), the gravity is unimportant (the last term in Eq. 2.36 is small) and the solution follows the Weaver's thin-shell solution

$$\xi = \tau^{3/5} \quad \rightarrow \quad r_{\text{sh}} = \left(\frac{125Lt^3}{154\pi\rho_0} \right)^{1/5}. \quad (2.42)$$

Later, when $t \gg t_0$, the gravitational term in the Eq. 2.36 dominates, and the solution of the Eq. 2.41 can be approximated by

$$\xi = \left(\frac{528\tau}{25\pi^2} \right)^{1/5} \rightarrow r_{\text{sh}} = \left(\frac{45Lt}{28\pi^2 G\rho_0} \right)^{1/5}, \quad (2.43)$$

which can be obtained by neglecting the pressure term in Eq. 2.36. As we can see, the expansion of the shell is substantially decelerated.

2.5 Numerical models

There are many works which use numerical codes to model the problem of the expanding shell, some of them are mentioned in this section. Most of the codes can be divided in two groups: the first uses the thin-shell approximation, the others are the hydrodynamic or magnetohydrodynamic codes.

2.5.1 The thin-shell approximation

The thin-shell approximation codes usually split the infinitesimally shell into small parts and solve the dynamical equations for each part separately. Each part of the shell accretes new mass and experiences forces given by internal and external pressure and the gravitational field. So, in fact, it is a kind of the N-body code. Simulations of this kind in 2D, which are also called 1+1/2 dimensional, have been developed by Tenorio-Tagle & Palouš (1987) and Palouš et al. (1990). They include the z-stratification of the ambient medium, the galactic differential rotation and the radiative cooling of the shell interior.

The thin-shell approximation codes in 3D (2+1/2 dimensional) have been performed by Palouš (1990, 1992), Silich et al. (1996) and Ehlerová (2000). They include also the effect of the evaporation of small interstellar clouds, which are engulfed by the expanding shell. These clouds evaporate in the hot shell interior increasing its density. This leads to the higher energy loss by the radiative cooling, which increases the X-ray luminosity of the bubble and affects the shell dynamics.

The advantage of the thin-shell approximation codes is that they are substantially faster than the (magneto)hydrodynamic simulations. It makes these codes ideal as the reference models when searching for the physical parameters of a real object.

2.5.2 HD and MHD simulations

Chevalier (1974) studied an evolution of supernovae remnants using a spherically symmetric 1D hydrodynamic code. His model includes the magnetic field (in the form of the magnetic pressure) and the radiative cooling. He obtained the famous formula

$$\left(\frac{E_0}{\text{erg}}\right) = 5.3 \times 10^{43} \left(\frac{n_0}{\text{cm}^{-3}}\right)^{1.12} \left(\frac{v_{\text{sh}}}{\text{km s}^{-1}}\right)^{1.40} \left(\frac{r_{\text{sh}}}{\text{pc}}\right)^{3.12}, \quad (2.44)$$

which connects the energy E_0 necessary for creating the shell to its radius r_{sh} , expansion velocity v_{sh} and particle density of the ambient medium n_0 . This formula is often used by observers to determine the energy of an object.

The formation of the thin shell in supernovae remnants was simulated by Falle (1975). He used the 1D Lagrangian hydrocode which includes the magnetic field as the magnetic pressure. Falle (1981) shows that the transition from the Sedov (adiabatic) phase is accompanied by a very quick collapse into the thin shell due to the thermal instability. The collapse is so quick, that multiple additional shocks may be created.

Różycka (1985) has developed a 2D second-order accurate hydrodynamic code and used it to study the evolution of the stellar wind bubbles. He investigated the thermal and hydrodynamic instabilities of the thin shell.

The evolution of a super-bubble expanding in the inhomogeneous medium was studied by Tomisaka & Ikeuchi (1986). They use the 2D hydrocode to model the super-bubble driven by sequential SN explosions in the z-stratified medium. Their results corresponds to the HI worms observed by Heiles (1984).

The super-bubble blow-outs (the opening of the shell due to acceleration of the outer shock-wave down the density gradient of the ISM) were investigated by Mac Low & McCray (1988) and Mac Low et. al (1989). They used the thin-shell approximation and the ZEUS2D hydrocode and compared both approaches with each other and with the models of the other authors. They found that the thin-shell approximation worked very well.

Mac Low & Norman (1993) used the ZEUS2D hydrocode to study the non-linear regime of hydrodynamic instabilities discovered by Vishniac (1983). They showed that the instability saturates due to weak transverse shocks and it does not break the shell in the fragments. Nevertheless, it may create density enhancements which may be subject of the gravitational instability.

Chevalier & Blondin (1995) have studied the non-linear hydrodynamic instabilities in the SNR using the code VH-1.

In this work we develop the 3D hydrodynamic model of the expanding shell based on the ZEUS3D code. We use it to study the gravitational instability evolving in these shells. The gravitational potential is computed by the multigrid Poisson solver Šemík.

Chapter 3

The gravitational instability

In this chapter we give the theory of the gravitational instability of expanding shells. In the first section we formulate the fluid equations and the Poisson equation on the shell surface. These equations are linearised and analytically solved in Section 3.2. The third Section 3.3 deals with the solution of the equations with the quadratic terms. In the last Section 3.4 we describe the procedure of obtaining the mass spectrum of fragments from the linear analysis. This mass spectrum is compared to the spectra obtained with similar procedure in different physical situations and to the observed mass spectrum of Giant Molecular Clouds (GMC) in the Milky Way and to the Initial Mass Function of stars (IMF).

The basic equation are formulated in 2D coordinates in the shell surface. (\mathbf{u}, \mathbf{v}) denotes the scalar product of the 2D vectors \mathbf{u} and \mathbf{v} , the differential operator ∇ acts in the 2D surface, too.

3.1 Fluid equations on the shell surface

We consider the cold and thin shell of radius r_{sh} surrounding the hot medium interior of it. It is expanding with velocity v_{sh} into a uniform medium of density ρ_0 . The intrinsic surface density of the shell Σ is composed of unperturbed part Σ_0 plus the perturbation Σ_1 ($\Sigma = \Sigma_0 + \Sigma_1$). Perturbation Σ_1 results from the flows on the surface of the shell redistributing the accumulated mass. We assume that Σ_0 corresponds to r_{sh} as $\Sigma_0 = \rho_0 r_{\text{sh}}/3$, which means that all the encountered mass is accumulated to the shell. (It comes from $\Sigma_0 = \frac{4}{3}\pi r_{\text{sh}}^3 \rho_0 / (4\pi r_{\text{sh}}^2)$).

The mass conservation law in a small area on the surface of the shell is

$$\frac{\partial m}{\partial t} + (\nabla, m\mathbf{v}) = Av_{\text{sh}}\rho_0 , \quad (3.1)$$

where m is the mass in area $A = 4\pi\alpha r_{\text{sh}}^2$, α is a fixed small fraction of the sphere. The term on the RHS describes the (uniform) accumulation of mass due to the supersonic expansion. \mathbf{v} denotes a two-dimensional velocity of surface flows connected to perturbations above the stretching of the area due to expansion of the unperturbed shell. In the following procedure we consider angular velocity $\mathbf{\Omega} = \mathbf{v}/r_{\text{sh}}$ to describe the evolution on the surface of the shell. With $\Sigma = m/A$ we obtain continuity equation in a form

$$\frac{\partial \Sigma}{\partial t} + 2\Sigma \frac{v_{\text{sh}}}{r_{\text{sh}}} + \Sigma r_{\text{sh}} (\nabla, \mathbf{\Omega}) + r_{\text{sh}} (\mathbf{\Omega}, \nabla) \Sigma = v_{\text{sh}} \rho_0 . \quad (3.2)$$

The equation of motion for flows on the shell surface has a form

$$\frac{1}{A} \frac{d(m\mathbf{v})}{dt} = -c_{\text{sh}}^2 \nabla \Sigma - \Sigma \nabla \Phi , \quad (3.3)$$

where c_{sh} is the constant isothermal sound-speed inside the cold shell, which is a free parameter in this analysis. Φ is the gravitational potential generated by the mass distribution given in the surface the shell. Using the continuity equation 3.2, we can rewrite Eq. 3.3 as

$$r_{\text{sh}} \frac{\partial \mathbf{\Omega}}{\partial t} + v_{\text{sh}} \mathbf{\Omega} + 3v_{\text{sh}} \mathbf{\Omega} \frac{\Sigma_0}{\Sigma} + r_{\text{sh}}^2 (\mathbf{\Omega}, \nabla) \mathbf{\Omega} = -\frac{c_{\text{sh}}^2}{\Sigma} \nabla \Sigma - \nabla \Phi . \quad (3.4)$$

The gravitational potential Φ is related to the surface density by the Poisson equation

$$\nabla^2 \Phi = 4\pi G \Sigma \delta(r - r_{\text{sh}}) , \quad (3.5)$$

where G is the constant of gravity and δ denotes the delta function.

We assume a small perturbation of the shell surface density $\Sigma_1 \ll \Sigma_0$ which evolves due to surface flows given with angular velocity $\mathbf{\Omega}$. The perturbed hydrodynamic equations 3.2, 3.4 and the perturbed Poisson equation 3.5 have form

$$\frac{\partial \Sigma_1}{\partial t} + 2\Sigma_1 \frac{v_{\text{sh}}}{r_{\text{sh}}} + \Sigma r_{\text{sh}} (\nabla, \mathbf{\Omega}) + r_{\text{sh}} (\mathbf{\Omega}, \nabla) \Sigma_1 = 0 , \quad (3.6)$$

$$\begin{aligned} & r_{\text{sh}} \frac{\partial \mathbf{\Omega}}{\partial t} + r_{\text{sh}}^2 (\mathbf{\Omega}, \nabla) \mathbf{\Omega} + 4v_{\text{sh}} \mathbf{\Omega} - 3v_{\text{sh}} \mathbf{\Omega} \frac{\Sigma_1}{\Sigma_0} \\ & = -\frac{c_{\text{sh}}^2}{\Sigma_0} \left(1 - \frac{\Sigma_1}{\Sigma_0}\right) \nabla \Sigma_1 - \nabla \Phi_1 , \end{aligned} \quad (3.7)$$

$$\Delta \Phi_1 = 4\pi G \Sigma_1 \delta(r - r_{\text{sh}}) , \quad (3.8)$$

where the $1/\Sigma$ in Eq. 3.4 was evaluated up to quadratic terms in Σ_1 : $\frac{c_{\text{sh}}^2}{\Sigma} \nabla \Sigma = \frac{c_{\text{sh}}^2}{\Sigma_0} (1 - \frac{\Sigma_1}{\Sigma_0} + \text{higher order terms}) \nabla \Sigma_1$, and $\nabla \Sigma_0 = 0$ on the shell surface.

The perturbation of the surface density Σ_1 and the angular velocity of the surface flows $\mathbf{\Omega}$ can be decomposed into the Fourier series as

$$\begin{aligned} \Sigma_1 &= \Sigma_{10} + \sum_{\eta} \Sigma_{\eta} e^{i(\eta, \Theta)} \\ \mathbf{\Omega} &= \mathbf{\Omega}_0 + \sum_{\eta} \mathbf{\Omega}_{\eta} e^{i(\eta, \Theta)} \end{aligned} \quad (3.9)$$

where Θ is a positional vector of the 2D angular coordinates in the shell surface and η denotes a dimensionless wave-vector $\eta = \mathbf{k} r_{\text{sh}}$ (\mathbf{k} is the standard 2D wave-vector in the shell surface). We assume no surface macroscopic flow through all the considered area which means $\mathbf{\Omega}_0 = 0$. Further we assume $\Sigma_{10} = 0$ (all the mass accumulation due to expansion to the ambient medium is included in Σ_0).

Eqs. 3.9 may be inserted to the perturbed Eqs. 3.6 and 3.7. The Fourier transform of the continuity equation 3.6 is

$$\begin{aligned} \dot{\Sigma}_{\eta} + \Sigma_0 (-i\eta, \mathbf{\Omega}_{-\eta}) + 2 \frac{v_{\text{sh}}}{r_{\text{sh}}} \Sigma_{\eta} + \sum_{\eta'} (-i\eta', \mathbf{\Omega}_{-\eta'}) \Sigma_{\eta-\eta'} \\ + \sum_{\eta'} (\mathbf{\Omega}_{\eta-\eta'}, -i\eta') \Sigma_{\eta'} = 0, \end{aligned} \quad (3.10)$$

where we used the identity $\eta' + (\eta - \eta') = \eta$.

The solution of the Poisson equation 3.5 for the case of the thin layer is

$$\nabla \Phi_1 = -2\pi G \sum_{\eta} \Sigma_{\eta} \frac{i\eta}{|\eta|} e^{i(\eta, \Theta)} \quad (3.11)$$

(see e.g. Binney & Tremaine, 1987). Using this and Eqs. 3.9 we get the Fourier transform of the equation of motion 3.7 in a form

$$\begin{aligned} r_{\text{sh}} \dot{\mathbf{\Omega}}_{\eta} + 4v_{\text{sh}} \mathbf{\Omega}_{\eta} - \frac{3v_{\text{sh}}}{\Sigma_0} \sum_{\eta'} \mathbf{\Omega}_{\eta'} \Sigma_{\eta-\eta'} + r_{\text{sh}} \sum_{\eta'} (\mathbf{\Omega}_{\eta-\eta'}, -i\eta') \mathbf{\Omega}_{\eta'} \\ (-i\eta', \mathbf{\Omega}_{-\eta'}) = -\frac{c_{\text{sh}}^2}{r_{\text{sh}} \Sigma_0} i\eta \Sigma_{\eta} + \frac{c_{\text{sh}}^2}{r_{\text{sh}} \Sigma_0^2} \sum_{\eta'} i\eta' \Sigma_{\eta-\eta'} \Sigma_{\eta'} + 2\pi G \frac{i\eta}{|\eta|} \Sigma_{\eta} \end{aligned} \quad (3.12)$$

3.2 Linear analysis

The Eqs. 3.10 and 3.12 can be solved analytically using the linear terms only. The complete linear analysis of the gravitational instability of the expanding shell was also done by Elmegreen (1994). The linearised equations have a form

$$\dot{\Sigma}_{\eta} + \Sigma_0 (-i\eta, \mathbf{\Omega}_{-\eta}) + 2 \frac{v_{\text{sh}}}{r_{\text{sh}}} \Sigma_{\eta} = 0 \quad (3.13)$$

$$r_{\text{sh}} \dot{\mathbf{\Omega}}_{\eta} = -\frac{c_{\text{sh}}^2}{\Sigma_0 r_{\text{sh}}} i\eta \Sigma_{\eta} + 2\pi G \frac{i\eta}{|\eta|} \Sigma_{\eta} - 4v_{\text{sh}} \mathbf{\Omega}_{\eta} \quad (3.14)$$

Angular velocity $\mathbf{\Omega}_{\eta}$ can be split in two components parallel and orthogonal to the wave-vector η

$$\mathbf{\Omega}_{\eta} = \Omega_{\eta_{\parallel}} \frac{\eta}{|\eta|} + \Omega_{\eta_{\perp}} \frac{\eta_{\perp}}{|\eta_{\perp}|}, \quad (3.15)$$

where η_{\perp} is a vector in the tangential plane, which is perpendicular to the wave-vector η and $|\eta_{\perp}| = |\eta|$.

We get the set of equations

$$\dot{\Sigma}_{\eta} = -2\frac{v_{\text{sh}}}{r_{\text{sh}}} \Sigma_{\eta} - i\eta \Sigma_0 \Omega_{\eta_{\parallel}} \quad (3.16)$$

$$\dot{\Omega}_{\eta_{\parallel}} = \left(i\frac{2\pi G}{r_{\text{sh}}} - i\frac{c_{\text{sh}}^2 \eta}{\Sigma_0 r_{\text{sh}}^2} \right) \Sigma_{\eta} - 4\frac{v_{\text{sh}}}{r_{\text{sh}}} \Omega_{\eta_{\parallel}} \quad (3.17)$$

$$\dot{\Omega}_{\eta_{\perp}} = -4\frac{v_{\text{sh}}}{r_{\text{sh}}} \Omega_{\eta_{\perp}}, \quad (3.18)$$

which can be formally written using the linear operator \mathcal{L} as

$$\begin{pmatrix} \dot{\Sigma}_{\eta} \\ \dot{\Omega}_{\eta_{\parallel}} \\ \dot{\Omega}_{\eta_{\perp}} \end{pmatrix} = \mathcal{L} \begin{pmatrix} \Sigma_{\eta} \\ \Omega_{\eta_{\parallel}} \\ \Omega_{\eta_{\perp}} \end{pmatrix}. \quad (3.19)$$

The solution of the set of Eqs. 3.19 is

$$\begin{pmatrix} \dot{\Sigma}_{\eta} \\ \dot{\Omega}_{\eta_{\parallel}} \\ \dot{\Omega}_{\eta_{\perp}} \end{pmatrix} = \begin{pmatrix} \Sigma_{\eta,0} \\ \Omega_{\eta_{\parallel},0} \\ \Omega_{\eta_{\perp},0} \end{pmatrix} \exp(\omega_{\eta} t), \quad (3.20)$$

where ω_{η} are eigenvalues of the operator \mathcal{L} and $\Sigma_{\eta,0}$, $\Omega_{\eta_{\parallel},0}$ and $\Omega_{\eta_{\perp},0}$ are initial values of the appropriate quantities.

Eq. 3.18 for the transversal modes decouples from the first two ones and its solution is the exponential decrease given by the eigenvalue

$$\omega_{\eta}^{(3)} = -4\frac{v_{\text{sh}}}{r_{\text{sh}}}. \quad (3.21)$$

The eigenvalues of the Eqs. 3.16 and 3.17 are

$$\omega_{\eta}^{(1,2)} = -\frac{3v_{\text{sh}}}{r_{\text{sh}}} \pm \sqrt{\frac{v_{\text{sh}}^2}{r_{\text{sh}}^2} - \frac{\eta^2 c_{\text{sh}}^2}{r_{\text{sh}}^2} + \frac{2\pi G \Sigma_0 \eta}{r_{\text{sh}}}}, \quad (3.22)$$

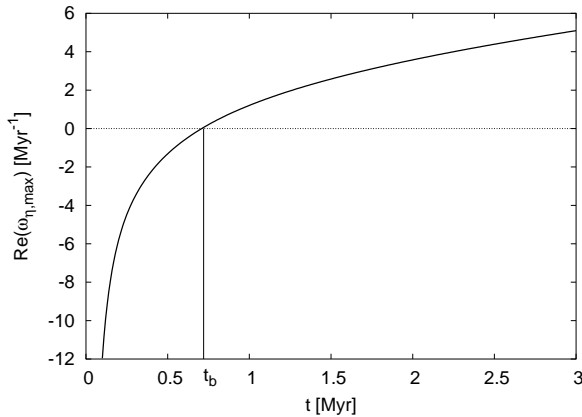


Figure 3.1: The time evolution of the maximum perturbation growth rate $\omega_{\eta,\max}$. The dynamical quantities r_{sh} , v_{sh} and Σ_0 of the shell were obtained from the thin shell approximation with parameters $L = 5^{51}$ erg/Myr, $n_0 = 1\text{cm}^{-3}$ and $\mu = 1.3$ amu. The sound-speed in the shell c_{sh} was 1 km/s.

where η is the magnitude of η . They are time-dependent dispersion relations of the modes on the shell surface. The real part of $\omega_{\eta}^{(2)}$ is always negative, so it cannot describe the instability (growth of perturbations). Eigenvalue $\omega_{\eta}^{(1)}$ (hereafter ω_{η}), on the other hand, is more physically interesting.

Perturbations grow if ω_{η} is real and positive. The last term with G represents the influence of gravity, the term with c_{sh}^2 gives the influence of pressure and the remaining two terms come from a stretching due to expansion. In the short-wavelength modes the pressure always dominates making the short-wavelength perturbations stable. Long-wavelength modes are stabilised by the stretching, in particular during the initial period of expansion, when r_{sh} is small and v_{sh} is large. Later, when the shell decelerates and accumulates enough mass, the gravity term dominates intermediate modes between short-wavelength modes stabilised by pressure and long-wavelength modes stabilised by stretching.

The maximum perturbation growth occurs at wavenumber

$$\eta_{\max} = \frac{\pi G \Sigma_0 r_{\text{sh}}}{c_{\text{sh}}^2} \quad (3.23)$$

and its rate is

$$\omega_{\eta,\max} = -\frac{3v_{\text{sh}}}{r_{\text{sh}}} + \sqrt{\frac{v_{\text{sh}}^2}{r_{\text{sh}}^2} + \frac{\pi^2 G^2 \Sigma_0^2}{c_{\text{sh}}^2}}. \quad (3.24)$$

Fig. 3.1 shows the typical evolution of the maximum perturbation growth

rate $\omega_{\eta, \max}$. The beginning of the gravitational instability t_b can be determined as the time when $\omega_{\eta, \max} = 0$, i.e. the first mode becomes unstable. Using the thin shell approximation with analytical solution 2.30 and 2.32 to obtain the shell parameters r_{sh} , v_{sh} and Σ_0 we get

$$t_b = \left(\frac{288}{25\pi^2 G^2} \right)^{5/14} \left(\frac{4\pi}{15} \right)^{1/7} c_{\text{sh}}^{5/7} E_0^{-1/7} \rho_0^{-4/7}, \quad (3.25)$$

for the shell created by the abrupt energy input and

$$t_b = \left(\frac{648}{25\pi^2 G^2} \right)^{5/16} \left(\frac{4\pi}{5} \right)^{1/8} c_{\text{sh}}^{5/8} E_0^{-1/8} \rho_0^{-1/2} \quad (3.26)$$

for the continuous energy input case. Converting Eqs. 3.25 and 3.26 to the astrophysical units we get

$$t_b = 28.0 \left(\frac{c_{\text{sh}}}{\text{km s}^{-1}} \right)^{5/7} \left(\frac{E_0}{10^{51} \text{ erg}} \right)^{-1/7} \left(\frac{\mu}{1.3 \text{ amu}} \frac{n_0}{\text{cm}^{-3}} \right)^{-4/7} \text{ Myr} \quad (3.27)$$

and

$$t_b = 28.8 \left(\frac{c_{\text{sh}}}{\text{km s}^{-1}} \right)^{5/8} \left(\frac{L}{10^{51} \text{ erg Myr}^{-1}} \right)^{-1/8} \left(\frac{\mu}{1.3 \text{ amu}} \frac{n_0}{\text{cm}^{-3}} \right)^{-1/2} \text{ Myr}. \quad (3.28)$$

Whitworth & Francis (2002) have shown that the radial gravitational force, which decelerates the shell expansion, can prevent the shell from accumulating enough mass and becoming gravitationally unstable. The very simple criterion can be obtained by the comparison of the gravitational instability time t_b to the time t_0 , when the radial gravity starts to dominate (see Eq. 2.40). If $t_b > t_0$ the expansion of the shell almost stalls before the gravitational instability occurs and cannot accrete additional mass to become unstable. Values of t_b and t_0 for the various physical parameters are given by Tab. 3.2. We can see that the condition $t_b < t_0$ is fulfilled for models with $c_{\text{sh}} = 1$ and 2 km/s. Using this condition for t_b given by Eq. 3.26 we get the threshold for the energy input rate

$$L > \frac{4\pi}{5} \left(\frac{32G}{3\pi} \right)^4 \left(\frac{648}{25\pi^2 G^2} \right)^{5/2} c_{\text{sh}}^5 \approx 2640 G^{-1} c_{\text{sh}}^5. \quad (3.29)$$

This value should be considered as the lower guess, i.e. the fragmentation cannot occur if L is smaller. The more detailed analysis (see Whitworth & Francis, 2002) yields the value of 1 magnitude higher

n_0	t_0	t_b ($L=1, c=1$)	t_b ($L=5, c=1$)	t_b ($L=1, c=2$)	t_b ($L=1, c=3$)
10^{-1}	163	91.1	74.5	140	181
10^0	51.7	28.8	23.6	44.4	57.2
10^1	16.3	9.11	7.45	14.0	18.1
10^2	5.17	2.88	2.36	4.44	5.72
10^3	1.63	0.911	0.745	1.40	1.81
10^4	0.517	0.288	0.236	0.444	0.572
10^5	0.163	9.11×10^{-2}	7.45×10^{-2}	0.14	0.181
10^6	5.17×10^{-2}	2.88×10^{-2}	2.36×10^{-2}	4.44×10^{-2}	5.72×10^{-2}

Table 3.1: t_0 and t_B for various combinations of parameters n_0 , L and c_{sh} . t_0 and t_b are in Myr, n_0 in cm^{-3} , L in 10^{51} erg/Myr and c_{sh} in km/s.

$$L > 3 \times 10^4 G^{-1} c_{\text{sh}}^5. \quad (3.30)$$

For the shells with sound-speeds 1, 2 and 3 km/s are the threshold values of energy input rate 0.14, 4.5 and 34×10^{51} erg/Myr, respectively. The high exponent at c_{sh} makes the sound-speed in the shell the crucial parameter: if it is high ($> 2 - 3$ km/s for HI shells and super-shells), it would be difficult to find the physically relevant energy source, which can bring the shell to the gravitationally unstable state.

If the shell is unstable for a certain time, the fragments may form. The quantity, which represents the state of the fragmentation at a certain wavelength, is the fragmentation integral, defined by Ehlerová et al. (1997)

$$I_f(t, \eta) \equiv \int_{t_b}^t \omega_\eta(t') dt'. \quad (3.31)$$

The authors consider that the fragments are well developed when $I_f = 1$. Consequently, the fragmentation time t_f may be defined as the time when

$$I_f(t_f, \eta) = 1 \quad (3.32)$$

for the first η .

3.3 Solution with quadratic terms

The set of non-linear hydrodynamic equations on surface of the shell can be solved using the similar procedure as adopted by Fuchs (1996) for the case of uniformly rotating self-gravitating disks. In this section we suggest the idea

of the procedure, the complete non-linear analysis can be found in Wunsch & Palouš (2001).

Nonlinear Eqs. 3.10 and 3.12 can be formally written as

$$\begin{pmatrix} \dot{\Sigma}_\eta \\ \dot{\Omega}_{\eta\parallel} \\ \dot{\Omega}_{\eta\perp} \end{pmatrix} = \mathcal{L} \begin{pmatrix} \Sigma_\eta \\ \Omega_{\eta\parallel} \\ \Omega_{\eta\perp} \end{pmatrix} + \mathcal{N}, \quad (3.33)$$

where \mathcal{N} represents the non-linear terms. We search for a solution of Eqs. 3.33 as a combination of the eigenvectors of the linear operator \mathcal{L}

$$\begin{pmatrix} \Sigma_\eta \\ \Omega_{\eta\parallel} \\ \Omega_{\eta\perp} \end{pmatrix} = \xi_\eta(t) \begin{pmatrix} \Sigma_\eta \\ \Omega_{\eta\parallel} \\ \Omega_{\eta\perp} \end{pmatrix}^{(1)} + \\ + \psi_\eta(t) \begin{pmatrix} \Sigma_\eta \\ \Omega_{\eta\parallel} \\ \Omega_{\eta\perp} \end{pmatrix}^{(2)} + \phi_\eta(t) \begin{pmatrix} \Sigma_\eta \\ \Omega_{\eta\parallel} \\ \Omega_{\eta\perp} \end{pmatrix}^{(3)}, \quad (3.34)$$

where $\xi_\eta(t)$, $\psi_\eta(t)$ and $\phi_\eta(t)$ are time dependent amplitudes of eigenvectors

$$\begin{pmatrix} \Sigma_\eta \\ \Omega_{\eta\parallel} \\ \Omega_{\eta\perp} \end{pmatrix}^{(1,2)} = \begin{pmatrix} i\eta\Sigma_0 \\ -2\frac{v_{\text{sh}}}{r_{\text{sh}}} - \omega_\eta^{(1,2)} \\ 0 \end{pmatrix} \quad (3.35)$$

$$\begin{pmatrix} \Sigma_\eta \\ \Omega_{\eta\parallel} \\ \Omega_{\eta\perp} \end{pmatrix}^{(3)} = \begin{pmatrix} 0 \\ 0 \\ 1 \end{pmatrix}. \quad (3.36)$$

There are always four solutions differing in eigenvectors multiplied by $\pm i$ or ± 1 . We select only solutions with physical relevance given by eigenvectors 3.35. We find orthonormal vectors $(\Sigma_\eta, \Omega_{\eta\parallel}, \Omega_{\eta\perp})^{(1,2,3)}$ in order that

$$\begin{aligned} (\Sigma_\eta, \Omega_{\eta\parallel}, \Omega_{\eta\perp})^{(j)} \begin{pmatrix} \Sigma_\eta \\ \Omega_{\eta\parallel} \\ \Omega_{\eta\perp} \end{pmatrix}^{(j)} &= 1 \\ (\Sigma_\eta, \Omega_{\eta\parallel}, \Omega_{\eta\perp})^{(j)} \begin{pmatrix} \Sigma_\eta \\ \Omega_{\eta\parallel} \\ \Omega_{\eta\perp} \end{pmatrix}^{(k \neq j)} &= 0, \end{aligned} \quad (3.37)$$

where $j, k = 1, 2, 3$. The orthonormal vectors are

$$\begin{aligned}
(\Sigma_\eta, \Omega_{\eta_\parallel}, \Omega_{\eta_\perp})^{(1)} &= \left(\frac{\omega^{(2)} + 2\frac{V}{R}}{i\eta\Sigma_0(\omega^{(2)} - \omega^{(1)})}, \frac{1}{(\omega^{(2)} - \omega^{(1)})}, 0 \right) \\
(\Sigma_\eta, \Omega_{\eta_\parallel}, \Omega_{\eta_\perp})^{(2)} &= \left(\frac{\omega^{(1)} + 2\frac{V}{R}}{i\eta\Sigma_0(\omega^{(1)} - \omega^{(2)})}, \frac{1}{(\omega^{(1)} - \omega^{(2)})}, 0 \right) \\
(\Sigma_\eta, \Omega_{\eta_\parallel}, \Omega_{\eta_\perp})^{(3)} &= (0, 0, 1)
\end{aligned} \tag{3.38}$$

We insert Eq. 3.34 into Eq. 3.33, multiply it by the orthonormal vectors (Eq. 3.38) and obtain a set of equations for amplitudes $\xi_{\eta(t)}$, $\psi_{\eta(t)}$ and $\phi_{\eta(t)}$

$$\begin{aligned}
\dot{\xi}_\eta &= \omega^{(1)}\xi_\eta - \left(\frac{\partial}{\partial t} \begin{pmatrix} \Sigma_\eta \\ \Omega_{\eta_\parallel} \\ \Omega_{\eta_\perp} \end{pmatrix}^{(1)}, (\Sigma_\eta, \Omega_{\eta_\parallel}, \Omega_{\eta_\perp})^{(1)} \right) \xi_\eta \\
&\quad - \left(\frac{\partial}{\partial t} \begin{pmatrix} \Sigma_\eta \\ \Omega_{\eta_\parallel} \\ \Omega_{\eta_\perp} \end{pmatrix}^{(2)}, (\Sigma_\eta, \Omega_{\eta_\parallel}, \Omega_{\eta_\perp})^{(1)} \right) \psi_\eta \\
&\quad + \left(\mathcal{N}, (\Sigma_\eta, \Omega_{\eta_\parallel}, \Omega_{\eta_\perp})^{(1)} \right)
\end{aligned} \tag{3.39}$$

$$\begin{aligned}
\dot{\psi}_\eta &= \omega^{(2)}\psi_\eta - \left(\frac{\partial}{\partial t} \begin{pmatrix} \Sigma_\eta \\ \Omega_{\eta_\parallel} \\ \Omega_{\eta_\perp} \end{pmatrix}^{(2)}, (\Sigma_\eta, \Omega_{\eta_\parallel}, \Omega_{\eta_\perp})^{(2)} \right) \psi_\eta \\
&\quad - \left(\frac{\partial}{\partial t} \begin{pmatrix} \Sigma_\eta \\ \Omega_{\eta_\parallel} \\ \Omega_{\eta_\perp} \end{pmatrix}^{(1)}, (\Sigma_\eta, \Omega_{\eta_\parallel}, \Omega_{\eta_\perp})^{(2)} \right) \xi_\eta \\
&\quad + \left(\mathcal{N}, (\Sigma_\eta, \Omega_{\eta_\parallel}, \Omega_{\eta_\perp})^{(2)} \right)
\end{aligned} \tag{3.40}$$

$$\begin{aligned}
\dot{\phi}_\eta &= \omega^{(3)}\phi_\eta - \left(\frac{\partial}{\partial t} \begin{pmatrix} \Sigma_\eta \\ \Omega_{\eta_\parallel} \\ \Omega_{\eta_\perp} \end{pmatrix}^{(3)}, (\Sigma_\eta, \Omega_{\eta_\parallel}, \Omega_{\eta_\perp})^{(3)} \right) \phi_\eta \\
&\quad + \left(\mathcal{N}, (\Sigma_\eta, \Omega_{\eta_\parallel}, \Omega_{\eta_\perp})^{(3)} \right),
\end{aligned} \tag{3.41}$$

where we denote $\omega^{(j)} \equiv \omega_{\eta, \max}^{(j)}$.

The Eq. 3.41 is decoupled from the others and its solution is the decrease of the initial value of ϕ . Eqs. 3.39 and 3.40 are coupled through the linear and non-linear terms. The interaction through the linear terms is weak, since the coupled linear terms have smaller amplitudes compared to linear terms and they decrease with time due to their dependence on the time derivatives of the eigenvectors, which are very small in the later stages of the shell evolution. The coupling through the non-linear terms leads to the terms of the third and higher orders, which can be neglected with respect to quadratic terms. Furthermore, the solution of the Eq. 3.40 has a decreasing character, because the first term on the right side, which includes the “stable” $\omega^{(2)}$, dominates. The Eq. 3.39 is the most interesting one, because it has $\omega^{(1)}$ in the first linear term, and only the $\omega^{(1)}$ can be real and positive, which leads to the instability.

In analogy to Fuchs (1996) we group together components with real ω_η into wave-packet and take the wavenumber η_{\max} . Other components are grouped to the wave-packets of the same width and approximated by the average wave-numbers. The $\xi_{\eta_{\max}}$ modes grow, the $\psi_{\eta_{\max}}$ and the $\phi_{\eta_{\max}}$ modes descend. Other modes oscillate with decrease.

Demanding $\eta = \eta' = |\eta - \eta'| = \eta_{\max}$ we obtain from geometrical consideration:

$$(\eta - \eta'_\pm, \eta'_\pm) = -\frac{1}{2}\eta_{\max}^2 \quad (\eta'_\pm, \eta) = \frac{1}{2}\eta_{\max}^2 \quad , \quad (3.42)$$

where η'_+ and η'_- are two wave-vectors inclined at angles 60° to the wave-vector η . It means that ξ_η wave-packets non-linearly interact with others with wave-vectors η'_\pm . Using Eqs. 3.22 and 3.42, the Eq. 3.39 can be simplified to the set of equations

$$\begin{aligned} \dot{\xi} &= (i\omega^{(2)} + A)\xi \quad + \quad B\xi_+\xi_- \\ \dot{\xi}_+ &= (i\omega^{(2)} + A)\xi_+ \quad + \quad B\xi\xi_-^* \\ \dot{\xi}_- &= (i\omega^{(2)} + A)\xi_- \quad + \quad B\xi\xi_+^* \end{aligned}$$

where $\xi \equiv \xi_\eta$, $\xi_+ \equiv \xi_{\eta_+}$, $\xi_- \equiv \xi_{\eta_-}$, the asterisk denotes the complex conjugation and

$$\begin{aligned} A &= -\frac{18r_{\text{sh}}v_{\text{sh}}c_{\text{sh}}^2\dot{\Sigma}_0\gamma + 18v_{\text{sh}}^2c_{\text{sh}}^2\dot{\Sigma}_0 + 2r_{\text{sh}}^4\pi^2G^2\rho_0^2\dot{\Sigma}_0}{2\Sigma_0(9v_{\text{sh}}^2c_{\text{sh}}^2 + \pi^2G^2\rho_0^2r_{\text{sh}}^4)} - \\ &\quad -\frac{18v_{\text{sh}}^2c_{\text{sh}}^2\Sigma_0\gamma + 2\pi^2G^2\rho_0^2r_{\text{sh}}^3v_{\text{sh}}\Sigma_0}{2\Sigma_0(9v_{\text{sh}}^2c_{\text{sh}}^2 + \pi^2G^2\rho_0^2r_{\text{sh}}^4)} - \\ &\quad -\frac{-9r_{\text{sh}}\dot{v}_{\text{sh}}c_{\text{sh}}^2\Sigma_0\gamma + 9v_{\text{sh}}\dot{v}_{\text{sh}}c_{\text{sh}}^2\Sigma_0}{2\Sigma_0(9v_{\text{sh}}^2c_{\text{sh}}^2 + \pi^2G^2\rho_0^2r_{\text{sh}}^4)} \end{aligned} \quad (3.43)$$

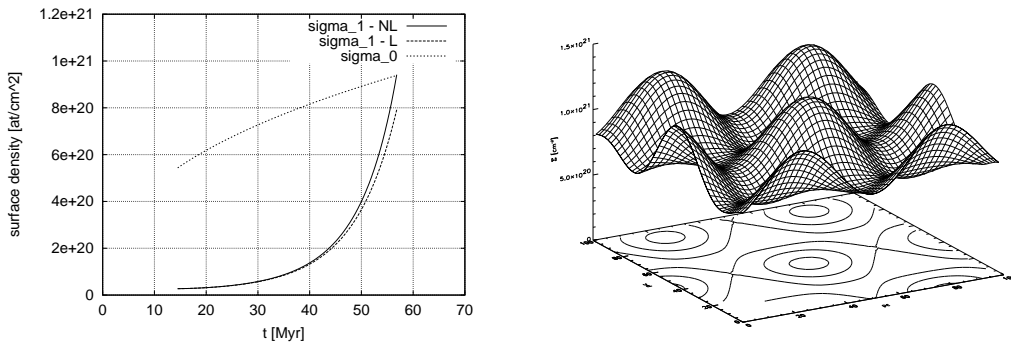


Figure 3.2: Left: The evolution of the amplitude of the surface density perturbation in the linear and non-linear case. Right: The spatial distribution of the surface density of the three interacting modes inclined at an angle 60° .

and

$$B = \frac{-3\pi^3 G^3 \Sigma_0^3 r_{\text{sh}} + 8\pi G \Sigma_0 c_{\text{sh}}^2 v_{\text{sh}} \left(\frac{v_{\text{sh}}}{r_{\text{sh}}} - \gamma \right)}{4c_{\text{sh}}^4 \gamma}, \quad (3.44)$$

where

$$\gamma = \sqrt{\frac{v_{\text{sh}}^2}{r_{\text{sh}}^2} + \frac{\pi^2 G^2 \Sigma_0^2}{c_{\text{sh}}^2}}. \quad (3.45)$$

The set of Eqs. 3.43 describes the time evolution of one triplet of the most interacting modes (η, η_+, η_-) . We solve this set of equations numerically, setting the initial values of ξ , ξ_+ and ξ_- randomly so, that $\Sigma_1/\Sigma_0 = 0.05$ at t_b . Fig. 3.2, left panel, shows the time evolution of the amplitude of the surface density perturbation in one of such solutions. It is compared to the solution given by the linearised equations and we can see that the difference is small. Other experiments show that the quadratic terms (included with the approximation described above) cannot substantially influence the perturbation growth rate (see Wünsch & Palouš, 2001).

The surface density which corresponds to the triplet of interacting modes is suggested by Fig. 3.2, right panel. We can see the sixty-degree symmetry, expected to appear in more complicated models (or in reality) if the non-linear analysis works well and the mode interaction is strong enough.

3.4 The mass spectrum of fragments

The linear analysis of the gravitational instability of the expanding shell yields the dispersion relation $\omega_\eta(t)$ (Eq. 3.22), which represents the growth

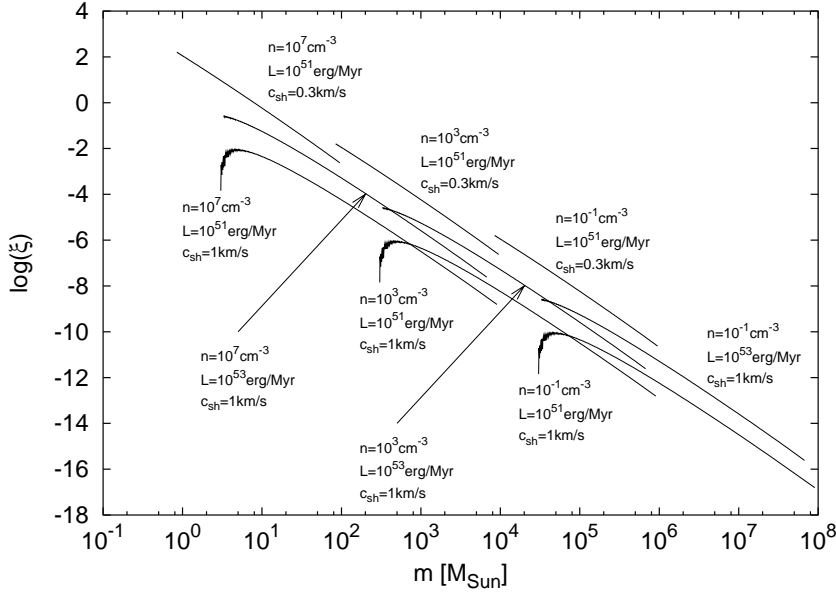


Figure 3.3: The mass spectra $\xi(m) = dN/dm$ for various parameters of the shell.

rate of perturbations at mode η . The fragmentation integral $I_f(\eta, t)$ (Eq. 3.31), which is the integral of $\omega_\eta(t)$ over the time, determines the state of fragmentation at a certain mode, i.e. the development of fragments of a certain size. It can be used to determine the relative number of fragments in the shell, i.e. the mass spectrum of fragments.

We assume that the number of fragments of the wavelength $\lambda = 2\pi r_{\text{sh}}/\eta$ is proportional to the fragmentation integral $I_f(\eta, t)$. The surface of the spherical shell of radius r_{sh} is able to accommodate $r_{\text{sh}}^2/\lambda^2$ fragments of wavelength λ . Therefore, the number of fragments is given by the relation

$$N \sim \frac{r_{\text{sh}}^2}{\lambda^2} I_f(\eta) = \frac{\eta^2}{4\pi^2} I_f(\eta) \quad (3.46)$$

and the number of fragments with wave-numbers from the interval $(\eta, \eta + d\eta)$ is

$$dN \sim \frac{\eta}{4\pi^2} \left(2dI_f(\eta) + \eta \frac{dI_f(\eta)}{d\eta} \right) d\eta. \quad (3.47)$$

The mass m of fragment of the wavelength λ is

$$m = \pi \left(\frac{\lambda}{4} \right)^2 \Sigma_0 = \frac{\pi^3 r_{\text{sh}}^2 \Sigma_0}{\eta^2}. \quad (3.48)$$

We transform Eq. 3.47 using the Eq. 3.48 getting the resulting mass spectrum in a form

$$dN \sim -\frac{\pi^2 r_{\text{sh}}^2 \Sigma_0}{4m^2} \left[I_f(m) - m^{1/2} \frac{dI_f(m)}{dm} \right] dm . \quad (3.49)$$

We use the thin-shell approximation (Eq. 4.10) with the continuous energy input to determine the dynamical parameters of the shell r_{sh} , v_{sh} and Σ_0 . We numerically integrate ω_η for each unstable mode η from the beginning of the instability at this mode, obtaining the fragmentation integral $I_f(\eta, t)$. We transform it from the dependence on η to the dependence on m at a certain time. Inserting it to the Eq. 3.49 we obtain the mass spectrum.

The mass spectra of shells with various physical parameters at time $t = 5t_b$ are shown by Fig. 3.3. Their middle- and high-mass parts can be approximated by the power-law $dN/dm \sim m^{-\alpha}$, where α is the mass spectrum index. The previously described analysis yields

$$\alpha = 2.3 - 2.4 . \quad (3.50)$$

The physical parameters of the shell determines the mass interval of fragments. The mass m_{max} of the fastest growing fragments, which appropriates to the wave-number η_{max} , at time t_b depends on the parameters as follows

$$m_{\text{max}} \sim G^{-2} c_{\text{sh}}^{29/8} L^{-1/8} n^{-1/2} \mu^{-1/2} . \quad (3.51)$$

The dependence on the power of the energy source L is weak. The sound-speed in the shell is more important parameter, but it seems that the physically possible range of values is relatively narrow (0.3 – 3 km/s). The most important parameter, which determines the mass of the created fragments is the density of the ambient medium given by parameter n_0 .

In the low density medium ($n_0 \sim 0.1 - 1 \text{cm}^{-3}$), fragments with mass $10^4 - 10^7 M_\odot$ are created, which corresponds to the typical mass of molecular clouds in galaxies. On the other hand, the fragments with stellar masses ($10^{-1} - 10^3$) are created in density $10^6 - 10^7 M_\odot$, typical for the dense cores of the molecular clouds, where new stars are formed.

Fig. 3.4, left panel, shows the typical dependence of the mass spectrum index on time. It relaxes to the value 2.3 – 2.4 at time $t = 3 - 4t_b$ and then it remains constant.

It is interesting to compare the mass spectrum of the expanding shell to the mass spectra obtained by similar procedure, but in different physical situation. For this purpose we use the scale-free instability and the Jeans instability.

In the case of the scale-free instability the perturbations grow with the constant rate ω , independently on the wave-number k . The number of fragments of wavelength λ within the volume of radius R is

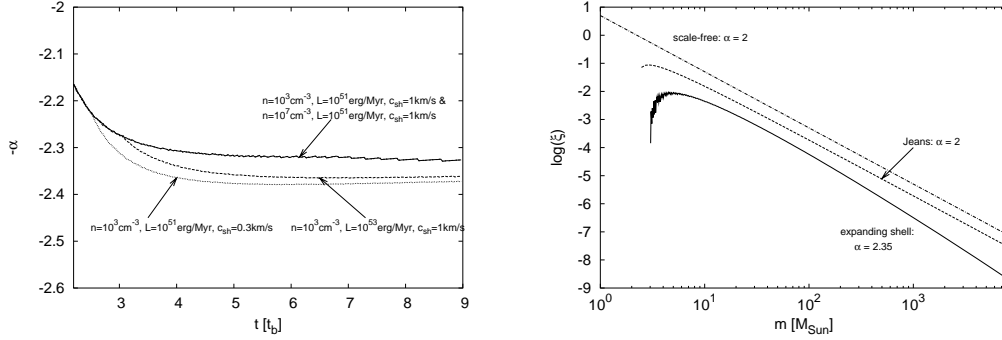


Figure 3.4: Left: The time dependence of the mass spectrum index α for shells with various physical parameters. Right: The mass spectrum of the expanding shell comparing to the spectra of the scale-free instability and the Jeans instability.

$$N = \omega \times \frac{R^3}{(\lambda/4)^3} = \frac{8\omega R^3 k^3}{\pi^3}, \quad (3.52)$$

where we have used $k = 2\pi/\lambda$. Since ω does not depend on time, we can use it instead of the fragmentation integral. The mass m of a fragment of wavelength λ is

$$m = \frac{4}{3}\pi(\lambda/4)^3\rho = \frac{1}{6}\pi^4\rho k^{-3}, \quad (3.53)$$

where ρ is the density of the homogeneous medium. Combining the Eqs. 3.52 and 3.53 we get

$$dN = \frac{24\omega R^3 k^2}{\pi^3} dk = -\frac{4}{3}\pi R^3 \rho \omega m^{-2} dm. \quad (3.54)$$

The mass spectrum of the scale-free instability is a power-law $dN/dm \sim m^{-\alpha}$ with the mass spectrum index $\alpha = 2$.

The perturbation growth rate in the case of the Jeans instability is given by the dispersion relation (see e.g. Binney & Tremaine, 1987)

$$\omega(k) = \sqrt{-c_s^2 k^2 + 4\pi G\rho}, \quad (3.55)$$

where ρ is the density of the medium, c_s is the sound-speed in it and G is the constant of gravity. The appropriate mass spectrum has a form

$$dN = -\frac{16}{9}R^3\rho m^{-2} \left[-c_s^2 \left(\frac{\pi^4\rho}{6m} \right)^{2/3} + 4\pi G\rho \right]^{1/2} dm \quad (3.56)$$

Fig. 3.4, right panel, compares the mass spectrum of the expanding shell to the spectra of the scale-free instability and the Jeans instability. More

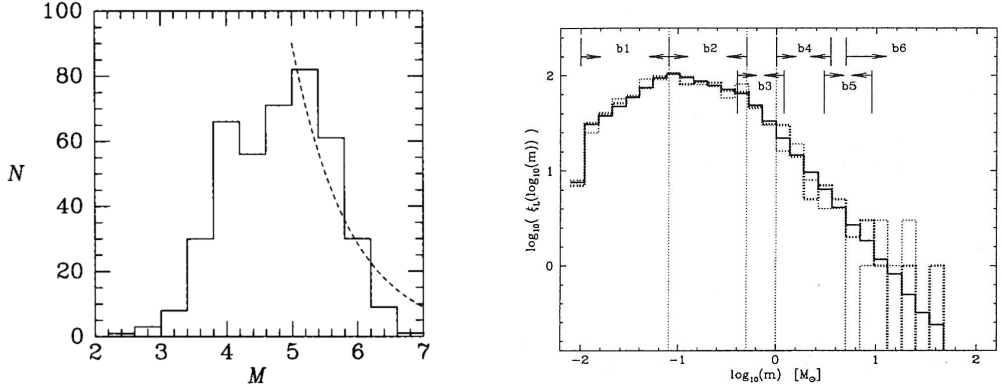


Figure 3.5: Left: The mass spectrum of Galactic molecular clouds. The dashed line represents the power-law with slope $\alpha = 1.5$ (borrowed from Binney & Merrifield, 1998). Right: The universal IMF of stars according to Kroupa (2001). It can be approximated by multiple-part power-law with slopes $\alpha = 0.3 \pm 0.7$ for $m \in (0.01, 0.08) M_{\odot}$, $\alpha = 1.3 \pm 0.5$ for $m \in (0.08, 0.5) M_{\odot}$, $\alpha = 2.3 \pm 0.3$ for $m \in (0.5, 1.0) M_{\odot}$ and $\alpha = 2.3 \pm 0.7$ for $m > 1.0 M_{\odot}$.

detailed analysis (see Palouš et al., 2003) shows that the harder spectrum of the expanding shell is due to the fact that it is the gravitational instability of the 2D structure (shell) in 3D space and due to the expansion, which destroys the larger fragments more effectively than the smaller ones.

Finally, we compare the mass spectrum of expanding shells to the observed mass spectrum of GMC and to the IMF of stars. Mass spectrum of the GMC in the Milky Way is flatter, with mass spectrum index $\alpha = 1.5 - 2.0$ (see Fig. 3.5, left panel). It may be due to collisions and merging, which always decrease the number of low-mass fragments and increase the number of high-mass fragments changing the slope of the mass spectrum to less steep. The gravitational instability time t_b in the low-density medium ($n_0 = 10^{-1} - 1 \text{ cm}^{-3}$) is typically 10-100 Myr, which is greater/similar to the average collisional time-scale of GMC (Tan, 200).

The initial mass function of stars is shown in Fig. 3.5, right panel. Its shape is similar to the obtained mass spectrum of the expanding shell, with mass spectrum index $\alpha = 2.3$ at its high-mass end. This is due to the fact that the average collisional time of the fragments is longer by factor $10^1 - 10^3$ than the gravitational instability time $t_b \sim 10^3 - 10^4$ yr and the potential merging does not play an important role like in the case of GMC (see Elmegreen & Shadmehri, 2002).

Chapter 4

The ZEUS code

4.1 Introduction

ZEUS is a widely used code for astrophysical fluid dynamics simulations. It was written by Stone and Norman (1992), the last official version 3.4.2 was released in August 1995. ZEUS was developed at the Laboratory for Computational Astrophysics (LCA) which is a joint project of the National Centre for Supercomputer Applications and the Department of Astronomy of the University of Illinois at Urbana-Champaign. The source code is available at http://zeus.ncsa.uiuc.edu:8080/lca_intro_zeus3d.html and it is distributed under the royalty free licence.

The code is based on the methods of finite differences and finite volumes, which are simple, fast and robust. All equations are discretized with the second order accuracy. An advantage of these techniques is that they can be easily extended to other physical processes. The basic equations of the code are written in a covariant form which allows the use of the code in an arbitrary orthogonal coordinate system (Cartesian, cylindrical and spherical coordinates are predefined). ZEUS also includes modules for solving magneto-hydrodynamic equations and the radiation transfer equation.

A substantial advantage is sufficiency of good documentation. A detailed description of the ZEUS code can be found in Stone & Norman, 1992a (HD), Stone & Norman, 1992b (MHD) and Stone & Norman, 1992c (RTE), these articles includes also basic tests of the code. The ZEUS3D distribution includes a User manual (Clarke et al., 1994), other useful information can be found in Norman & Stone (1994).

ZEUS has also some limitations and drawbacks. Several artificial effects, e.g. the imprint of the grid to the computation, are discussed in Chapter 6. Some drawbacks are connected to the technological background of the code.

ZEUS is written in FORTRAN77 which is an old programming language and is very impractical for such a big project (over 45,000 lines of code) – it is impossible to define user data structures, exchange of data through the common blocks is not very transparent, memory cannot be allocated dynamically and so on. The source code management of ZEUS is another thing which we have found problematic. The source code of ZEUS is generated automatically from the original code and user change-decks held in separate files. It makes the orientation in larger changes difficult.

We have also found several bugs in the code, they are described in Section 4.11. The patches are available at <http://richard.wunsch.matfyz.cz/zeus/>.

In this chapter we give a brief description of ZEUS and our modifications and add-ons.

4.2 Basic equations

Although ZEUS is able to solve full set of MHD equations, we only use the part which solves pure hydrodynamic equations. Therefore, we focus on the description of the HD algorithm.

HD equations can be written in a following form:

$$\frac{D\rho}{Dt} + \rho \nabla \cdot \mathbf{v} = 0 \quad (4.1)$$

$$\rho \frac{D\mathbf{v}}{Dt} = -\nabla p - \rho \nabla \Phi \quad (4.2)$$

$$\rho \frac{D}{Dt} \left(\frac{e}{\rho} \right) = -p \nabla \cdot \mathbf{v} \quad (4.3)$$

where D/Dt denotes the comoving derivative

$$\frac{D}{Dt} = \frac{\partial}{\partial t} + \mathbf{v} \cdot \nabla . \quad (4.4)$$

Dependent variables are mass density ρ , fluid velocity v and internal energy density e . Φ is the gravitational potential, which can be set externally in the form of an analytical function or determined from the space distribution of the mass by the Poisson solver (see Chapter 5). The set of the HD equations is closed by the equation of state connecting pressure p to the internal energy density (and the mass density in general). We use the equation of state of the ideal gas in the form:

$$p = (\gamma - 1)e \quad (4.5)$$

where $\gamma = 5/3$ is a polytropic index.

4.3 The HD algorithm

ZEUS solves the fluid equations using the operator split method. If we have an equation in a form

$$\frac{\partial y}{\partial t} = \mathcal{L}(y) , \quad (4.6)$$

where operator \mathcal{L} can be split into several parts $\mathcal{L} = \sum_{i=1}^n \mathcal{L}_i$, we can search for the solution with the procedure

$$\begin{aligned} (y^1 - y^0)/\Delta t &= \mathcal{L}_1(y^0) \\ (y^2 - y^1)/\Delta t &= \mathcal{L}_2(y^1) \\ &\dots \\ (y^n - y^{n-1})/\Delta t &= \mathcal{L}_n(y^{n-1}) \end{aligned} \quad (4.7)$$

Numerical experiments have shown that such a multistep solution procedure is more accurate than a single integration step based on old data (Stone & Norman, 1992a, Hawley, et al., 1984 and Norman & Winkler, 1986).

ZEUS solves the Eqs. 4.1 – 4.3 in two substeps, called a source step and a transport step. In the source step the finite-difference approximation to the equations:

$$\rho \frac{\partial \mathbf{v}}{\partial t} = -\nabla p - \rho \nabla \Phi - \nabla \cdot \mathbf{Q} \quad (4.8)$$

$$\frac{\partial e}{\partial t} = -p \nabla \cdot \mathbf{v} - \mathbf{Q} : \nabla \mathbf{v} \quad (4.9)$$

is solved, i.e. the fluid velocity is corrected on pressure and gravity forces and the pressure work is performed on the gas internal energy. \mathbf{Q} is the tensor of the artificial viscosity (see Section 4.5), the colon denotes a double scalar product of two tensors ($\mathbf{A} : \mathbf{B} = \sum_{i,j} a_{ij} b_{ij}$ in Cartesian coordinates).

In the transport step the set of following integral equations is solved

$$\frac{d}{dt} \int_V \rho dV = - \int_{dV} \rho (\mathbf{v} - \mathbf{v}_g) \cdot \mathbf{dS} , \quad (4.10)$$

$$\frac{d}{dt} \int_V \rho \mathbf{v} dV = - \int_{dV} \rho \mathbf{v} (\mathbf{v} - \mathbf{v}_g) \cdot \mathbf{dS} , \quad (4.11)$$

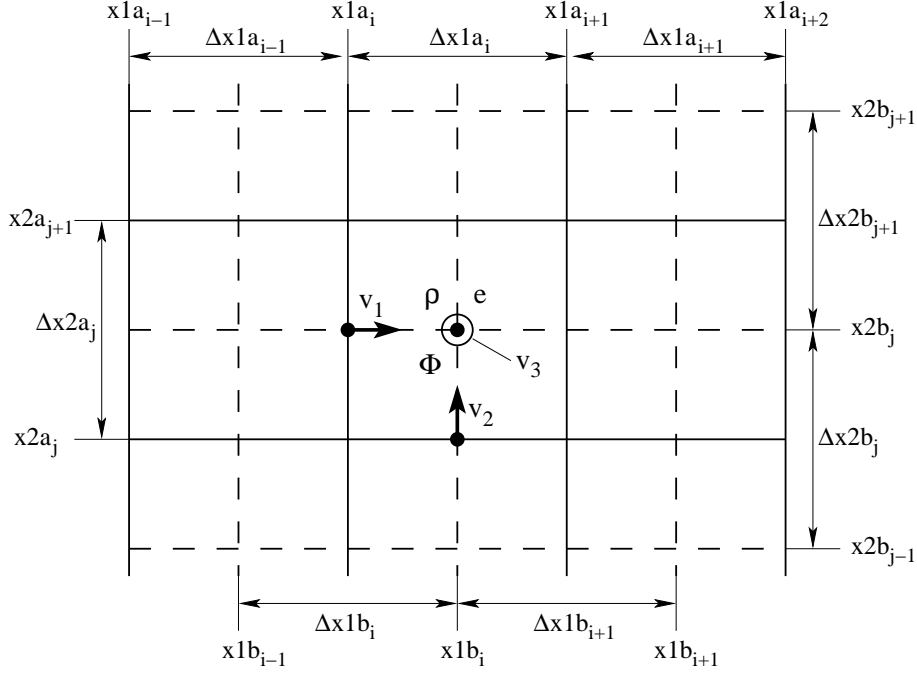


Figure 4.1: The ZEUS grid. The solid lines denote the a-grid, while the dashed lines denote the b-grid.

$$\frac{d}{dt} \int_V e dV = - \int_{dV} e(\mathbf{v} - \mathbf{v}_g) \cdot d\mathbf{S} . \quad (4.12)$$

They describe an advection of mass, momentum and internal energy, respectively, through the computational mesh. \mathbf{v}_g denotes the grid velocity (ZEUS allows the moving grid, however, we do not use this technique). In ZEUS, three methods for solving Eqs. 4.10 – 4.12 are implemented: the first-order-accurate donor-cell method (Godunov, 1959), the second-order van Leer method (van Leer, 1977) and the third-order piecewise parabolic advection (PPA) method (Colella & Woodward, 1984). After some numerical experiments we have decided to use the van Leer method, because it offers the best ratio of precision to computational costs.

The finite-difference method is based on the discretization of each dependent variable over the spatial computational domain. Then finite-difference approximations (algebraic equations) to the differential equations are solved on this discrete mesh. ZEUS uses a staggered mesh built up of two mutually shifted grids. The a-grid specifies positions of the zone boundaries while the b-grid specifies the zone centres. Discrete values of all dependent variables are stored for each zone. Scalars are stored at the zone centres while compo-

nents of vectors are stored at the appropriate zone interfaces (see Fig. 4.1).

4.4 The coordinate system

The ZEUS code is designed to work in an arbitrary orthogonal coordinate system. The particular coordinate system is described by the diagonal metric tensor with the scale factors (h_1, h_2, h_3) . They can be used to write all operators which appear in the dynamic equations in a coordinate-independent fashion. The scale factors of the three predefined coordinate systems are

$$\begin{aligned} \text{Cartesian : } & (x_1, x_2, x_3) = (x, y, z) , & (h_1, h_2, h_3) &= (1, 1, 1) \\ \text{cylindrical : } & (x_1, x_2, x_3) = (z, r, \phi) , & (h_1, h_2, h_3) &= (1, 1, r) \\ \text{spherical : } & (x_1, x_2, x_3) = (r, \theta, \phi) , & (h_1, h_2, h_3) &= (1, r, r \sin \theta) . \end{aligned} \quad (4.13)$$

In general, each scale factor can be a function of all coordinates. However, in ZEUS, they are supposed to be of the form

$$\begin{aligned} h_1 &= g_1 \equiv 1 \\ h_2 &= f(x_1) = g_2 \\ h_3 &= f(x_1)f(x_2) = g_{31} g_{32} , \end{aligned} \quad (4.14)$$

in order to reduce the memory requirements and floating point operations. The new scale factors are defined on both a- and b-grid, so there are six 1D arrays which define the coordinate system g_{2a_i} , g_{31a_i} , g_{32a_j} , g_{2b_i} , g_{31b_i} and g_{32b_j} .

The standard way of differencing equations, i.e. replacing derivatives $\partial F/\partial x$ with formulas $\Delta F/\Delta x$, cannot be used with curvilinear coordinates. The reason is the possibility of large numerical errors when differencing near the coordinate singularities. This problem can be eliminated by differencing with respect to coordinate volume rather than coordinate distance. For instance, if we discretize dynamical equations in spherical coordinates using the formula

$$\frac{1}{r^2} \frac{\partial}{\partial r} (r^2 F) \sim \frac{\Delta(r^2 F)}{r^2 \Delta r} = \frac{r_i^2 F_i - r_{i-1}^2 F_{i-1}}{[(r_i + r_{i-1})/2]^2 (r_i - r_{i-1})} , \quad (4.15)$$

then near the origin there is a serious discrepancy between this result and the volume difference formula

$$\frac{1}{r^2} \frac{\partial}{\partial r} (r^2 F) \sim \frac{\Delta(r^2 F)}{\Delta(r^3/3)} = \frac{r_i^2 F_i - r_{i-1}^2 F_{i-1}}{r_i^3/3 - r_{i-1}^3/3}, \quad (4.16)$$

which expresses much better the physical meaning of the original differential operator. The general method of differencing conservation laws on a non-Cartesian mesh is described in (Mönchmeyer & Müller, 1989).

In ZEUS, there are introduced the volume factors

$$\begin{aligned} \text{Cartesian : } & \quad dvl1 = \Delta x, \quad dvl2 = \Delta y, \quad dvl3 = \Delta z \\ \text{cylindrical : } & \quad dvl1 = \Delta z, \quad dvl2 = \Delta(r^2/2), \quad dvl3 = \Delta\phi \\ \text{spherical : } & \quad dvl1 = \Delta(r^3/3), \quad dvl2 = \Delta(-\cos\theta), \quad dvl3 = \Delta\phi, \end{aligned} \quad (4.17)$$

which are, like the scale factors, defined on both the a- and b-grid. Using them, the derivatives in the dynamical equations are replaced with differences as follows:

$$\frac{1}{h_2 h_3} \frac{\partial F}{\partial x_1} \rightarrow \frac{1}{g_{32}} \frac{\Delta F}{dvl1}, \quad \frac{1}{h_3} \frac{\partial F}{\partial x_2} \rightarrow \frac{1}{g_{31}} \frac{\Delta F}{dvl2}, \quad \frac{\partial F}{\partial x_3} \rightarrow \frac{\Delta F}{dvl3} \equiv \frac{\Delta F}{\Delta x_3}. \quad (4.18)$$

4.5 Artificial viscosity

There are two kinds of artificial viscosity in the ZEUS code. The non-linear Neumann-Richtmyer is used to treat shocks. It is based on an analysis of planar shocks in one dimension (Neumann & Richtmyer, 1950) and is extended to multi-dimensions by defining the coefficients in each direction independently. The tensor of the artificial viscosity \mathbf{Q} is diagonal, composed of artificial pressures q_i defined as

$$q_i^{\text{NR}} = \begin{cases} l_i^2 \rho (\partial v_i / \partial x_i)^2 & \text{if } (\partial v_i / \partial x_i) < 0 \\ 0 & \text{otherwise} \end{cases} \quad (4.19)$$

where $l_i = C_2 \Delta x_i$ is a distance over which the artificial viscosity spreads the shock, and is typically chosen to be $C_2 = 3$. The sensitivity of the artificial non-linear viscous pressure only to compression ensures the correct entropy jump across shocks and the correct shock propagation velocity (Neumann & Richtmyer, 1950). The artificial viscosity defined in this way has a negligibly small effect away from shocks.

The second one is the linear artificial viscosity. It is sensitive to both compression and expansion, the linear artificial viscosity pressures are defined as

$$q_i^{\text{lin}} = C_1 \rho c_s \Delta v_i, \quad (4.20)$$

where C_1 is a constant of order unity and c_s is the adiabatic sound-speed ($c_s = \gamma p / \rho$). The linear artificial viscosity is used to damp oscillations in stagnant flows (we use it to damp sound-waves propagating in the interior of the shell).

4.6 Boundary conditions

Boundary conditions are implemented as two layers of ghost zones at each boundary of the computational domain. They are necessary to determine the spatial differences of the dependent variables here (two layers are required for higher order interpolation if the PPA method is used). Values of the dependent variables in the ghost zones are given by simple, explicit equations (which, for instance, may connect these value to the values in the adjacent active zones). In ZEUS, the form of these boundary condition equations can be chosen as one of the following types independently for each dependent variable and each boundary:

Reflecting boundary conditions: all zone centred variables and the tangential components of velocity in the ghost zones are set to the values of the corresponding active zones. The normal component of velocity is set to zero at the boundary and reflected in the second ghost zone.

Axis of symmetry / central point: the same as previous in Cartesian coordinates; in cylindrical coordinates Φ -components are inverted at inner R -boundary (the axis of symmetry); in spherical coordinates θ - and ϕ -components are inverted at inner r -boundary (the central point) and ϕ -components are inverted at inner and outer θ -boundary (the axis of symmetry).

Inflow boundary conditions: all dependent variables in the ghost zones are set to the user defined values (which may be time-dependent).

Outflow boundary conditions: the values of all variables in the ghost zones are set equal to the values in the corresponding active zones. This simple implementation of the outflow boundary conditions may cause the unwanted reflections of sound-waves.

Periodic boundary conditions: all dependent variables except the normal component of velocity at the boundary are set to the corresponding active zones on the opposite side of the grid. The normal component of velocity at the boundary is computed from the difference equations.

4.7 Time-step control

It can be shown by performing von Neumann stability analysis of the dynamical equations (Richtmyer & Morton, 1957) that the time-step must be limited by the Courant-Friedrichs-Lewy (CLF) condition to maintain stability (otherwise artificial short wavelength oscillations occur)

$$\Delta t \leq \min \frac{\Delta x}{|\mathbf{v}| + c_s}, \quad (4.21)$$

where v is the local fluid velocity and c_s is the adiabatic sound-speed. The minimum is taken over all grid zones. Physically, it means that the maximum distance which information can travel in one time-step must be smaller than a size of a grid zone.

In ZEUS the time-step is computed using the explicit formula

$$\Delta t = \frac{C_0}{\max(\delta t_c^{-2} + \delta t_1^{-2} + \delta t_2^{-2} + \delta t_3^{-2} + \delta t_q^{-2})}, \quad (4.22)$$

where C_0 is the safety factor, so called Courant number (it can be chosen between 0 and 1, typically $C_0 = 0.5$). The sound-speed time-step is defined as

$$\delta t_c = \frac{\min(\Delta x_1, \Delta x_2, \Delta x_3)}{c_s}, \quad (4.23)$$

while fluid velocity time-steps are

$$\delta t_i = \frac{\Delta x_i}{\mathbf{v}_i - \mathbf{v}_{\mathbf{g},i}}, \quad \text{where } i = 1, 2, 3. \quad (4.24)$$

Finally, we need to add the limitation of the time-step due to the artificial viscosity, the artificial viscosity time-step is

$$\Delta t \leq \frac{(\Delta x)^2}{4\nu}, \quad (4.25)$$

where ν is the coefficient of the kinematic viscosity. It can be determined by comparison of artificial viscosity terms to the viscous terms in Navier-Stokes equations. For Neumann-Richtmyer artificial viscosity we get

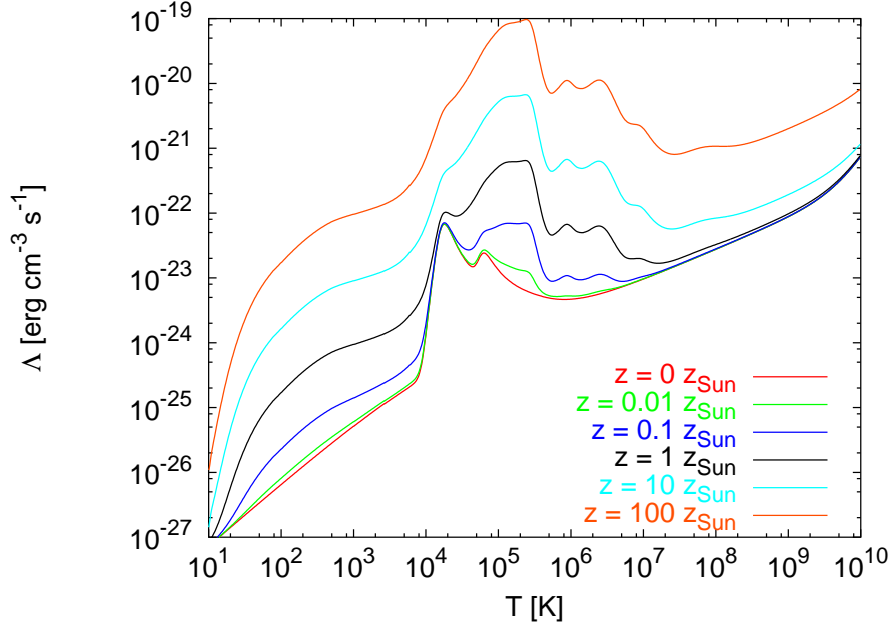


Figure 4.2: The used cooling function.

$$\delta t_q = \min \left(\frac{\Delta x_1}{4C_2 \Delta v_1}, \frac{\Delta x_2}{4C_2 \Delta v_2}, \frac{\Delta x_3}{4C_2 \Delta v_3} \right) \quad (4.26)$$

where C_2 is the constant determining the artificial viscosity strength defined in section 4.5.

4.8 Radiative cooling

The radiative cooling of the interstellar gas is an important microscopic process, which is necessary to take into account, if we want to simulate the thin, cool and dense shell. The process is initiated by an excitation of atomic, ionic or molecular transitions during collisions, which is followed by a radiative deexcitation. Then, if the medium is optically thin, the radiated photon escapes away.

The rate at which the gas loses its energy can be approximated by the equation

$$\left(\frac{de}{dt} \right)_{\text{cool}} = -\rho^2 \Lambda(T, z), \quad (4.27)$$

it depends on the second power of the mass density (transitions are induced by the collisions) and the cooling function $\Lambda(T, z)$. It is the complicated function of temperature T and chemical composition, which is described by the metallicity z . To calculate the cooling function, it is necessary to know the collisional excitation cross-sections of included particles as functions of temperature. The cooling function was computed by many authors, for instance Shapiro & Moore (1976) or Böhringer & Hensler (1989).

The cooling function implemented in the official distribution of ZEUS is taken from the work by MacDonald & Bailey (1981), which is based on the cooling function Shapiro & Moore, 1976. Since we had some problems with this implementation (the Newton-Raphson iteration did not use to converge during the fast thermal collapse of the shell), we had to rewrite this part of the code, so we have decided to use a more up-to-date cooling function. Fig. 4.2 shows the cooling function we use in the simulations of the expanding shells. It was created by T. Płewa using the code Cloudy (Ferland, 2000 and Ferland & Savin, 2003) and it was kindly provided by Prof. Różyczka.

The implementation of the cooling into the HD algorithm means to include the additional term into the equation for energy 4.3.

$$\rho \frac{D}{Dt} \left(\frac{e}{\rho} \right) = -p \nabla \cdot \mathbf{v} - \rho^2 \Lambda(T, z) . \quad (4.28)$$

The contribution of the cooling term is added in the source substep, which consists of two subsubsteps following the operator split procedure. In the first subsubstep, the intermediate value of internal energy e^{n+b} is obtained adding the artificial viscosity dissipation using the difference scheme

$$\frac{e^{n+b} - e^n}{\Delta t} = (\mathbf{Q} : \nabla \mathbf{v}) . \quad (4.29)$$

The change of the internal energy due to compression/expansion of the gas is added in the second subsubstep, which in adiabatic case (without cooling) has a form

$$\frac{e^{n+1} - e^{n+b}}{\Delta t} = p^{n+1/2} \nabla \cdot \mathbf{v} , \quad (4.30)$$

where the time-centred pressure $p^{n+1/2} = (p^{n+b} + p^{n+1})$ is used to maintain the second-order accuracy of the code. Using the equation of state $p = (\gamma - 1)e$, the Eq. 4.30 can be rearranged to give an explicit expression for e^{n+1}

$$e^{n+1} = \frac{1 - (\Delta t/2)(\gamma - 1)\nabla \cdot \mathbf{v}}{1 + (\Delta t/2)(\gamma - 1)\nabla \cdot \mathbf{v}} e^{n+b} . \quad (4.31)$$

Unfortunately, the previous operation is impossible if we include the cooling term. The cooling function depends on temperature, which is a function of internal energy. If we want to use the time centred internal energy to calculate temperature and the cooling rate (and we need it to maintain the second-order accuracy), the only possibility is to search for the solution of the implicit equation

$$\frac{e^{n+1} - e^{n+b}}{\Delta t} = p^{n+1/2} \nabla \cdot \mathbf{v} - \rho^2 \Lambda(T^{n+1/2}, z) \quad (4.32)$$

numerically, because the cooling function is defined as a table of values.

The gas in the expanding shell cools very quickly, in particular during the thermal collapse phase. This often caused that the Newton-Raphson iteration used in the original ZEUS cooling routine did not converge to the correct solution. Therefore we have changed the routine to use the Brent algorithm (Press et al., 1992). It should be as fast as the Newton-Raphson iteration, but the convergence is guaranteed.

Nevertheless, the solution of Eq. 4.32 leads to negative energies in exceptional cases during the thermal collapse – it is because the slope of the cooling function changes a lot during one time-step, and the cooling rate in the central time-point is overestimated. The proper solution of this problem should be reducing the time-step. However, it would be very "uneconomical" to compute the whole domain with the extremely small time-steps due to problems in several zones. Moreover, we are not interested in the exact description of the thermal collapse for which we have insufficient spatial resolution anyway. We use the simple work-around: the internal energy in zones, where the negative energy occurs due to overestimated radiative cooling, is set to the half of the value at the beginning of the time-step. This "dirty trick" must be applied only in a short period (several time-steps) of the thermal collapse. We have checked how it influenced the evolution of the shell. It seemed that the only effect was a bit slower thermal collapse of the shell. In the later stage of the shell evolution, there were no differences detected between the simulation using this trick and the simulation with the reduced time-step.

4.9 Heating

The real interstellar gas is heated by starlight, cosmic rays, X-rays and other physical mechanisms. We need to insert this process in our model to maintain the ambient medium of the shell at some realistic temperature (otherwise it cools quickly by the radiative cooling). As the ambient medium is not the

main subject of our interest, we can use very simple approximation assuming that the heating is proportional to the mass density

$$\left(\frac{de}{dt}\right)_{\text{heat}} = H_0 \rho , \quad (4.33)$$

where H_0 is the constant. Its value can be determined demanding the cooling and heating of the ambient medium be in equilibrium

$$H_0 \rho_0 = \rho_0^2 \Lambda(T_0) \quad \Rightarrow \quad H_0 = \rho_0 \Lambda(T_0) , \quad (4.34)$$

where ρ_0 and T_0 are density and temperature of the ambient medium. Heating defined in such way has a negligible effect in the shell, where the density is high and the cooling dominates. The effect of heating in the shell interior is also small due to the low density of the gas.

4.10 Additional pressure

The hydrodynamic simulation of the shell with the radiative cooling leads to the extremely (and unrealistically) thin shell.

Density in the shell is so high and the radiative cooling so effective that the shell cools below one hundred Kelvins. The low pressure leads to the shell which is only several grid-zones thick. This thickness is artificial, because the resolution is usually insufficient to make the shell dense enough to balance the pressure with its surroundings. However, in reality the magnetic field and/or the turbulence increase the pressure and thickness of the shell. These processes have to be accounted for if the pressure in the shell should be realistic.

We can use the magnetic pressure or the turbulent pressure (or both). Finally, we have decided to use the turbulent pressure, because the implementation was easier and the definition of the turbulent pressure was more suitable for the comparison to the analytical approach.

If the system scales exceed the scale of turbulence, the turbulence can be included as an additional pressure by defining the effective sound-speed

$$c_{s,\text{eff}}^2 = c_s^2 + \frac{v_{\text{rms}}^2}{3} , \quad (4.35)$$

where v_{rms} is the root mean square velocity of the random motions due to turbulence (e.g. Klessen, 2003 or Chandrasekhar, 1949). The effective turbulent pressure is defined as

$$p_{\text{eff}} = \rho c_{s,\text{eff}}^2 . \quad (4.36)$$

To include the additional pressure into ZEUS we can simply define a parameter $c_{add} = v_{\text{rms}}/3$ and add the quantity $p_{\text{add}} = \rho c_{\text{add}}^2$ to the thermal pressure.

We also need to change the definition of the sound-speed time-step (Eq. 4.23) to the form

$$\delta t_c = \frac{\min(\Delta x_1, \Delta x_2, \Delta x_3)}{c_{\text{s,eff}}} . \quad (4.37)$$

The advantage of this approach is that c_{add} is a free parameter, which can be compared to parameter c_{sh} (sound-speed in the shell) in the analytical model.

4.11 Patches

Finally, we give a list of patches that correct some bugs and problems in the ZEUS code. They may be used with the ZEUS v.3.4.2 only and are available at <http://richard.wunsch.matfyz.cz/zeus/>.

TEA: There are two possibilities how to handle the energy equation in ZEUS. The first one is described above (section 4.2), the energy equation is written for the internal energy, which is also the quantity transported between the zones. The second possibility is to advect the total energy and use the energy equation in a form $De_{\text{tot}}/Dt = 0$, where e_{tot} denotes the total energy. The later approach ensures the energy conservation to the machine roundoff, contrary to the former one, but negative pressures may occur. In ZEUS v.3.4.2 there is a bug – the artificial viscosity term is added to the right hand side of the equation for energy. The patch corrects this problem.

TEA_tslice: The routine `tslice`, which outputs some data, does not work correctly if the total energy advection is used. We fix it by this patch.

mddb_cool: This corrects the value of the normalisation factor of the cooling function used in the original ZEUS code (MacDonald & Bailey, 1981). The value was underestimated by the factor of ten.

hdf_vect: The values of the vector components, which are set on the a-grid, are written with the b-grid values without any interpolation to the hdf (Hierarchical Data Format) output files. It is mentioned in the documentation, so it is not clear, whether it is a bug or a feature. Nevertheless, we have created the patch, which stores these vector components with the correct coordinates.

neg_en: If the total energy advection scheme is used, negative pressures and internal energies can occur, and if also the cooling is used, it may lead to the artificial instabilities. We fix this problem by setting the values of the internal energy in these zones to a small positive value. This of course violates the energy conservation law, but the deviation is usually smaller than if the internal energy advection scheme (which ensures positive internal energies) is used.

Chapter 5

Poisson solver

5.1 Overview of methods

The preceding chapter was devoted to the ZEUS code – the solver of the hydrodynamic equations including the effects of radiative cooling, heating and turbulent pressure. The last unknown variable is the gravitational potential Φ , which appears on the RHS of the Euler’s equation 4.2.

If we want to know the self-gravity of the system, we need the Poisson solver – the code, which determines the gravitational potential field from the spatial distribution of the mass density ρ , solving the Poisson equation

$$\nabla^2\Phi = 4\pi G\rho , \tag{5.1}$$

where G is the constant of gravity. The Poisson equation is the elliptical partial differential equation of the second order. The gravitational potential is determined not only by the mass density ρ , but also by the boundary conditions, e.g. the values of Φ at all boundaries of the computational domain. This is therefore referred as *the boundary value problem*.

A lot of numerical methods has been developed to solve the boundary value problems, especially for elliptical equations as the Eq. 5.1. It is possible to distinguish two large categories: *direct methods* and *iterative* (or *relaxation*) *methods*.

Direct methods solve the Eq. 5.1 exactly in a finite number of arithmetic steps. The simplest of them is the Gaussian elimination of the system of linear equations arising if the Eq. 5.1 is differenced on some coordinate grid. This method is very ineffective and usually cannot be used for the real problems. More efficient methods are mostly based on the fast Fourier transform (FFT) or on the method of cyclic reduction. If N is the number of the grid zones, these methods require $O(N \log N)$ arithmetic operations, which is close to

the possible minimum $O(N)$.

Relaxation methods start with an initial guess for a solution, then they improve this approximation through successive iterations. If the method works properly, the sequence of approximations converges to the exact solution. Examples of these methods may be Jacobi method or Gauss-Seidel method and their variants (they are described in Section 5.2.2). Classical relaxation methods are easy to implement and may be applied to more general problems than most direct methods. On the other hand, many of these methods show some serious limitations. They quickly eliminate oscillatory (short wavelength, measured in zones of the grid) modes of error, but the smooth (long wavelength) modes of error converge very slowly. Moreover, this property become worse and worse as we use finer grids to increase the resolution. There are many methods that accelerate the convergence rate, for instance Dynamic Alternating Direction Implicit (DADI), which was used in the ZEUS2D code, or Conjugate Gradient method. Another example is a set of Multigrid methods, which evolve from attempts to overcome problems with the smooth modes. These methods count among the most efficient methods of solving elliptical equations and even more general problems. They are competitive with the fastest direct methods, but they are more general. Properly implemented multigrid methods may reach the best possible efficiency in the number of arithmetic operations $O(N)$.

In view of the fact that we need to solve the Poisson equation in every (or in almost every) hydrodynamic time-step, there is a good reason to use the relaxation method. A spatial distribution of the mass density typically does not change a lot during one time-step, so we can assume that the gravitational potential we compute is very similar to the gravitational potential from the previous time-step. Relaxation methods are able to use the solution from the previous time-step as an initial guess in the actual one, while direct methods throw all information away and start every time-step from scratch. Using the solution from the previous time-step can substantially accelerate the computation. Usually, there are only several iteration steps necessary to adjust the gravitational potential to a required precision.

At first we tried to port the DADI method from ZEUS2D to ZEUS3D. It worked acceptably in Cartesian coordinates, but the convergence rate in spherical coordinates was poor. Finally, we have decided to use the multigrid method, which should meet all our requirements. Additional reason was the fact that the algorithm was very elegant and an implementation of the multigrid method might be fun.

5.2 Iterative methods

5.2.1 Problem definition

We search for the solution of the Poisson equation, which can be formally written as

$$\nabla^2 u(x_1, x_2, x_3) = f(x_1, x_2, x_3) . \quad (5.2)$$

Both potential field u and right hand side f are set on the grid Ω defined as

$$\begin{aligned} \Omega &= \{(x_{1,i}, x_{2,j}, x_{3,k}), i \in \langle 0, L \rangle, j \in \langle 0, M \rangle, k \in \langle 0, N \rangle\} \\ u_{i,j,k} &= u(x_{1,i}, x_{2,j}, x_{3,k}), \quad f_{i,j,k} = f(x_{1,i}, x_{2,j}, x_{3,k}) . \end{aligned} \quad (5.3)$$

To solve Eq. 5.2, boundary conditions must be specified. For our purpose Dirichlet or periodic conditions will be appropriate. If Dirichlet boundary conditions are used, the values in the boundary planes are set to the values, which must be determined by some external mechanism, e.g. the multipole expansion.

$$\begin{aligned} u_{0,j,k} &= u_{iib,j,k} & u_{L,j,k} &= u_{oib,j,k} \\ u_{i,0,k} &= u_{ijb,i,k} & u_{i,M,k} &= u_{ojb,i,k} \\ u_{i,j,0} &= u_{ikb,i,j} & u_{i,j,N} &= u_{okb,i,j} \end{aligned} \quad (5.4)$$

($u_{iib,j,k}$ stands for *inner i-boundary*, $u_{oib,j,k}$ for *outer i-boundary*, $u_{ijb,i,k}$ for *inner j-boundary*, etc.). In the case of periodic boundary conditions, the values in the boundary planes are set to the corresponding values in the boundary plane on the opposite side of the grid:

$$\begin{aligned} u_{0,j,k} &= u_{L-1,j,k} & u_{L,j,k} &= u_{1,j,k} \\ u_{i,0,k} &= u_{i,M-1,k} & u_{i,M,k} &= u_{i,1,k} \\ u_{i,j,0} &= u_{i,j,N-1} & u_{i,j,N} &= u_{i,j,1} \end{aligned} \quad (5.5)$$

Next step is to determine the finite difference form of the Laplacian operator. It can be written in the ZEUS covariant formalism (see Section 4.4) as

$$\nabla^2 u = \frac{1}{h_1 h_2 h_3} \left[\frac{\partial}{\partial x_1} \left(\frac{h_2 h_3}{h_1} \frac{\partial u}{\partial x_1} \right) + \frac{\partial}{\partial x_2} \left(\frac{h_1 h_3}{h_2} \frac{\partial u}{\partial x_2} \right) + \frac{\partial}{\partial x_3} \left(\frac{h_1 h_2}{h_3} \frac{\partial u}{\partial x_3} \right) \right] \quad (5.6)$$

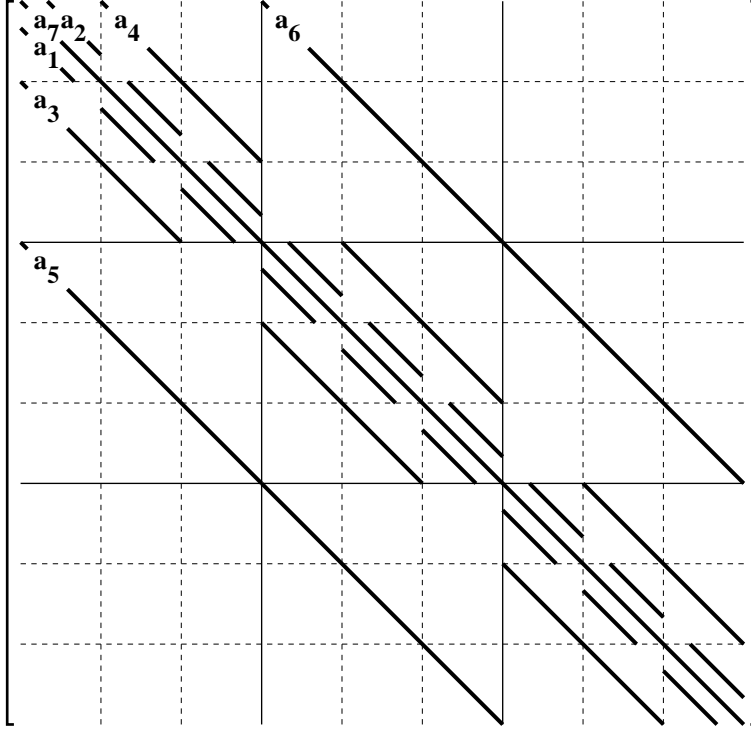


Figure 5.1: The structure of the matrix of the system of linear equations arising when the 7-point discretization scheme is used for the Poisson equation.

If we replace space derivatives in the Eq. 5.6 by their finite difference approximation according to the rules described in Section 4.4, we get so called 7-point discretization of the Poisson equation

$$\begin{aligned}
 & a_{1i}u_{i-1,j,k} + a_{2i}u_{i+1,j,k} + a_{3j}u_{i,j-1,k} + a_{4j}u_{i,j+1,k} + a_{5k}u_{i,j,k-1} + \\
 & + a_{6k}u_{i,j,k+1} + (a_{7i} + a_{7j} + a_{7k})u_{i,j,k} = f_{i,j,k} , \quad (5.7)
 \end{aligned}$$

where coefficients $a_{1i} - a_{7k}$ written in a covariant form are

$$\begin{aligned}
 a_{1i} &= \frac{g2a_i^2 g31a_i^2}{dvl1a_i dvl1b_i} & a_{2i} &= \frac{g2a_{i+1}^2 g31a_{i+1}^2}{dvl1a_i dvl1b_{i+1}} \\
 a_{3j} &= \frac{g32a_j^2}{g2b_i^2 dvl2a_j dvl2b_j} & a_{4j} &= \frac{g32a_{j+1}^2}{g2b_i^2 dvl2a_j dvl2b_{j+1}} \\
 a_{5k} &= \frac{1}{g31b_i^2 g32b_j^2 dvl3a_k dvl3b_k}
 \end{aligned}$$

$$\begin{aligned}
a_{6k} &= \frac{1}{g31b_i^2 g32b_j^2 dvl3a_k dvl3b_{k+1}} & (5.8) \\
a_{7i} &= -\frac{1}{dvl1a_i} \left(\frac{g2a_{i+1}^2 g31a_{i+1}^2}{dvl1b_{i+1}} + \frac{g2a_i^2 g31a_i^2}{dvl1b_i} \right) \\
a_{7j} &= -\frac{1}{g2b_i^2 dvl2a_j} \left(\frac{g32a_{j+1}^2}{dvl2b_{j+1}} + \frac{g32a_j^2}{dvl2b_j} \right) \\
a_{7k} &= -\frac{1}{g31b_i^2 g32b_j^2 dvl3a_k} \left(\frac{1}{dvl3b_{k+1}} + \frac{1}{dvl3b_k} \right)
\end{aligned}$$

As the Eq. 5.7 must be fulfilled in each grid zone, it represents a huge set of linear equations. If N is the number of grid zones, we have the set of N equations of a type

$$\mathbf{A}\mathbf{u} = \mathbf{f} , \quad (5.9)$$

where A is a matrix $N \times N$. Assuming a realistic grid $100 \times 100 \times 100$ we get the matrix of 10^{12} elements, if we store each element in double precision, this matrix would occupy 8 TB in the computer memory. Fortunately, the matrix is very sparse and it is not necessary to store the whole structure in the memory. The structure of the matrix A is shown by Fig. 5.1.

Let us define some quantities which are used in relaxation methods. Assuming \mathbf{v} is the computed approximation to the exact solution \mathbf{u} , we can define the *algebraic error* as

$$\mathbf{e} = \mathbf{u} - \mathbf{v} . \quad (5.10)$$

Unfortunately, it is impossible to use it to control the relaxation process, because it is uncomputable without the knowledge of the exact solution \mathbf{u} . The quantity suitable for measuring how well \mathbf{v} approximates \mathbf{u} is the *residual*

$$\mathbf{r} = \mathbf{f} - \mathbf{A}\mathbf{v} . \quad (5.11)$$

However, it should be used with a caution because although $\mathbf{r} = 0$ if and only if $\mathbf{e} = 0$ (it comes from the uniqueness of the solution 5.9), sometimes it may not be true that when $|\mathbf{r}|$ is small, $|\mathbf{e}|$ is also small.

If we insert Eqs. 5.10 and 5.11 into the linear system 5.9 we get the residual equation, an important relation between the error and the residual

$$\mathbf{A}\mathbf{e} = \mathbf{r} . \quad (5.12)$$

Alternatively, the relative error ϵ of the current approximation \mathbf{v} can be obtained by rearranging Eq. 5.7 so that

$$v'_{i,j,k} = \frac{1}{a_{7i} + a_{7j} + a_{7k}} (f_{i,j,k} - a_{1i}v_{i-1,j,k} - a_{2i}v_{i+1,j,k} - a_{3j}v_{i,j-1,k} - a_{4j}v_{i,j+1,k} - a_{5k}v_{i,j,k-1} - a_{6k}v_{i,j,k+1}) \quad (5.13)$$

and using the formula

$$\epsilon = \max_{i,j,k} \left| \frac{v'_{i,j,k} - v_{i,j,k}}{v_{i,j,k}} \right|. \quad (5.14)$$

5.2.2 Basic iterative schemes

One of the simplest schemes is the *Jacobi method*. The matrix A of the linear system 5.9 can be split into a diagonal and lower and upper triangular matrices as follows

$$A = D - L - U. \quad (5.15)$$

The advantage of this decomposition is that the diagonal matrix is easy to invert. We can rearrange term in the Eq. 5.9 to a form

$$\mathbf{u} = D^{-1}(L + U)\mathbf{u} + D^{-1}\mathbf{f} \quad (5.16)$$

and define the Jacobi iteration matrix

$$R_J = D^{-1}(L + U). \quad (5.17)$$

One iteration step can be written in a form

$$\mathbf{v}^{(1)} = R_J\mathbf{v}^{(0)} + D^{-1}\mathbf{f}, \quad (5.18)$$

where $\mathbf{v}^{(0)}$ denotes the current approximation and $\mathbf{v}^{(1)}$ is the new, updated approximation. When all components of $\mathbf{v}^{(1)}$ have been computed, the algorithm enters the next step, where $\mathbf{v}^{(1)}$ plays the role of $\mathbf{v}^{(0)}$. This procedure is repeated until a demanded precision of the solution is reached (in practice, it usually means the residual is small enough).

The *weighted Jacobi method* is a simple modification of the Jacobi method. The new approximation is $\mathbf{v}^{(1)}$ composed of two parts. The first one is the current approximation $\mathbf{v}^{(0)}$ and the second one is the approximation obtained by the standard Jacobi method. The parameter ω is used to set weights of these parts

$$\mathbf{v}^{(1)} = [(1 - \omega)I + \omega R_J]\mathbf{v}^{(0)} + D^{-1}\mathbf{f}. \quad (5.19)$$

Similarly, we can define the weighted Jacobi iteration matrix

$$R_{J\omega} = (1 - \omega)I + \omega R_J \quad (5.20)$$

and write the iteration scheme in a conventional form

$$\mathbf{v}^{(1)} = R_{J\omega}\mathbf{v}^{(0)} + D^{-1}\mathbf{f} . \quad (5.21)$$

The advantage of the weighted Jacobi method is the possibility of controlling the rate of relaxation. Convergence is guaranteed for all modes if $\omega \leq 1$. Values $\omega < 1$ enable us to accelerate the convergence of high-frequency modes, although the convergence of low-frequency modes is a bit slower (specially the best convergence rate of high-frequency modes is achieved if $\omega = 2/3$). The convergence of the low-frequency is very slow when using standard relaxation methods as the (weighted) Jacobi method, and it is extremely difficult to make it faster. Nevertheless, the idea of super-relaxation, i.e. $\omega > 1$, may be sometimes useful. Note that we have to take care about the high-frequency modes whose convergence is not guaranteed in this case.

The (weighted) Jacobi method has two disadvantages. As it computes all components of the new approximation before using any of them, it needs double space of memory to store the vector \mathbf{v} . The second problem is that the new information cannot be used as soon as it is available. Both these problems are solved in the *Gauss-Seidel method*. It simply overwrites the values of the approximation vector \mathbf{v} as soon as they are computed. In this case, the original system of equations is written in a form

$$(D - L)\mathbf{u} = U\mathbf{u} + \mathbf{f} , \quad (5.22)$$

which implies

$$\mathbf{u} = (D - L)^{-1}U\mathbf{u} + (D - L)^{-1}\mathbf{f} . \quad (5.23)$$

Using the Gauss-Seidel iteration matrix defined as

$$R_G = (D - L)^{-1}U , \quad (5.24)$$

the method scheme can be written in a form

$$\mathbf{v} \leftarrow R_G\mathbf{v} + (D - L)^{-1}\mathbf{f} , \quad (5.25)$$

where the left arrow stands for direct replacement of the \mathbf{v} -values.

The weighted Gauss-Seidel method can be defined in the same way as the weighted Jacobi method. There exists another important variant to this method – the *red-black Gauss-Seidel method*. In this strategy all points of

the grid are divided in two sets using the chessboard pattern. The red points are updated in the first substep, the black points in the second one. The advantage of this approach is that the points may be updated in any order, which is very useful property in terms of parallel computing. It is due to the fact that the red points need only the black points for their updating and vice versa.

5.2.3 The convergence rate

A measure of successfulness of a particular iterative method is its convergence rate. In this section we suggest how it is defined and connected to the form of the iteration matrix, specifically we show how it depends on the iteration matrix spectrum.

At first we form a general iteration scheme. Using the residual Eq. 5.12 and the definition of the algebraic error 5.10 we can write

$$\mathbf{u} - \mathbf{v} = A^{-1}\mathbf{r} . \quad (5.26)$$

If we identify \mathbf{v} with the current approximation $\mathbf{v}^{(0)}$ and \mathbf{u} with the new approximation $\mathbf{v}^{(1)}$, an iteration step may be formed as

$$\mathbf{v}^{(1)} = \mathbf{v}^{(0)} + B\mathbf{r}^{(0)} , \quad (5.27)$$

where B is an approximation to A^{-1} . The efficiency of the method depends on the quality of this approximation. The general iteration step 5.27 can be rewritten in a conventional form

$$\begin{aligned} \mathbf{v}^{(1)} &= R\mathbf{v}^{(0)} + B\mathbf{r}^{(0)} = \mathbf{v}^{(0)} + B(\mathbf{f} - A\mathbf{v}^{(0)}) \\ &= (I - BA)\mathbf{v}^{(0)} + B\mathbf{f} \equiv R\mathbf{v}^{(0)} + B\mathbf{f} \end{aligned} \quad (5.28)$$

where $R \equiv I - BA$ is the general iteration matrix. The m -th iteration has a form

$$\mathbf{v}^{(m)} = R^m\mathbf{v}^{(0)} + C\mathbf{f} \quad (5.29)$$

where $C(\mathbf{f}) = \sum_{i=0}^{m-1} R^i B\mathbf{f}$ represents a series of operations on \mathbf{f} .

All iteration method should be designed in the way so that the exact solution is the fixed point of the iteration, i.e. the iteration does not change it:

$$\mathbf{u} = R\mathbf{u} + C\mathbf{f} \quad (5.30)$$

Subtracting the last equation from the general iteration step 5.28, we get

$$\mathbf{e}^{(1)} = R\mathbf{e}^{(0)} \quad (5.31)$$

and after m iteration steps

$$\mathbf{e}^{(m)} = R^m \mathbf{e}^{(0)} . \quad (5.32)$$

Using the elementary property of vector and matrix norms we get the inequality

$$\|\mathbf{e}^{(m)}\| \leq \|R\|^m \|\mathbf{e}^{(0)}\| , \quad (5.33)$$

which means that the method converges if $\|R\| < 1$. It can be shown (see for instance Young, 1971 or Golub & van Loan, 1996) that

$$\lim_{m \rightarrow \infty} R^m = 0 \text{ if and only if } \rho(R) < 1 , \quad (5.34)$$

where $\rho(R)$ is the spectral radius of the matrix R defined as

$$\rho(R) = \max |\lambda(R)| , \quad (5.35)$$

where $\lambda(R)$ are eigenvalues of the matrix R .

The spectral radius $\rho(R)$ is also called the asymptotic convergence rate and it represents the worst factor by which the error is reduced with one iteration step.

The convergence rate also depends on the form of the initial algebraic error. It can be written as a combination of the eigenvectors \mathbf{w}_k of the iteration matrix R

$$\mathbf{e}^{(0)} = \sum_k c_k \mathbf{w}_k , \quad (5.36)$$

where $c_k \in R$ are coefficients at the eigenvectors. After m iteration steps the error has a form

$$\mathbf{e}^{(m)} = R^m \mathbf{e}^{(0)} = \sum_k c_k R^m \mathbf{w}_k = \sum_k c_k \lambda_k^m(R) \mathbf{w}_k . \quad (5.37)$$

In other words, after m iterations, the k th eigenvector in the $e^{(0)}$ expansion has been reduced by a factor of $\lambda_k^m(R)$.

If we take the weighted Jacobi method in 1D as an example, the eigenvalues of the iteration matrix $R_{J\omega}$ are

$$\lambda_k(R_{J\omega}) = 1 - \omega \sin^2 \left(\frac{k\pi}{2N} \right) , \quad (5.38)$$

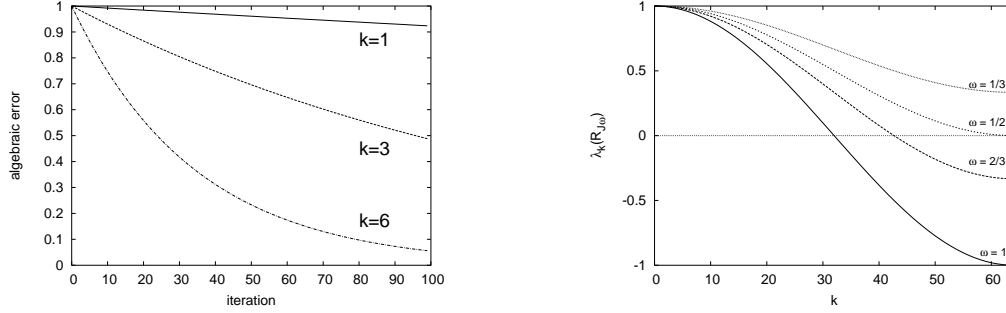


Figure 5.2: Convergence properties of the 1D weighted Jacobi method. Left: Relaxation of three smooth modes ($k = 1, 3, 6$). Right: Eigenvalues of the weighted Jacobi method. The eigenvalues are always close to 1 for $k \rightarrow 0$ – the convergence of low-frequency modes is poor; high-frequency modes ($k > 32$) can be eliminated in the most efficient way if $\omega = 2/3$.

and the corresponding eigenvectors are

$$w_{k,j} = \sin\left(\frac{jk\pi}{N}\right), \quad (5.39)$$

where j denotes the j th components of the eigenvector \mathbf{w}_k . We can see that the eigenvectors are simply the Fourier modes. The eigenvalues, which describe the convergence rate of that modes, show that the convergence rate of the smooth modes (with a small k) is close to 1 regardless of the parameter ω , which means that the convergence of the smooth modes is always very slow (see Fig. 5.2.3). Unfortunately, this feature is common for all standard relaxation methods. It can be intuitively understood taking in consideration the fact that the information about the value at some point can influence only the values in the neighbour points during one relaxation step (due to 7-point discretization). Assuming this information must travel the whole wavelength of the mode of the error to eliminate it, it is clear that it takes many iteration steps to eliminate the smooth (long wavelength) modes. Moreover, if we increase the resolution to reach a higher precision, the smooth modes become effectively longer (measured in the grid zones) and this unwanted feature becomes worse. Elimination of this behaviour was a great success of the multigrid methods.

5.2.4 The DADI method

As an example of more advanced relaxation methods we describe the Dynamic Alternating Direction Implicit (DADI) method in this section. This

method is implemented in the ZEUS2D code. We have ported it to ZEUS3D and used it for experiments in Cartesian coordinates, where it worked satisfactorily. However, the convergence in spherical coordinates was very slow, so finally, we have switched to the multigrid method.

The DADI method is an extension of the ADI (Alternating Direction Implicit) method, which is based on the idea of *line relaxation*. The matrix of the linear system 5.9 can be split as follows

$$A = T - U - L , \quad (5.40)$$

where T denotes the tridiagonal matrix, U and L are remaining upper and lower parts. The tridiagonal matrix (like the diagonal one) is very easy to invert, for instance by the Gaussian elimination (it needs only N arithmetic steps, where N is a size of the matrix). Otherwise, the method is similar to the Jacobi method, the new approximation is obtained from the current one using the formula

$$\mathbf{v}^{(1)} = R\mathbf{v}^{(0)} + T^{-1}\mathbf{f} , \quad (5.41)$$

where R is the iteration matrix defined as

$$R = T^{-1}(L + U) . \quad (5.42)$$

Using the direct solution of the tridiagonal system the ADI method is able to update the entire line of the 3D grid at once. These lines, parallel to the particular coordinate axis, are represented by the smaller blocks of the matrix A along the main diagonal (see Fig. 5.1). The direction of the lines is given by the order of the linear equations. In order not to make a certain coordinate favoured, the ADI method cyclically alternates the order of the linear equations. Thus, new approximation is computed using the procedure

$$\begin{aligned} \mathbf{v}^{(a)} &= R_1\mathbf{v}^{(0)} + T_1^{-1}\mathbf{f} \\ \mathbf{v}^{(b)} &= R_2\mathbf{v}^{(a)} + T_2^{-1}\mathbf{f} \\ \mathbf{v}^{(1)} &= R_3\mathbf{v}^{(b)} + T_3^{-1}\mathbf{f} , \end{aligned} \quad (5.43)$$

where R_{1-3} and T_{1-3} are iteration and tridiagonal matrices which arise from the orderings starting along the x_1 , x_2 and x_3 coordinate axes.

The DADI method introduces the idea of weighting into the ADI method. It searches for a steady state solution of the diffusion equation

$$\frac{\partial \mathbf{u}}{\partial g} = \nabla^2 \mathbf{u} - \mathbf{f} , \quad (5.44)$$

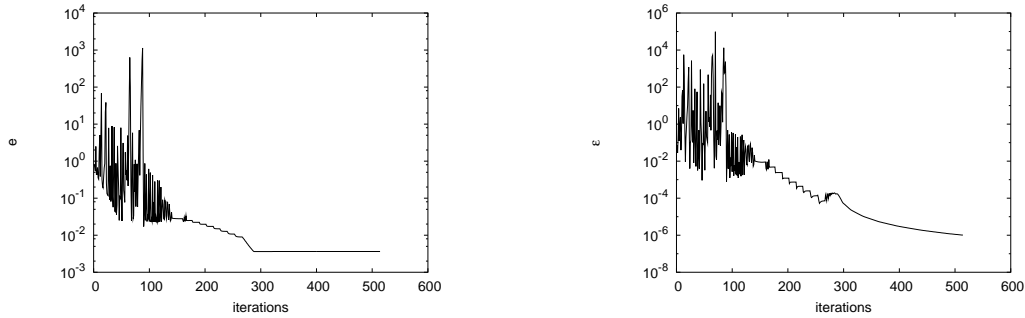


Figure 5.3: Computation of the gravitational potential of the homogeneous sphere using the DADI method on the Cartesian grid $50 \times 50 \times 50$. The left panel shows the algebraic error (obtained by comparison to the analytical potential), the right panel shows the relative error of the Poisson equation. The discretization error was reached after 300 iterations.

where g is a virtual iteration time with no relation to the dynamical time of the simulation. Large virtual time-steps are equivalent to the large weight parameter ω , i.e. the large component of relaxed solution in the new approximation.

The advantage of this approach is that it is possible to maintain the virtual time-step near the stability margin and do as much super-relaxation as possible not to break the convergence. Standard techniques for controlling the time-step of the numerical solution of differential equations can be used for this purpose.

The change-deck for ZEUS3D v3.4.2 which includes the DADI Poisson solver into the code is available at <http://richard.wunsch.matfyz.cz/zeus/-chgz.gravity-dadi>.

5.3 The multigrid method

5.3.1 Basic ideas

In Section 5.2.3 we have seen that the convergence of the smooth modes is very slow when standard relaxation methods are used. The quest to find relaxation methods which eliminate the smooth error modes quickly leads to the development of the multigrid methods. They are based on two ideas: the idea of *nested iterations* and the *correction scheme*.

Nested iterations:

As the wavelength of the error modes is measured in the grid zones from

the point of view of the method, it can be effectively decreased using a coarser grid. In other words, the smooth modes look less smooth when set on the coarser grid. It is a good idea, therefore, to start the computation by relaxation on a coarser grid and then use the result as an initial condition for the final refinement on a high-precision grid. If we ask how to solve the problem on the coarser grid in the most efficient way, we find out that it is a transition to the even coarser grid. If we extend the procedure recursively we get the idea of nested iterations:

- Relax on $A\mathbf{u} = \mathbf{f}$ on a very coarse grid to obtain an initial guess for the next finer grid
-
-
- Relax on $A\mathbf{u} = \mathbf{f}$ on Ω^{2h} to obtain an initial guess for Ω^h
- Relax on $A\mathbf{u} = \mathbf{f}$ on Ω^h to obtain a final approximation to the solution

where $\Omega^h, \Omega^{2h}, \dots$ are the grids with the zone sizes $h, 2h, \dots$. Note that the relaxations on the coarser grids need substantially less arithmetic operations, in particular for higher dimensional (2D or 3D) problems.

The previous procedure does not solve the problem what happens if it reaches the finest grid and there is still a smooth component of the error. Also, it is not clear how to go back to the coarser grid and do not drop the details of the solution obtained by the relaxation on the fine grid. The correction scheme gives the answer.

The correction scheme:

It is based on the solution of the residual Eq. 5.12, which enables us to obtain an approximation to the algebraic error \mathbf{e} from the residual \mathbf{r} . In the next step it can be used to correct the approximation to the solution \mathbf{v} . The two-grid correction scheme can be written in a form

- Relax on $A\mathbf{u} = \mathbf{f}$ on Ω^{2h} to obtain an approximation \mathbf{v}^h and compute the residual $\mathbf{r} = \mathbf{f} - A\mathbf{v}^h$
- Relax on the residual equation $A\mathbf{e} = \mathbf{r}$ on Ω^{2h} to obtain an approximation to the error \mathbf{e}^{2h}
- Correct the approximation \mathbf{v}^h with the error \mathbf{e}^{2h} : $\mathbf{v}^h \leftarrow \mathbf{v}^h + \mathbf{e}^{2h}$.

The next step is to define more precisely the way how to transfer the problem between the grids.

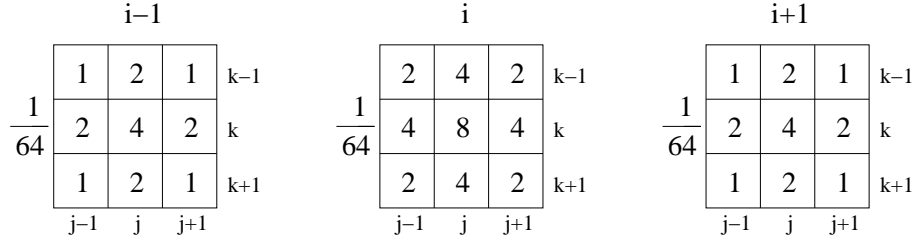


Figure 5.4: Stencils show the weights of the finer-grid points which contribute to the $i/2, j/2, k/2$ point of the coarser grid when the restriction is applied. The interpolation operator can be obtained as a transposition of the appropriate restriction operator matrix.

The extension of the previous grid-transfer operators to a higher dimension is straightforward. For the sake of transparency it is useful to represent the restriction operator in the form of stencils. They show the weight coefficients of the neighbour points on the fine grid. The stencil form of the 3D full weighting restriction operator is suggested by Fig. 5.4.

Finally, we give the more precise definition of the coarse grid operator A^{2h} , which we need to solve the residual equation on the coarse grid. Using the interpolation operator the residual equation on the fine grid can be written in a form

$$A^h \mathbf{e}^h = A^h I_{2h}^h \mathbf{u}^{2h} = \mathbf{r}^h \quad (5.50)$$

and by applying the restriction operator I_h^{2h} to both sides of the Eq. 5.50 we get

$$\underbrace{I_h^{2h} A^h I_{2h}^h}_{A^{2h}} \mathbf{u}^{2h} = I_h^{2h} \mathbf{r}^h \quad (5.51)$$

A definition of the coarse-grid operator

$$A^{2h} = I_h^{2h} A^h I_{2h}^h \quad (5.52)$$

is also called the *Galerkin condition*.

5.3.3 Multigrid schemes

Gathering the ideas and techniques from the previous two sections we are able to introduce the basic multigrid schemes. The recursive usage of the correction scheme leads us to a definition of the simplest multigrid scheme – the V-cycle. It can be written in a recursive form as

$$\mathbf{v}^h \leftarrow V^h(\mathbf{v}^h, \mathbf{f}^h, \nu_1, \nu_2)$$

1. Relax ν_1 times on $A^h \mathbf{u}^h = \mathbf{f}^h$ with the initial guess \mathbf{v}^h
2. If $\Omega^h =$ coarsest grid, go to step 4
Else

$$\begin{aligned} \mathbf{f}^{2h} &\leftarrow I_h^{2h}(\mathbf{f}^h - A^h \mathbf{v}^h) \\ \mathbf{v}^{2h} &\leftarrow 0 \\ \mathbf{v}^{2h} &\leftarrow V^{2h}(\mathbf{v}^{2h}, \mathbf{f}^{2h}, \nu_1, \nu_2) \end{aligned}$$

3. Correct $\mathbf{v}^h \leftarrow \mathbf{v}^h + I_{2h}^h \mathbf{v}^{2h}$
4. Relax ν_2 times on $A^h \mathbf{u}^h = \mathbf{f}^h$ with the initial guess \mathbf{v}^h

In the first phase it descends down to the coarsest grid doing ν_1 relaxation steps on each level. The system is solved exactly on the coarsest grid and then the algorithm ascends to the finest grid with ν_2 relaxations on each level. In the relaxations during the first (descending) phase the high-frequency error modes are eliminated, which is necessary for the interpolation used in the second phase (very roughly: the interpolation of the error from the coarser grid $2h$ gives the poor representation of the real error on the grid h if the error has a high oscillatory component; see e.g. Briggs et al., 2000 for the proper discussion of this problem).

The V-cycle can be simply generalised into the whole family of the multi-grid methods called the μ -cycle. It has a recursive form

$$\mathbf{v}^h \leftarrow M\mu^h(\mathbf{v}^h, \mathbf{f}^h, \mu, \nu_1, \nu_2)$$

1. Relax ν_1 times on $A^h \mathbf{u}^h = \mathbf{f}^h$ with the initial guess \mathbf{v}^h
2. If $\Omega^h =$ coarsest grid, go to step 4
Else

$$\begin{aligned} \mathbf{f}^{2h} &\leftarrow I_h^{2h}(\mathbf{f}^h - A^h \mathbf{v}^h) \\ \mathbf{v}^{2h} &\leftarrow 0 \\ \mathbf{v}^{2h} &\leftarrow M\mu^{2h}(\mathbf{v}^{2h}, \mathbf{f}^{2h}, \mu, \nu_1, \nu_2) \mu \text{ times} \end{aligned}$$

3. Correct $\mathbf{v}^h \leftarrow \mathbf{v}^h + I_{2h}^h \mathbf{v}^{2h}$
4. Relax ν_2 times on $A^h \mathbf{u}^h = \mathbf{f}^h$ with the initial guess \mathbf{v}^h

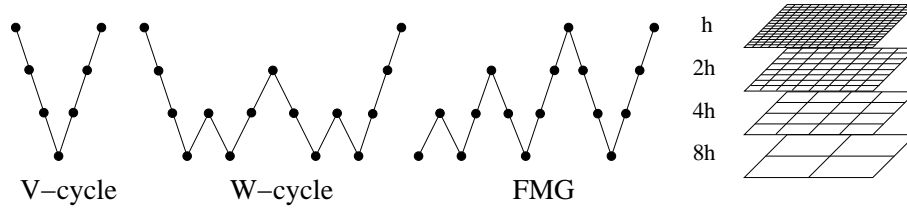


Figure 5.5: Basic multigrid schemes on four grid-levels.

The most often used values are $\mu = 1$ (the V-cycle) and $\mu = 2$, which is called the W-cycle.

Using the idea of nested iteration the V-cycle can be extended into the *full multigrid method* (FMG), the most powerful method we describe. A set of ν_0 V-cycles on a certain grid-level is preceded by a set of ν_0 coarse-grid V-cycles in order to give the best initial guess possible. The recursive form of the FMG is

$$\mathbf{v}^h \leftarrow FMG^h(\mathbf{v}^h, \mathbf{f}^h, \nu_0, \nu_1, \nu_2)$$

1. If $\Omega^h =$ coarsest grid, set $\mathbf{v}^h \leftarrow \mathbf{0}$ and go to step 3
Else

$$\mathbf{f}^{2h} \leftarrow I_h^{2h}(\mathbf{f}^h)$$

$$\mathbf{v}^{2h} \leftarrow FMG^{2h}(\mathbf{v}^{2h}, \mathbf{f}^{2h}, \nu_0, \nu_1, \nu_2)$$

2. Correct $\mathbf{v}^h \leftarrow I_{2h}^h \mathbf{v}^{2h}$
3. $\mathbf{v}^h \leftarrow V^h(\mathbf{v}^h, \mathbf{f}^h, \nu_1, \nu_2)$

The described multigrid schemes are suggested by Fig. 5.5.

5.3.4 Implementation of the multigrid method

We have created the code Šemík – the Poisson solver which uses the multigrid method. The source code is available at <http://richard.wunsch.matfyz.cz/~semik/>. It is written in the C programming language and can be used in ZEUS (the FORTRAN interface in the form of ZEUS change-deck is included) or independently as the library of functions.

The code is still in development, so only some of the described multigrid algorithms are implemented so far. It works in Cartesian and spherical coordinates, but the extension to the other orthogonal coordinate systems

should be easy. The weighted Jacobi and weighted Gauss-Seidel methods can be used for the relaxation, the line relaxation is also possible. The only implemented multigrid scheme is the V-cycle.

Fig. 5.6, left panel, shows the asymptotic convergence rate of the multigrid solver using the weighted Jacobi method and the Gauss-Seidel method. We can see that the convergence is substantially faster when Gauss-Seidel relaxation is used reaching the convergence rate ~ 0.13 , while when Jacobi method is used the convergence rate is ~ 0.65 .

The beneficial property of the multigrid codes is the independence of the convergence rate on the wavelength of the error mode. Fig. 5.6, right panel, illustrates that our code shows this property.

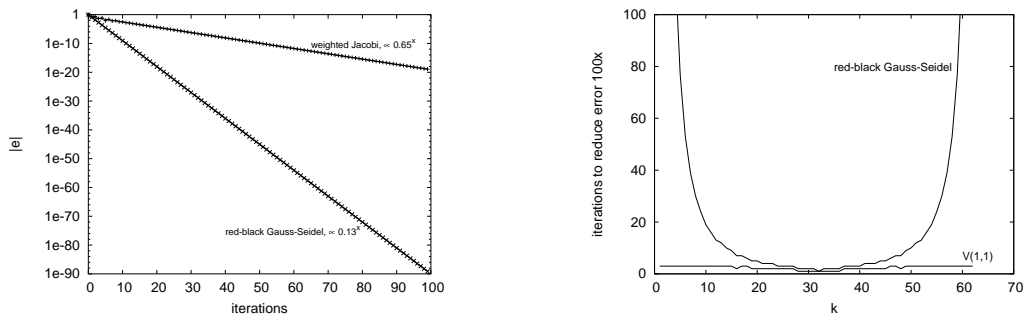


Figure 5.6: Convergence of the V-cycle V(1,1) on Cartesian grid $64 \times 64 \times 64$ when weighted Jacobi ($\omega = 2/3$) and Gauss-Seidel relaxation is used. Right: Number of iterations necessary to reduce the error 100x depending on the wavenumber k of the error. The same V-cycle with the Gauss-Seidel relaxation on the same grid is compared to the standard red-black Gauss-Seidel relaxation method. While convergence of the V-cycle almost does not depend on k (it needs 3 – 6 iterations), the red-black Gauss-Seidel needs more than 1000 iterations to reduce the mode $k = 1$ by factor 100.

Chapter 6

Hydrodynamic model of the shell

In the first section of this chapter we describe the module SHELL which sets up the problem of the expanding shell in the ZEUS code. The source code of the module SHELL is available at <http://richard.wunsch.matfyz.cz/zeus/chgz.shell>.

Every numerical model should be carefully tested against analytical or other numerical models. ZEUS itself was tested by the authors of the code (Stone et al, 1992). In sections 6.2 – 6.4 we present tests of the SHELL module and the tests of our extensions described in chapter 4. Section 6.5 shows the tests of the interconnection of the SHELL module with the Poisson solver.

6.1 The SHELL module

The simulation can be set up either in Cartesian coordinates (the computational domain is a cube with the shell expanding from its centre) or in spherical coordinates (the computational domain is a sphere sector). We fill the whole computational domain with gas of particle density n_0 , average molecular weight μ and temperature T_0 . Spherical expanding shock is created by inserting the energy into this homogeneous medium. A certain amount of energy E_{init} can be inserted initially, energy can be also fed continuously with rate E_{flow} . In order to prevent the model from large skips in hydrodynamic quantities, which can cause numerical difficulties, the energy is inserted into the area of radius R_{initb} (or R_{flowb}) with the radial distribution $\sim \exp(r/R_{\text{init}})$ (or $\exp(r/R_{\text{flow}})$) (see Fig. 6.1). Variables R_{init} , R_{initb} , R_{flow} and R_{flowb} can be set in parsecs, centimetres or grid zones depending on the

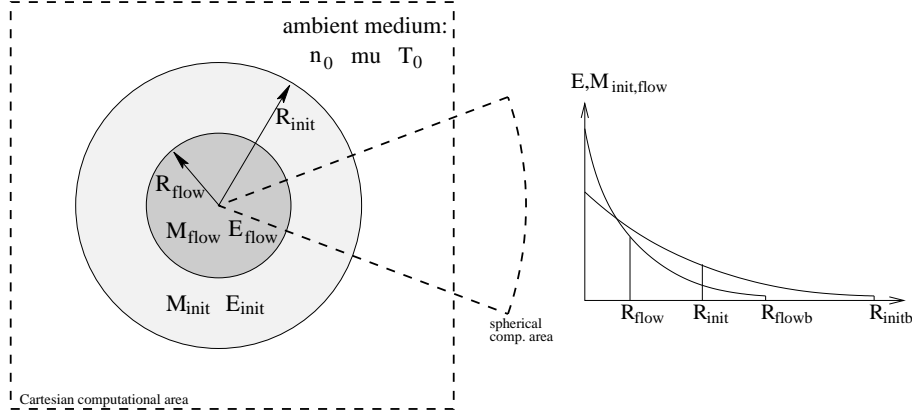


Figure 6.1: Energy source scheme.

value of parameter r_{unit} .

Since our model does not include microscopic processes as evaporation (and the evaporation of the shell into its interior is the main source of the mass there), we need to insert the mass artificially. It can be controlled using variables M_{init} and M_{flow} . Similarly, as in the case of energy, the radial distribution of the mass is controlled by R_{init} , R_{initb} , R_{flow} and R_{flowb} parameters.

If the mass is inserted into the central zones, the kinetic energy in these zones is changed. In order to conserve the energy rate given by parameter E_{flow} , the internal energy in these zones is corrected appropriately. Additionally, the ratio of the kinetic and internal energy, which changes artificially, can be influenced by the change of the velocity in these zones. This feature is controlled by the parameter $velsol$: if $velsol = 0$, the velocity is changed

Table 6.1: Parameters of the shell setup.

param.	unit	param.	unit
n_0	cm^{-3}	r_{unit}	–
μ	amu	$velsol$	–
T_0	K	$vwind$	km/s
R_{init}	pc,cm,zones	R_{flow}	pc,cm,zones
R_{initb}	pc,cm,zones	R_{flowb}	pc,cm,zones
E_{init}	10^{51} erg	E_{flow}	10^{51} erg/Myr
M_{init}	M_{\odot}	M_{flow}	M_{\odot}/Myr

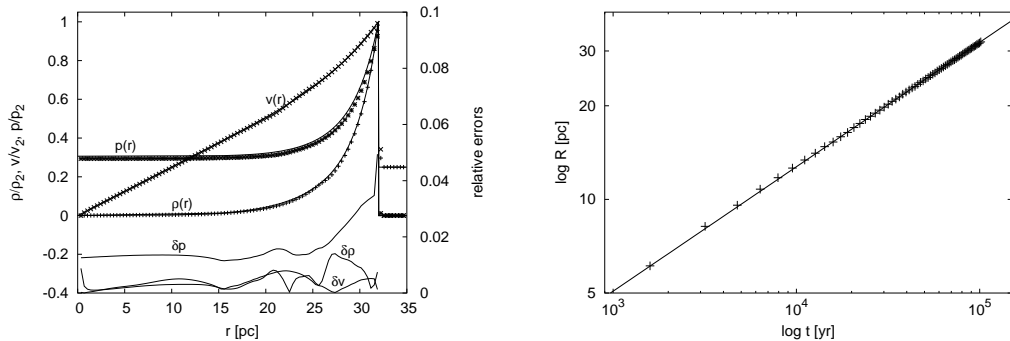


Figure 6.2: Simulation of the Sedov problem on the 400x1x1 grid. Left: radial profiles of the density, velocity and pressure and the relative errors. For the sake of clarity only every fourth point is plotted. Absolute values at the position of shock front are: $\rho_2 = 5.2 \text{ m}_\text{H}/\text{cm}^3$, $v_2 = 94 \text{ km/s}$, $p_2 = 2.53 \cdot 10^{-10} \text{ dyne/cm}^2$. Right: time dependence of the shock-front position in ZEUS simulation (+ symbols) vs. the analytical Sedov solution (line).

in order to conserve the momentum in the zone; if $velsol=1$, the radial component of the velocity is changed to conserve the kinetic energy in the zone, other components are leaved untouched; $velsol=2$ means that all components of the velocity are decreased by factor $1 - \exp(r/R_{\text{flow}})$ in the $(0, R_{\text{flowb}})$ area; and in the case $velsol=3$, the radial component of the velocity is set to the value $vwind$, while other components are set to zero. In the later computations we use $velsol = 0$, because with this value we get the fastest relaxation to the correct solution (tested with 1D Sedov and Weaver solutions).

A detailed description of the SHELL module is included in its source code.

6.2 Expansion of 1D adiabatic bubble

6.2.1 The Sedov problem

The Sedov problem can be used as the simplest test of the SHELL module. We set up 1D spherically symmetric simulation with the abrupt energy input ($E_{\text{init}} = 10^{51} \text{ erg}$) into the homogeneous medium with $n_0 = 1 \text{ cm}^{-3}$, $\mu = 1.3 \text{ amu}$ and $T_0 = 7000 \text{ K}$ (values typical for a single supernovae explosion in a common galactic ISM). The radial profiles of density, velocity and pressure at the time $t = 10^5 \text{ yr}$ are compared to the analytical Sedov solution given by the Eq. 2.9 (see Fig. 6.2, left panel). All quantities are in a good agreement with the analytical solution – relative errors of density and velocity are smaller

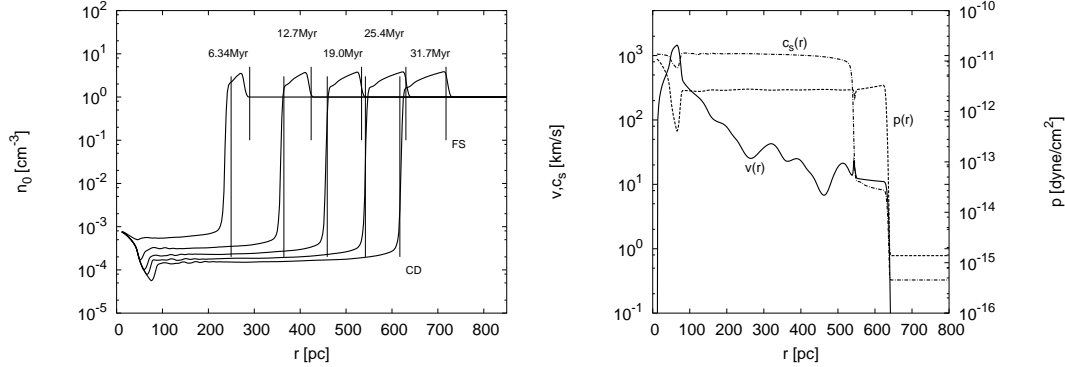


Figure 6.3: The expanding super-shell, simulation on the 400x1x1 grid. Left: radial profiles of density, vertical lines denote the positions of the shock-front (SF) and the contact discontinuity (CD) given by the analytical Weaver’s solution. Right: radial profiles of velocity, pressure and sound-speed. The velocity curve shows the artificial sound-waves which propagate in the shell interior.

than 2%, the relative error of pressure is a bit higher, it reaches 5% near the shock. However, this relatively high discrepancy may be caused by a small horizontal shift of the steep curve – the error in the shock-front position.

The right panel of Fig. 6.2 shows the time dependence of the position of the shock-front. The evolution of the shock follows almost perfectly the power-law $\sim t^{2/5}$, the relative error of the shock-front position is below 1%.

6.2.2 Expanding adiabatic super-shell

In order to test the behaviour of the model when the continuous energy (and mass) input is used, we set up the simulation of the expanding super-shell. The energy is inserted continuously at a rate $E_{\text{flow}} = 6.667 \cdot 10^{51} \text{erg/Myr}$ in the same ISM (in reality it can be e.g. the super-shell created by a powerful OB association). The mass is inserted at a rate $M_{\text{flow}} = 200 M_{\odot}/\text{Myr}$.

Fig. 6.3, left panel, shows the radial profiles of the density at several stages of the shell evolution. The positions of the shock front and contact discontinuity are compared to the values given by the Weaver’s semi-analytical solution (Eqs. 2.14 and 2.18). They are in good agreement, in particular in the later phase, when the discrepancy is smaller than the three grid-zones size, which is the scale of the artificial viscosity.

Occasionally, numerical instabilities may lead to artificial sound-waves propagating in the shell interior (this effect is mentioned in Stone & Norman, 1992; they usually occur in stagnant flows of mass). Here, it is illustrated in velocity profile in Fig. 6.3, right panel. They can be damped by imposing

grid	$R_{\text{initb}} \setminus C_2$	1	3	5	7
200	4%	23.7%	11.5%	21.4%	29.2%
200	8%	24.6%	3.2%	8.7%	13.2%
400	4%	28.8%	3.6%	8.0%	12.2%
400	8%	27.1%	6.9%	2.5%	4.9%
800	4%	31.2%	8.9%	2.1%	4.4%
800	8%	28.3%	9.9%	4.0%	1.1%

Table 6.2: The maximum relative error of energy conservation in simulations with abrupt energy input ($n_0 = 1 \text{ cm}^{-2}$, $\mu = 1.3 \text{ amu}$, $T_0 = 10 \text{ K}$, $E_{\text{init}} = 10^{51} \text{ erg}$) depending on resolution, size of the central area R_{initb} and artificial viscosity given by parameter C_2 . Temperature of the ambient medium is unrealistically small to make its internal energy unimportant.

grid	$R_{\text{flowb}} \setminus C_2$	1	3	5	7
200	5%	2.7%	4.3%	6.1%	7.2%
200	10%	4.6%	0.8%	0.1%	1.3%
400	5%	3.0%	3.5%	4.9%	5.6%
400	10%	4.6%	1.3%	0.3%	0.2%
800	5%	3.1%	3.3%	4.4%	5.0%
800	10%	4.3%	1.4%	0.6%	0.2%

Table 6.3: The maximum relative error of energy conservation in simulations with continuous energy input ($n_0 = 1 \text{ cm}^{-2}$, $\mu = 1.3 \text{ amu}$, $T_0 = 10 \text{ K}$, $E_{\text{init}} = 6.667 \cdot 10^{51} \text{ erg/Myr}$).

the linear artificial viscosity (Eq. 4.20, $C_1 = 0.5$ is usually a suitable value).

6.3 Energy conservation

In our first simulations we had had serious problems with the conservation of energy. It had seemed that the ZEUS algorithm did not conserve energy well if the hydrodynamic variables include large gradients. These problems were later solved by making the total energy advection scheme work. Nevertheless, we present our experiments related to the energy conservation in the belief that they may be useful. In the second part of this section we measure the internal and kinetic energy in the shell and the shell interior and compare them to the analytical model.

It should be also remarked that the problem is very insensitive to the

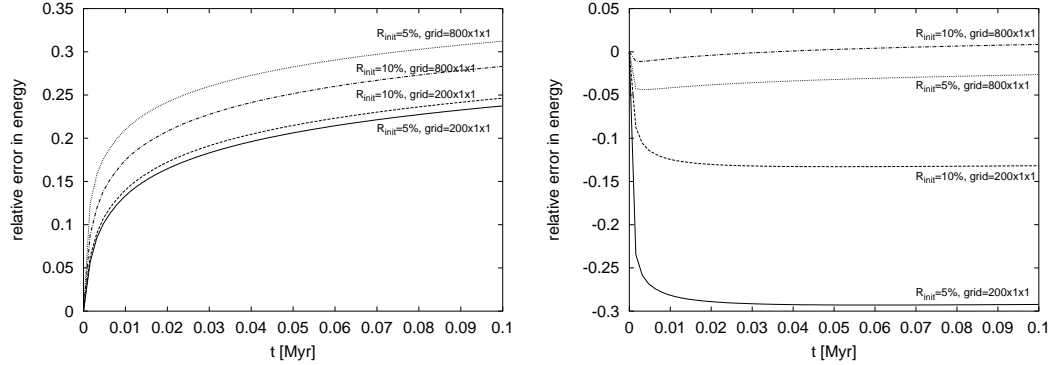


Figure 6.4: Evolution of the relative error in the energy conservation in the case of the abrupt energy input. Left: low artificial viscosity ($C_2 = 1$) – the error is positive; Right: high artificial viscosity ($C_2 = 7$) – the error is negative and can be damped using the higher resolution or larger central area.

error in energy. The quantities that describe the shell evolution (shell radius, expansion energy and surface density) are only 1/5th power of the energy. The internal energy (and also the pressure) in the shell is determined in particular by the radiative cooling, so it should not be affected by small discrepancies in energy conservation.

We have observed that the critical parameters for the energy conservation are the artificial viscosity strength, the grid resolution and the size of the area where the energy is inserted (controlled by R_{initb} and R_{flowb} parameters). Maximum relative errors of the energy conservation depend on these parameters, they are shown in Tab. 6.2 (for abrupt energy input) and Tab. 6.3 (for continuous energy input).

A detailed analysis of the time evolution of error shows that if the artificial viscosity is too small ($C_2 < 3$), the error is positive (the computation contains more energy than it should) and it is difficult to make it smaller by varying other parameters (it even grows with increasing resolution, see Fig. 6.4, left panel). On the other hand, when the artificial viscosity is high enough, the error in energy is negative and can be damped by better resolution and/or larger central area, where the energy is inserted (see Fig. 6.4, right panel). In the case of the continuous energy input, the evolution of the error is similar (see Fig. 6.5).

A general method for making the error in energy conservation low is employing a sufficiently high artificial viscosity (such that we do not get a positive error), high resolution and a sufficiently large energy source area.

The same experiments can be performed with total energy advection. The scheme itself ensures the energy conservation to the machine precision, but a

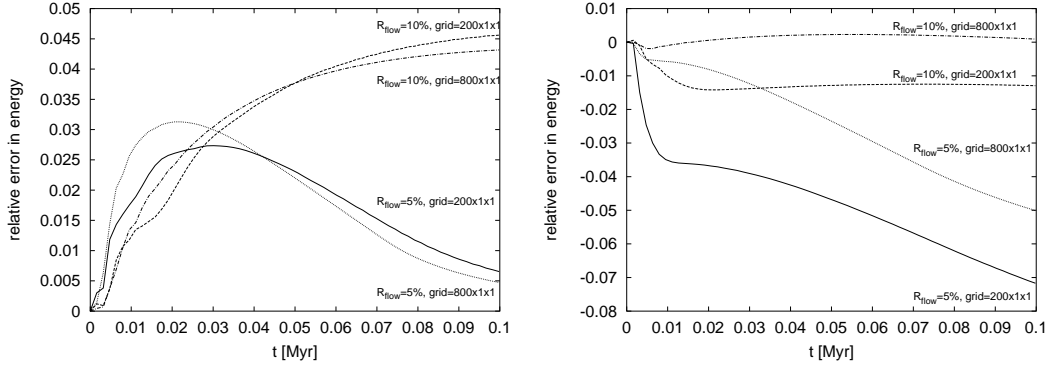


Figure 6.5: Evolution of the relative error in energy conservation in the case of continuous energy input.

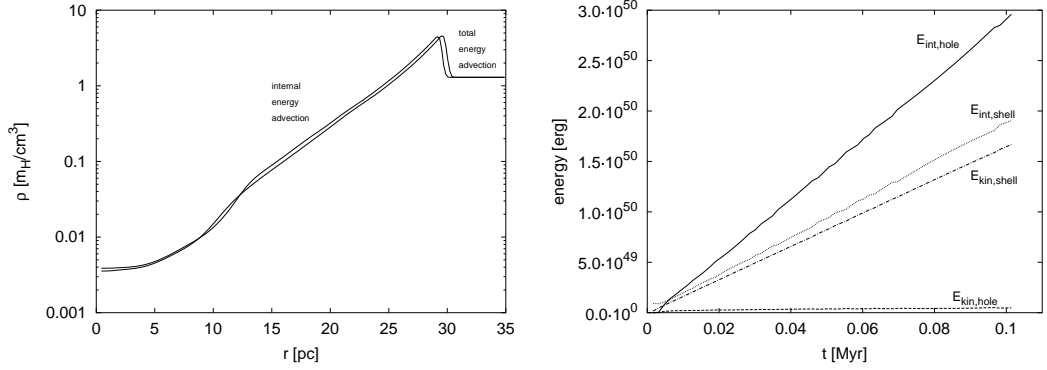


Figure 6.6: Left: simulation of the Sedov problem with the internal and total energy advection scheme. Right: internal and kinetic energy in the shell and its interior in the adiabatic expanding shell with the continuous energy input.

small error is generated when the negative values of the internal energy are eliminated by adding some energy into the affected zones (see section 4.11). Nevertheless, the error was in all cases negligibly small ($< 10^{-6}$).

Fig. 6.6, left panel, illustrates the weak dependence of the shell dynamics on the energy. It compares simulation of the Sedov problem with the internal energy advection to the one with the total energy advection. Although the discrepancy in the total energy is almost 8%, the density profile of the simulation with more energy is shifted only by 1.5%. Otherwise, the density profiles (and other quantities too) are in a good agreement.

Weaver's solution predicts the relative amounts of internal and kinetic energy in the shell and its interior (see section 2.2). It can be used to check the energy distribution in the numerical model of the expanding shell. Fig. 6.6, right panel, shows that these amounts of energy remain constant during the

	hole			shell		
	E_{int}	E_{kin}	E_{tot}	E_{int}	E_{kin}	E_{tot}
Weaver	45.5%	0.0%	45.5%	32.5%	22.0%	54.5%
ZEUS	45.4%	1.0%	46.4%	28.3%	25.3%	53.6%

Table 6.4: Ratios of energy in the ZEUS model of the expanding adiabatic shell with the continuous energy input comparing to the Weaver’s semi-analytical solution.

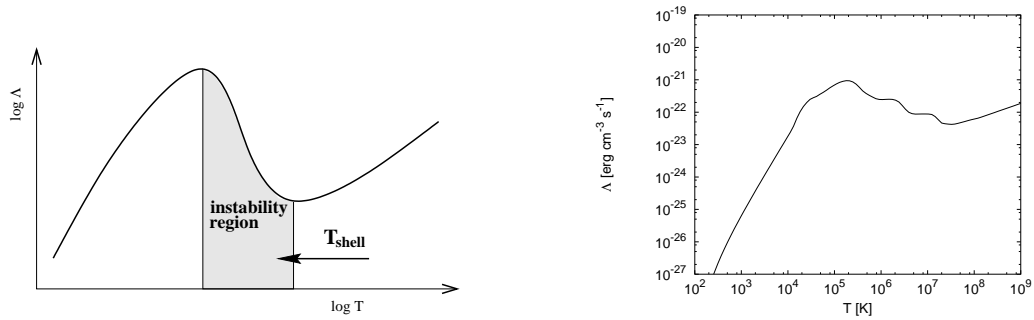


Figure 6.7: Left: Mechanism of the thermal instability. Right: cooling function by MacDonald & Bailey, 1989.

whole shell evolution, which is consistent with the self-similar Weaver’s solution. Tab. 6.4 compares the energy ratios in our simulations to the Weaver’s solution. We can see that they are in a good agreement, the most serious discrepancy has the ratio $E_{\text{int}}/E_{\text{kin}}$ inside the shell, which is smaller by several percent.

6.4 The thermal instability

The thermal instability in the expanding shell can be used as the test of our implementation of the radiative cooling. The mechanism of the thermal instability is explained in Fig. 6.7, left panel. As the shell expands, it cools down and increases its density. When the temperature inside the shell enters the instability region of the cooling function (where $d\Lambda/dT < 0$), the efficiency of the cooling grows with the decreasing temperature and this positive feedback leads to the quick collapse of the shell into the thin layer. This process was described by Falle (1981) as the ”catastrophic cooling” for the case of supernovae remnants.

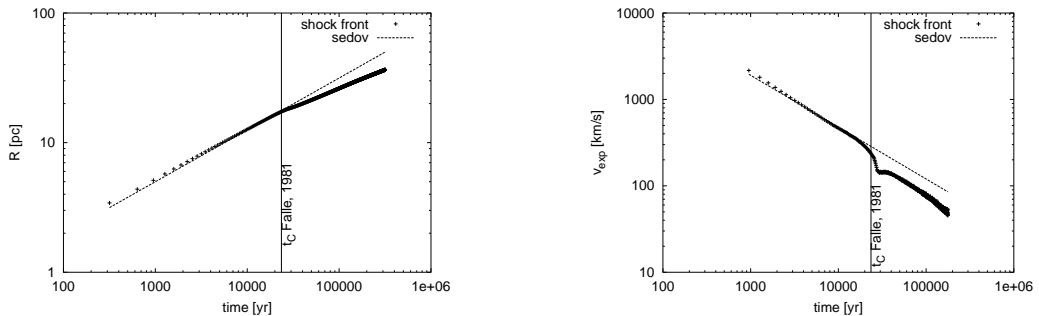


Figure 6.8: Left: the shock-front position in the simulation of the collapse of the SNR. The line denotes the Sedov solution. Right: expansion velocity of the shock in the same simulation.

In order to compare our simulations with computations of S. A. E. G. Falle we have to use the same cooling function. Falle has used the cooling function made by Kafatos, 1973. This cooling function is similar to the one by MacDonald and Bailey (1989), which is the part of the standard ZEUS distribution (in fact the MacDonald & Bailey cooling function is based on the Kafatos cooling function). So we use the original ZEUS cooling function (see Fig. 6.7, right panel) with the new Brendt algorithm.

We setup the simulation with abrupt energy input $E_{\text{init}} = 10^{51}$ erg into the homogeneous medium of particle density $n_0 = 1 \text{ cm}^{-3}$. After a certain period the Sedov solution is established, and it remains until the cooling starts to be important. Falle predicts that it happens at time

$$t_c = 2.7 \times 10^4 \left(\frac{E_{\text{init}}}{10^{51} \text{ erg}} \right)^{0.24} n_0^{-0.52} \text{ yr} , \quad (6.1)$$

when the shell quickly collapses. The expansion velocity of the shock drops down as the matter flows back toward the contact discontinuity. Later, when the pressure inside the shell reestablishes equilibrium with its surroundings, the expansion velocity grows again, but the expansion does not follow the Sedov solution $v_{\text{exp}} \sim t^{-3/5}$ anymore. The collapse of the shell may be so rapid that additional shocks are created.

Fig. 6.8 shows our simulation of this process. The evolution of the shell leaves the Sedov solution at the correct time, at the right panel we can see the drop in the expansion velocity. The Fig. 6.8 is very similar to Fig. 2 and 3 in Falle (1981), although we were not able to model the additional shocks in the collapsing shell as Falle with his special purpose Lagrangian hydrocode.

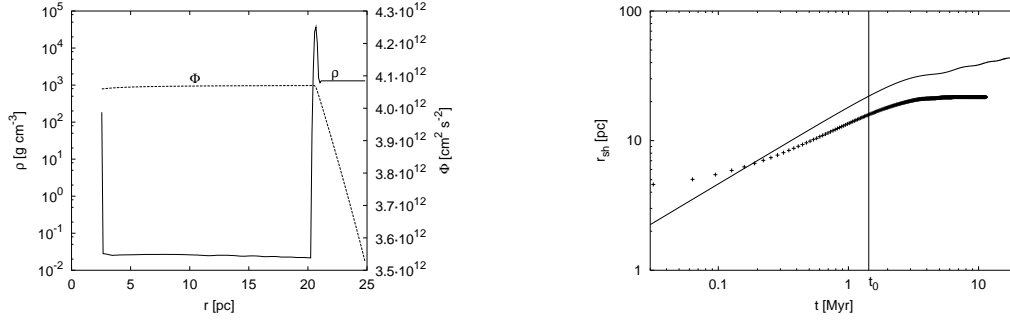


Figure 6.9: The 1D self-gravitating expanding shell. Parameter of the simulation are: $n_0 = 10^3$, $\mu = 1.3$, $L = 5 \times 10^{51} \text{erg/Myr}$, the radiative cooling is on. Left: radial profiles of the density and the gravitational potential. Right: position of the shock-front depending on time comparing to the analytical solution Whitworth & Francis, 2002; Eq. 2.41.

6.5 1D self-gravitating expanding shell

The last feature of the code which remains to be tested is the self-gravity. The tests of the Poisson solver itself are presented in section 5.3.4, here we test only the connection of the Poisson solver with the ZEUS code and the SHELL module. For this purpose we setup the 1D simulation of the shell with the self-gravity switched on and compare the result to the analytical solution given by Whitworth & Francis, 2002 (see section 2.4).

The inclusion of the self-gravity brings the problem of the ambient matter falling to the centre of the computational domain. It can be shown that it is almost impossible to find the parameters of the problem (ambient medium density and temperature, energy rate) for which the shell could become gravitationally unstable and the ambient matter would be stable according to Jeans law. In reality the ambient medium does not collapse, because it contains the magnetic field and turbulence. To solve this problem we use a simple work-around. In each time-step we detect the shock-front and set the velocity of the ambient medium (exterior to the shock-front) to zero. We should remark here that this artificial intervention does not bring the inconsistency into our model – the aim of this work is to test the analytical models of the gravitational instabilities of expanding shells, we are not interested in the evolution of the ambient medium, which plays the role of the boundary condition in our experiments. The analytical models of the gravitational instabilities which we test assume the homogeneous ambient medium and this work-around only assures this boundary condition.

In this situation we cannot expect the perfect agreement, because the

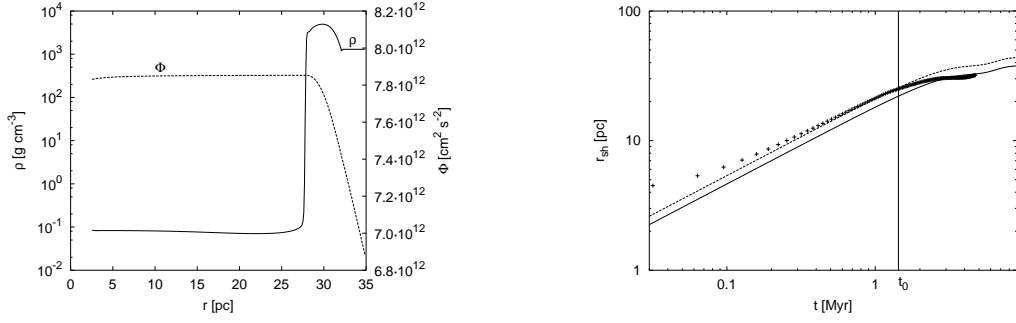


Figure 6.10: The 1D self-gravitating expanding shell. Parameters of the simulation are the same as in Fig. 6.9, but the radiative cooling is off. Left: radial profiles of the density and the gravitational potential. Right: the position of the shock-front depending on time. The solid line is the analytical solution Whitworth & Francis, 2002, the dashed line is the same multiplied by 1.16 – in the initial period same as the Weaver’s model of the adiabatic shell, Eq. 2.14.

numerical and analytical models are a bit different. If we use the radiative cooling in the numerical model to get the thin shell, the energy loss decelerates the shell expansion, in particular, in the later stage of its evolution. Furthermore, the analytical model does not include the external pressure, which is another mechanism decelerating the shell expansion. We can therefore expect that the expansion of the shell in the numerical model will be slower than in the analytical model. On the other hand, when we switch the radiative cooling off, the shell does not collapse into the thin layer and the thin-shell approximation used by the analytical model will be poor. We may expect that the expansion of the shell in the numerical model will be faster at least for $t < t_0$ – the adiabatic shell expands faster than the thin shell by factor of 1.16 according to the Weaver’s model (see Section 2.3 – Weaver’s model of the thin shell).

Fig. 6.9 shows the simulation of the self-gravitating shell with the cooling. Qualitatively it corresponds to the analytical solution. The transition to the gravitationally decelerated expansion occurs at the correct time t_0 given by Whitworth & Francis (2002), but the expansion is slower as we have expected.

Fig. 6.10 shows the simulation with the cooling switched off. Initially, the expansion follows the Weaver’s adiabatic model (with the thick shell and the expansion faster by factor 1.16), then, at the time t_0 the shell is decelerated by the self-gravity. The expansion for $t > t_0$ is even slower than $r_{sh} \sim t^{1/5}$ given by Whitworth & Francis (2002).

Chapter 7

Self-gravitating shells in 3D

Hydrodynamic computations in 3D are extremely CPU time consuming. In order to get the results in a reasonable time, several tricks have to be used.

At first, we are not interested in the early stage of the shell evolution (shell may become gravitationally unstable only when it accretes enough mass and when it cools down, which may only happen in the later stage of its evolution), so we can start the 3D computation in the time when the shell is evolved with spherically symmetric initial conditions obtained by the 1D simulation. The 3D computation can be started in the time given by the linear analysis of the shell gravitational instability (t_b with some safety factor, because the linear analysis may not be exact, see Eq. 3.26).

We can also utilise the ZEUS ability of working on non-equidistant grids. The shell interior, in whose detailed structure we are not interested, can be computed on a radially coarser grid than the remaining area. We define the coarser grid in the region which is in the shell interior at the beginning of the 3D computation (we do not enlarge this region during the simulation to avoid problems which may arise when redefining the grid during the computation). This trick has a positive side effect: using the larger zone sizes effectively increases the linear artificial viscosity, which helps to damp the unwanted sound-waves which may arise from numerical instabilities (see section 6.2.2).

The ambient medium, which we want to stay homogeneous, is not necessary to compute at all. In each time-step we may detect the shock-front and set the border of the computed area several (5-10) grid zones behind it.

The physical time of the simulation (which is proportional to the CPU time) will be significantly shortened if we restrict our survey to models with dense ambient medium and high energy input rate, in which the instability grows relatively fast.

For all that, the computation on a 150x50x50 grid (which is the lowest reasonable resolution to resolve some fragments) needs approximately 20 days

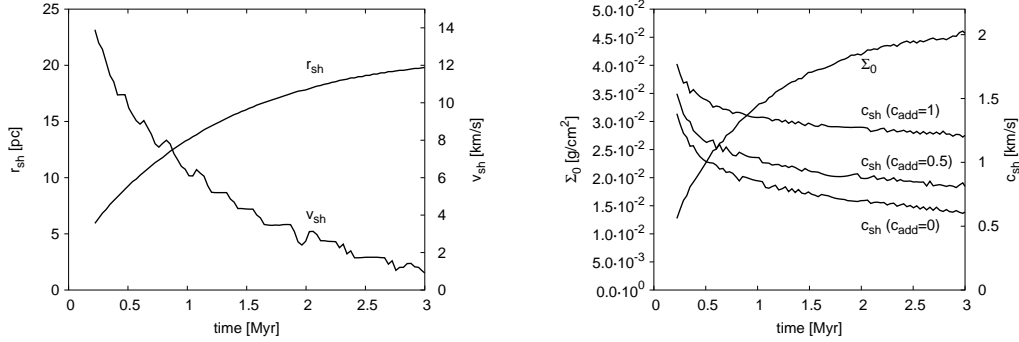


Figure 7.1: Properties of the the selected 1D simulation. Left: The evolution of radius r_{sh} and expansion velocity v_{sh} of the shell. Right: The evolution of surface density Σ_0 and sound-speed in the shell c_{sh} for various values of the additional pressure given by c_{add} .

of CPU time on a single 1.5 GHz processor, which seriously limits the number of models which can be computed.

The simulations which serve for a determination of the mass spectrum of fragments are independent and have been run in parallel on the 16-processor PC cluster of the AsÚ-Praha.

Nevertheless, the situation is getting better, since new faster processors are developed quickly. We also plan to prepare a parallel version of the numerical model, which may reduce the computational time by one order. A substantial speed-up may be also gained by using a more advanced hydrodynamic code, which supports the adaptive mesh refinement technique.

7.1 1D to 3D transition

At first, we prepare 1D simulations to compute an initial phase of the shell evolution and obtain the initial conditions for the 3D computations. In order to make the number of computed models small to spare the CPU time, we have to choose a particular set of parameters for which we will run the next 3D computations.

We may expect that the behaviour of the model in different scales would be qualitatively same for the following reasons: a) the purely hydrodynamic model is described by the self-similar solution and the change of scales has no effect; b) the solution with the gravity scales in a simple way, very similarly to the scaling of the gravitational instability (see Tab. 3.1); c) the situation with the radiative cooling is not so simple, but the main effect of the radiative

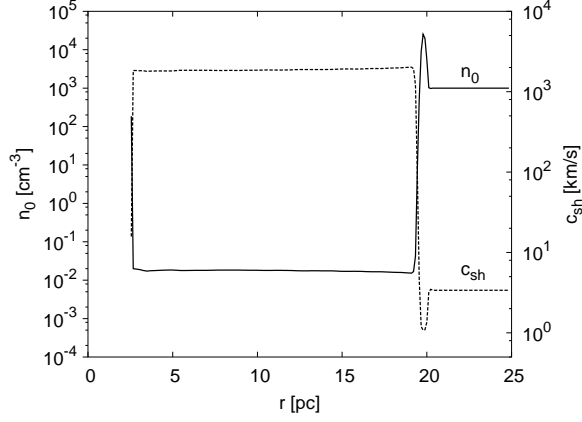


Figure 7.2: Radial profiles of particle density n_0 and sound-speed c_s in the selected 1D simulation.

cooling is the thermally collapsed thin shell, whose thickness is controlled by the artificial parameter c_{add} , anyway. The radiative cooling also causes the energy loss from the hole and decelerates the shell expansion, but we cannot expect that this process can qualitatively change the behaviour of the gravitational instability.

Therefore, we prepare models with relatively dense ambient medium and powerful energy source, which makes the gravitational instability time t_B short and perturbation growth rate high. The c_{add} parameter, which controls the additional pressure, should be chosen so that the sound-speed in the shell is as small as possible, but the shell is thick enough (5-7 zones) to be resolved (see Fig. 7.2). We try the values from the range 0 – 1 km/s. Parameters of the model are shown by the following table

$$\begin{array}{l|l} n_0 = 10^3 \text{ cm}^{-3} & E_{\text{flow}} = 5 \cdot 10^{51} \text{ erg/Myr} \\ \mu = 1.3 \text{ amu} & M_{\text{flow}} = 50 M_{\odot}/\text{Myr} \\ T_0 = 10^3 \text{ K} & c_{\text{add}} = 0.5 \text{ km/s} \end{array}$$

Fig. 7.1 shows the evolution of the shell radius, expansion velocity, surface density and the sound-speed in the shell for various values of c_{add} parameters (0, 0.5 and 1 km/s). For the next simulations we take $c_{\text{add}} = 0.5$ km/s which is enough to resolve the shell. It leads to the value of c_{sh} around 1 km/s which is a) physically reasonable value; b) small enough to relatively fast gravitational instability.

Radial profiles of the particle density and the sound-speed are shown by Fig 7.2. It illustrates the dip of the sound-speed in the dense thin shell.

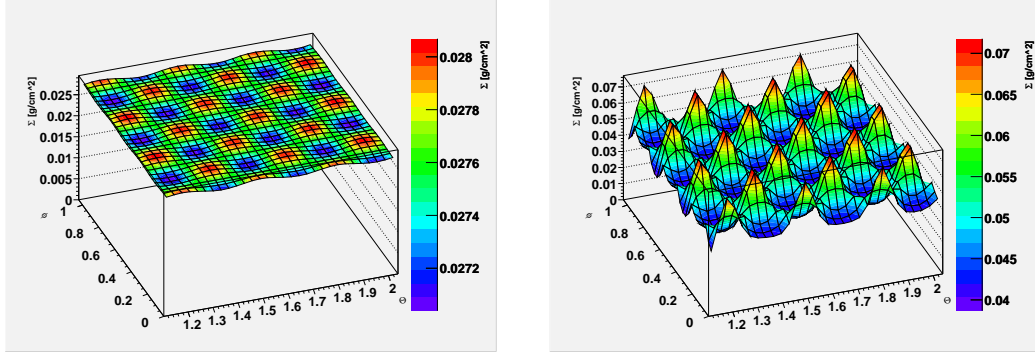


Figure 7.3: Left: The initial perturbation of the surface density is a single mode (the spherical harmonics Y_{18}^{27}). Right: The surface density at time $t = 3$ Myr, the perturbation amplitude is $0.48\Sigma_0$.

7.2 Perturbation growth in the linear regime

As the first test we try to model the growth of a single mode of initial perturbations and compare its growth rate to the one given by the linear analysis (Eq. 3.22).

The beginning of the gravitational instability t_b can be determined from the 1D simulation described in the previous section. The minimum sound-speed in the shell at time 0.5 – 1Myr (in this time interval we expect the beginning of the instability) is $c_{\text{sh}} \doteq 1\text{km/s}$. Using the Eq. 3.26 we obtain $t_b = 0.75\text{Myr}$. With a small safety factor, we start the 3D computation at time 0.7Myr.

At this time we perturb the density in the shell $\rho(r, \theta, \phi)$ using the formula

$$\rho(r, \theta, \phi) = 0.05\rho_{1\text{D}}(r)Y_m^l(\theta, \phi), \quad r \in (r_{\text{cd}}, r_{\text{sf}}), \quad (7.1)$$

where $\rho_{1\text{D}}$ is a density in the shell in 1D spherically symmetric simulation, r_{sh} and r_{cd} are radii of the shock-front and the contact discontinuity and $Y_m^l(\theta, \phi)$ is a spherical harmonic function. We take $l = 27$ and $m = 18$ which creates the mode of the wavenumber close to $\eta_{\text{max}}(t_b)$ given by the linear analysis (see Eq. 3.23), $\eta_{\text{max}}(t_b, \Sigma_0, r_{\text{sh}}, c_{\text{sh}}) = 18.5$ for the current simulation. The initial amplitude of this mode is 5%. We use the periodic boundary conditions at the axial borders.

Fig. 7.3, left panel, shows the distribution of the surface density on the shell surface at $t = t_b$ (initial perturbations), while the right panel of the figure shows the same quantity later (at $t = 3$ Myr) when the perturbations are evolved.

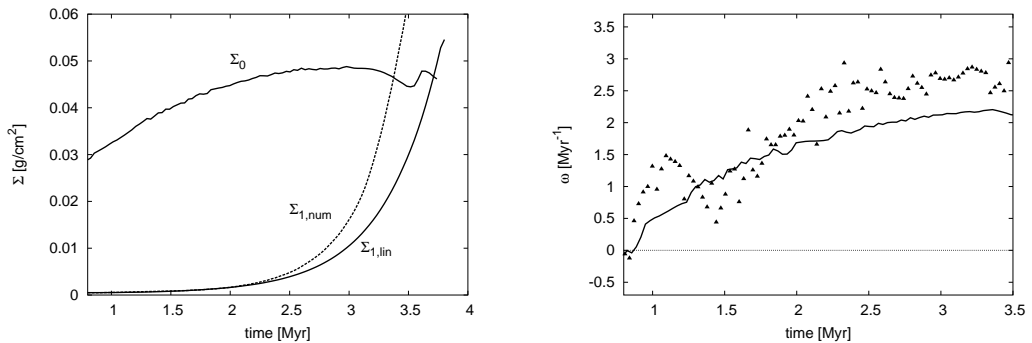


Figure 7.4: Left: The evolution of the perturbations in the numerical solution $\Sigma_{1,\text{num}}$ and in the linear analysis $\Sigma_{1,\text{lin}}$. Right: The perturbation growth rate in the numerical simulation $\omega_{\eta,\text{num}}$ (triangles) and in the linear analysis $\omega_{\eta,\text{lin}}$ (line).

Detecting the shell and integrating its mass we obtain the average surface density Σ_0 . The average sound-speed in the shell is computed as the density weighted average of $\sqrt{p/\rho}$ over the whole shell. Knowledge of these quantities enable us to determine the perturbation growth rate $\omega_{\eta,\text{lin}}(t)$ according to the linear analysis (Eq. 3.22). Using this value and inserting it to the equation

$$\frac{d\Sigma_{1,\text{lin}}}{dt} = \omega_{\eta,\text{lin}}(t)\Sigma_{1,\text{lin}} \quad (7.2)$$

we get the evolution of the perturbation amplitude $\Sigma_{1,\text{lin}}(t)$, which the linear analysis predicts for the shell with parameters given by the numerical model. This function can be compared to the perturbation amplitude in the simulation given by

$$\Sigma_{1,\text{num}}(t) = \frac{1}{2}(\Sigma_{\text{max}}(t) - \Sigma_{\text{min}}(t)) , \quad (7.3)$$

where Σ_{max} and Σ_{min} are the maximum and minimum surface densities in the shell at time t . Fig. 7.4, left panel, shows that both functions are in a good agreement. The perturbations in the numerical model grow a bit faster, but this is what we should expect. The main reason is that the linear analysis assumes the isothermal shell, while the sound-speed in the numerical simulation depends on the density. The sound-speed in the dense parts of the shell is smaller due to the more effective cooling, and it leads to the faster gravitational collapse of these parts. The value of $\Sigma_{1,\text{lin}}$ after $t = 3$ Myr is probably wrong, since the shell is so fragmented, that the algorithm which detects its borders fails, and the parameters r_{sh} , v_{sh} , c_{sh} and Σ_0 cannot be determined (as can be seen from the curve of Σ_0).

l	m	$t_{\text{frag,lin}}$	$t_{\text{frag,num}}$
18	12	4.10	3.73
22	15	3.92	3.53
27	18	3.72	3.38
32	21	3.57	3.28
36	24	3.44	3.26

Table 7.1: The fragmentation time in the numerical simulation $t_{\text{frag,num}}$ and in the linear analysis $t_{\text{frag,lin}}$ for several modes of initial perturbations.

Similarly, we can determine $\omega_{\eta,\text{num}}$ from the perturbation growth given by $\Sigma_{1,\text{num}}$ as

$$\omega_{\eta,\text{num}} = \frac{\frac{d}{dt}(\Sigma_{1,\text{num}})}{\Sigma_{1,\text{num}}} \quad (7.4)$$

and compare it to $\omega_{\eta,\text{lin}}$ from the linear analysis as suggested by Fig. 7.4, right panel. We can see that after relatively high growth rate in the beginning, which is connected to the initial relaxation of the inserted perturbation, the growth rate drops to the value slightly less than the value given by the linear analysis. Then, at $t \doteq 2$ Myr, it reaches the analytical rate and it is by approximately 30% higher for the rest of the simulation.

Experiments with other modes η are qualitatively very similar. Fragmentation times, defined as the time t_{frag} when $\Sigma_1(t_{\text{frag}}) = \Sigma_0$, in the numerical simulations and the analytical solutions are compared in Tab. 7.1.

We conclude that the linear analysis and the numerical experiments using the hydrodynamic code are in a good agreement. The perturbations grow slightly faster in the numerical solution, but it can be explained by the different treatment of the sound-speed in the shell. In the numerical simulation it decreases in the dense clumps reducing the pressure, which lead to the faster growth of perturbations. In the analytical solution, on the other hand, it is constant over the whole shell.

7.3 The mass spectrum of fragments

Having this optimistic results, we can do the next step and start to study the behaviour of the instability in a more realistic environment, where multiple different modes are present. In this situation, the modes compete with each other for the mass – the mode interaction takes effect.

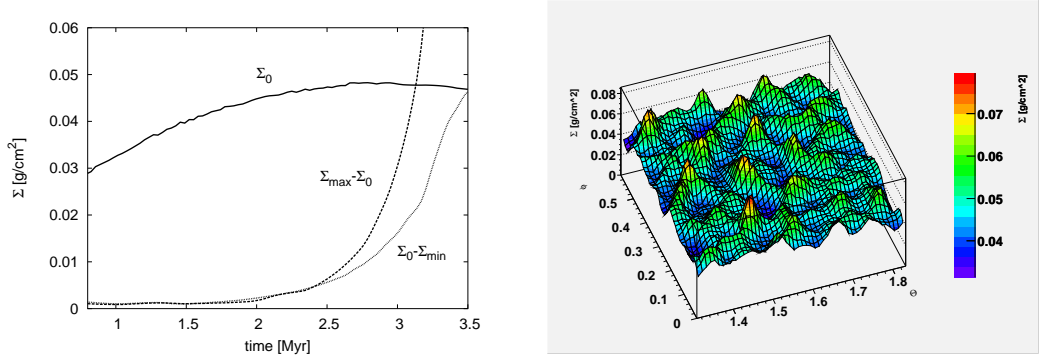


Figure 7.5: Left: evolution of the perturbation amplitude in the simulation with the random initial perturbations. Right: distribution of the surface density at $t = 3$ Myr in the same simulation.

Σ_{cut}	N_f	Σ_{cut}	N_f	Σ_{cut}	N_f	Σ_{cut}	N_f
0.045	60	0.050	230	0.053	274	0.056	242
0.046	70	0.051	251	0.0535	274	0.057	231
0.047	96	0.0515	271	0.054	268	0.058	226
0.048	137	0.052	272	0.0545	265	0.059	198
0.049	193	0.0525	263	0.055	259	0.060	167

Table 7.2: Number of fragments detected in the set of simulations with random initial conditions depending on the value of Σ_{cut} .

We setup the simulation with randomly distributed initial perturbations of the amplitude 5%. The size of the computational domain is $30^\circ \times 30^\circ$ in axial coordinates, the boundary conditions are periodic.

An evolution of the perturbation amplitude in such simulation is shown by Fig. 7.5, left panel; the right panel of this figure shows the distribution of the surface density in the computed part of shell after some evolution (at time $t = 3$ Myr). We can clearly see that some perturbations have grown such that their maximum surface density is comparable to the average (unperturbed) value $\Sigma_0 = 0.048 \text{ g cm}^{-2}$. These can be considered to be separate fragments.

Fig. 7.6, left panel, illustrates that the shell remains thin (5-7 zones) and its shape spherical during the whole evolution. This enables us to use the surface density for the identification and description of fragments.

We use the simplest approach and define a fragment in the shell surface as the compact area with the surface density higher than some limit Σ_{cut} . The question is what should be its value. A high value of Σ_{cut} causes that there would be less fragments and they would be too small. A low value, on

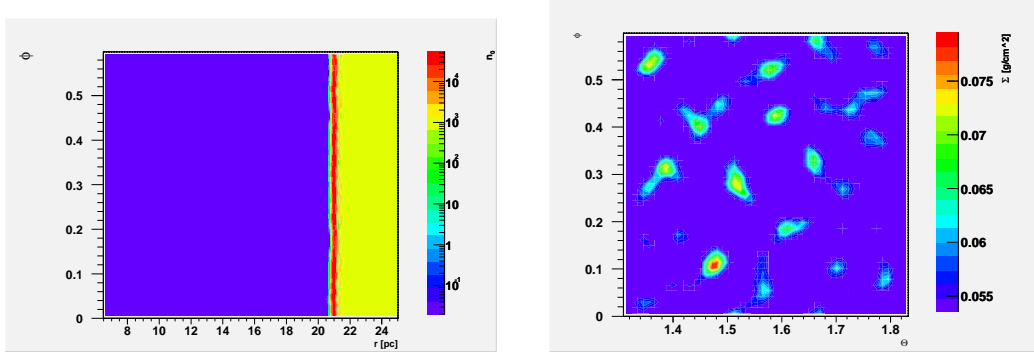


Figure 7.6: The simulation with random initial conditions. Left: distribution of the particle density in the computational domain at $\Theta = \pi/2$ at time $t = 3$ Myr. It illustrates that the shell remains thin and spherical in the later stage of its evolution. Right: distribution of the surface density in the shell at the same time. The minimum of the colour coding scale is set to $\Sigma_{\text{cut,max}}$ to highlight the detected fragments.

the other hand, would lead to merging of fragments – there would be also less fragments, but they would be too large. We need a value, for which the fragments are as large as possible, but they do not merge. Experiments show that it is well fulfilled for $\Sigma_{\text{cut,max}}$ for which the highest number of fragments is detected. In the following analysis we use this value. Nevertheless, we should check how the resulting spectrum depends on the value of Σ_{cut} .

We should also note that the size of fragments is limited by the resolution (for the small fragments) and by the size of the computational domain and the fact that the periodic boundary conditions were used (for the large fragments).

Fragments which consist of only one zone are eliminated from the following analysis, because they are rather random fluctuations than the "real" fragments. After that, we typically detect 20 - 30 fragments in one simulation. We need approximately ten times more fragments to form a reasonable mass spectrum, so we run eight simulations, which are identical, except the pseudorandom-number generator initialisation. Tab. 7.2 shows the number of fragments detected in such set of simulations depending on the value of Σ_{cut} , so we have $\Sigma_{\text{cut,max}} = 0.053 \text{ g cm}^{-2}$. The fragments detected using this $\Sigma_{\text{cut,max}}$ are shown by Fig. 7.6, right panel.

We determine the mass of individual fragments and split the mass range in several bins. Then we count the number of fragments in particular bins obtaining the mass spectrum suggested by Fig. 7.7, left panel. The mass spectrum index computed from the three most-right bins is

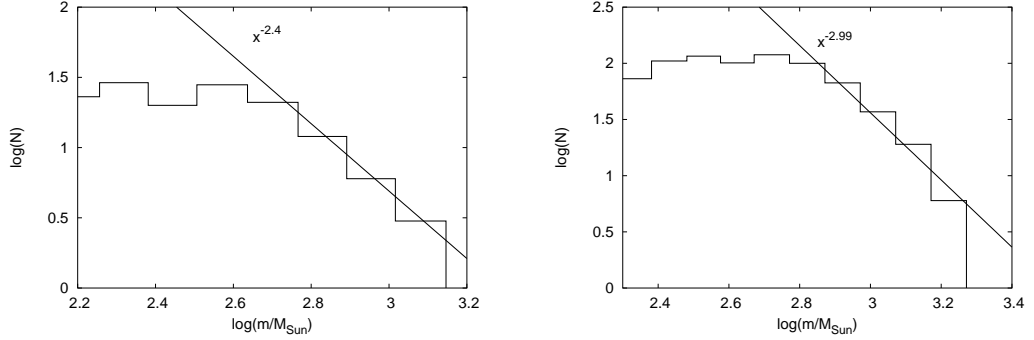


Figure 7.7: The mass spectrum of fragments. Left: Fragments were detected in 8 simulations with $30^\circ \times 30^\circ$ computational area. Right: Fragments were detected in 12 simulations with $60^\circ \times 60^\circ$ computational area.

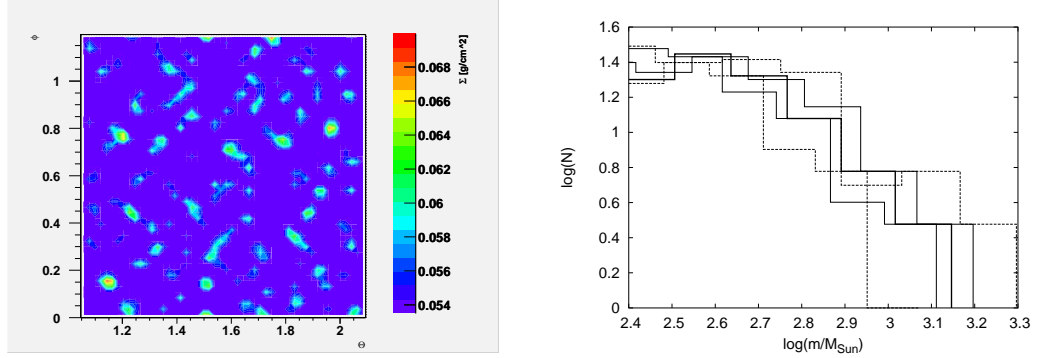


Figure 7.8: Left: The fragments detected in one of the simulations with $60^\circ \times 60^\circ$ computational area. Right: The mass spectra obtained using different values of Σ_{cut} .

$$\alpha = 2.4 \pm 0.1 . \quad (7.5)$$

Since the computational domain is only the part of the shell with periodic boundary conditions at its borders, the obtained mass spectrum may be cut artificially at its high mass end. Therefore we set up the simulation in the computational domain with a double size in each axial direction. It leads to the artificial cut at the low mass end of the mass spectrum, but it is not possible to cover whole mass range (more than 3 orders) of created fragments with the recent numerical model. We determine the $\Sigma_{\text{cut,max}}$ and obtain the mass spectrum suggested by Fig. 7.7, right panel. The mass spectrum index at the high mass end is

$$\alpha = 3.0 \pm 0.4 . \quad (7.6)$$

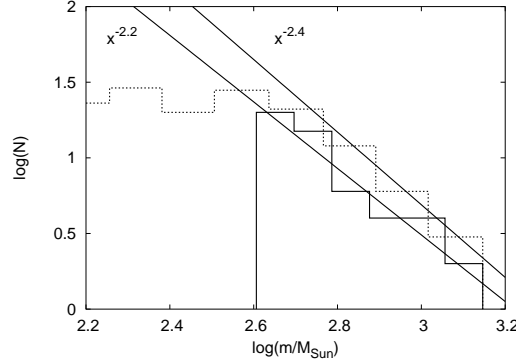


Figure 7.9: The mass spectrum of fragments with $m > M_J$ comparing to the mass spectrum of all detected fragments.

Fig. 7.8, left panel, shows detected fragments in one of such simulations.

The dependence of the mass spectrum slope on the Σ_{cut} value is suggested by Fig. 7.8. The mass spectrum indices for the considered Σ_{cut} values are

$\Sigma_{\text{cut}} [\text{g cm}^{-2}]$	0.052	0.0525	0.053	0.0535	0.054
α	0.8	2.6	2.4	2.4	3.8
$\Delta\alpha$	0.8	0.1	0.1	0.7	1.6

The values of α for $\Sigma_{\text{cut}} = 0.0525, 0.053, 0.0535 \text{ g cm}^{-2}$ are similar, around $\alpha = 2.5$. The high value of α for high $\Sigma_{\text{cut}} = 0.054 \text{ g cm}^{-2}$ is because we detect only the central parts of fragments and cut off the borders of fragments, which contains relatively more mass for the larger fragments than for the smaller ones. The flatter spectrum for $\Sigma_{\text{cut}} = 0.052 \text{ g cm}^{-2}$ is due to the merging of identified fragments – it decreases the number of small fragments in favour of large fragments (note, that it is the merging in the identification process, which has nothing to do with the physical merging of the fragments).

Finally, we check if the detected fragments are gravitationally bounded. We determine the average density ρ_{av} and temperature T_{av} of each fragment and compute the Jeans mass as follows

$$M_J = \rho_{\text{av}}^{-1/2} T_{\text{av}}^{3/2} \left(\frac{5k_B}{G\mu m_H} \right)^{3/2} \left(\frac{3}{4\pi} \right)^{1/2}, \quad (7.7)$$

where k_B is the Boltzmann constant.

In the set of 8 numerical simulations we have detected 274 fragments, 53 of them have $m > M_J$. Fig. 7.9, left panel, shows the mass spectrum made of such fragments comparing to the spectrum made of all fragments. We can see that this selection does not influence the slope of the spectrum, which is

$$\alpha = 2.2 \pm 0.3 , \quad (7.8)$$

which is close to the mass spectrum of all fragments given by Eq. 7.5. The only change is the cut-off at the low mass end, which is at the higher mass for the gravitationally bounded fragments – the low-mass fragments are usually not gravitationally bounded.

7.4 Conclusions

We have developed a 3D numerical model of the expanding self-gravitating shell based on the ZEUS hydrocode. It includes the cooling of the gas by radiation implemented as a cooling function depending on density, temperature and metallicity of the material. An effect of magnetic field and turbulence in the shell is treated as the artificial additional pressure.

The gravitational potential is computed by the code Šemík developed by us. It uses the multigrid method – one of the most efficient recent methods. This code is independent on the rest of the model, and can be used in different applications.

The numerical model was used to test the linear analysis of the gravitational instability of the expanding shell. Both the solutions are in good agreement. The numerical model predicts a bit faster growth of the gravitational instability, which can, however, be easily explained by the fact that the sound-speed in the shell is a dynamical quantity which depends on the density, while analytical solution assumes the isothermal shell.

The analytical and numerical models were used to obtain the mass spectrum of fragments generated by the gravitational instability. Both models predict that the expanding shell yields the mass spectrum with higher slope in the high-mass region than other physical models (which yield $\alpha = 2$). It may explain higher slope of the initial mass function of stars ($\alpha = 2.3$); the much flatter mass spectrum of Galactic molecular clouds ($\alpha = 1.5$) may be explained by their merging. The analytically and numerically obtained spectra are in quite a good agreement, although the accuracy of the numerical spectrum is limited by the resolution of the numerical simulations and the low number of fragments, which is caused by high CPU-costs of these simulations.

Future development of our model should consist of three main points. First of all, physical processes which have not yet been represented within the model should be taken into account. This concerns in particular the influence of magnetic field and microscopic processes such as evaporation. Furthermore, the numerical code has to be improved, e.g. by using AMR

(adaptive mesh refinement) or/and parallel hydrodynamic code. Finally, the model can be used in more complicated and realistic environments, which means using the non-homogeneous ambient medium, galactic differential rotation, etc.

The bibliography

- Bicknell, G., 2001, Lecture Notes, available at
<http://msowwww.anu.edu.au/~geoff/AFD/Sedov.pdf>
- Binney, J., Merrifield, M., 1998, in *Galactic Astronomy*, Princeton University Press, p. 600
- Binney, J., Tremaine, S., 1987, in *Galactic Dynamics*, Princeton University Press, p. 290
- Böhringer & Hensler, 1989, *A&A*, 215, 147
- Briggs, W. L., Henson, V. E., McCormick, S. F., 2000, *A Multigrid Tutorial*, SIAM, Philadelphia
- Brinks, E., Bajaja, E., 1986, *A&A*, 169, 14
- Castor, J., McCray, R., Weaver, R., 1975, *ApJ*, 200, L107
- Chandrasekhar, S., 1949, *ApJ*, 110, 329
- Chevalier, R. A., 1974, *ApJ*, 188, 501
- Chevalier, R. A., Blondin, J. M., 1995, *ApJ*, 444, 312
- Clarke, D. A., Norman, M. L., Fiedler, R. A., 1994, *ZEUS User manual*
- Colella, P., Woodward, P. R., 1984, *J. Comput. Phys.*, 54, 174
- Cox, D. P., Smith, B. W., *ApJ*, 189, L105
- Deul, E. R., den Hartog, R. H., 1990, *A&A*, 229, 362
- Efremov, Yu. N., Ehlerová, S., Palouš, J., 1999, *A&A*, 350, 457
- Ehlerová, S., Palouš, J., Theis, Ch., Hensler, G., 1997, *A&A*, 328, 121
- Ehlerová, S., 2000, PhD thesis, Charles University, Prague
- Ehlerová, S., Palouš, J., Huchtmeier, W. K., 2001, *A&A*, 374, 682
- Ehlerová, S., Palouš, J., 2003, *A&A*, submitted
- Elmegreen, B. G., 1994, *ApJ*, 427, 384
- Elmegreen, B. G., 1998, in the proceedings of the NASA Conference: "Origins of Galaxies, Stars, Planets and Life", eds. C. E. Woodward, H. A. Thronson, M. Shull, *ASP Conf. Ser.*, astro-ph/9712352
- Elmegreen, B. G., Shadmehri, 2002, astro-ph/0210246
- Falle, S. A. E. G., 1975, *MNRAS*, 172, 55
- Falle, S. A. E. G., 1981, *MNRAS*, 195, 1011
- Ferland, G. J., 2000, *RevMexAA*, 9, 153

- Ferland, G. J., Savin, D. W., 2003, Spectroscopic Challenges of Photoionized Plasmas, ASP Conference Series, vol. 247, edited by Gary Ferland and Daniel Wolf Savin
- Fuchs, B., 1996, MNRAS, 278, 985
- Godunov, S. K., 1959, Matematicheskii Sbornik, 47, 271
- Hartmann, D., Burton, W. B., 1997, Atlas of Galactic Neutral Hydrogen, Cambridge University Press
- Halwley, J. F., Smarr, L. L., Wilson, J. R., 1984, ApJ, 277, 296
- Heiles, C., 1979, ApJ, 229, 533
- Heiles, C., 1984, ApJS, 55, 585
- Heiles, C., 1990, ApJ, 354, 483
- Jungwierth, B., Palouš, J., 1994, A&A, 187, 55
- Kafatos, M., 1973, ApJ, 182, 433
- Kamphuis, J., Sancisi, R., van der Hulst, J. M., 1991, A&A, 244, L29
- Kim, S., Staveley-Smith, L., Dopita, M. A., Freeman, K. C., Sault, R. J., Kesteven, M. J., McConnel, D., 1998, ApJ, 503, 674
- Klessen, R. S., 2003, to appear in Reviews of Modern Astronomy, Vol. 16, arXiv:astro-ph/0301381
- Kroupa, P., 2001, MNRAS, 322, 231
- MacDonald, J., Bailey, M. E., 1981, MNRAS, 197, 995
- Mac Low, M.-M., McCray, R., 1988, ApJ, 324, 776
- Mac Low, M.-M., McCray, R. A., Norman, M. L., 1989, ApJ, 337, 141
- Mac Low, M.-M., Norman, M. L., 1993, ApJ, 407, 207
- McClure-Griffiths, N. M., Dickey, J. M., Gaensler, B. M., Green, A. J., 2002, ApJ, 578, 176
- McKee, C. F., Ostriker, J. P., 1977, ApJ, 218, 148
- Menon, T. K., 1958, ApJ, 127, 28
- Mönchmeyer, R., Müller, E., 1989, A&A, 217, 351
- Mueller, M. W., Arnett, W. D., 1976, ApJ, 210, 670
- Norman, M. L., Stone, J. M., 1994, ZEUS2D
- Norman, M. L., Winkler, K.-H., 1986, in Astrophysical Radiation Hydrodynamics, ed. K.-H. Winkler & M. L. Norman, Dordrecht: Reidel, p. 187
- Palouš, J., Franco, J., Tenorio-Tagle, G., 1990, A&A, 227, 175
- Palouš, J., 1990, in The Interstellar Disc-Halo Connection in Galaxies, ed. H. Bloemen, Sterrewacht, Leiden, p. 101
- Palouš, J., 1992, in Evolution of Interstellar matter and Dynamics of Galaxies, eds. J. Palouš, W. B. Burton, and P. O. Lindblad, Cambridge University Press, p. 177
- Palouš, J., Wünsch, R., Ehlerová, S., MNRAS, 2003, submitted

- Press, W. H., Teukolsky, S. A., Vetterling, W. T., Flannery, B. P., 1992, in Numerical Recipes in C, Cambridge University Press, Chapter 9.3
- Puche, D., Westpfahl, D., Brinks, E., Roy, J.-R., 1992, *AJ*, 103, 1841
- Różyczka, M., 1985, *A&A*, 143, 59
- Sedov, L. I., 1959, in *Similarity and Dimensional Methods in Mechanics*, Academic Press, New York
- Sedov, L. I., 1972, in *Metody Podobija i Razmernosti v Mehanike*, Nauka, Moscow
- Silich, S. A., Franco, J., Palouš, J., Tenorio-Tagle, G., 1996, *ApJ*, 468, 722
- Shapiro, P. R., Moore, R. T., 1976, *ApJ*, 207, 460
- Shore, S. N., 1992, *An Introduction to Astrophysical Hydrodynamics*, Academic Press, San Diego
- Stanimirovic, S., Staveley-Smith, L., Dickey, J. M., Sault, r. J., Snowden S. L., 1999, *MNRAS*, 302, 417
- Stone, J. M., Norman, M. L., 1992a, *ApJS*, 80, 753
- Stone, J. M., Norman, M. L., 1992b, *ApJS*, 80, 791
- Stone, J. M., Norman, M. L., 1992c, *ApJS*, 80, 819
- Straka, W. C., 1974, *ApJ*, 190, 59
- Tan, J. C., 2000, *ApJ*, 536, 173
- Tenorio-Tagle, G., Bodenheimer, P., 1988, *Ann. Rev. A&A*, 26, 145
- Tenorio-Tagle, G., Franco, J., Bodenheimer, P., Różyczka, M., 1987, *A&A*, 179, 219
- Tenorio-Tagle, G., Palouš, J., 1987, *A&A*, 186, 267
- Tomisaka, K., Ikeuchi, S., 1986, *PASJ*, 38, 697
- van der Hulst, J. M., 1996, in *ASP Conf. Ser. Vol. 106: The Minnesota Lectures on Extragalactic Neutral Hydrogen*, ed. E. D. Skillman, ASP, San Francisco, p. 47
- van Leer, B., 1977, *J. Comput. Phys.*, 23, 276
- Vishniac, E. T., 1983, *ApJ*, 274, 152
- von Neumann, J., Richtmyer, R. D., 1950, *J. Appl. Phys.*, 21, 232
- Weaver, H. F., Williams, D. R., 1973, *A&A Suppl.*, 8, 1
- Weaver, R., McCray, R., Castor, J., Shapiro, P., Moore, R., 1977, *ApJ*, 218, 377
- Wilcots, E. M., Miller, B. W., 1998, *AJ*, 116, 2363
- Whitworth, A. P., Francis, N., 2002, *MNRAS*, 329, 641
- Wünsch, R., Palouš, J., 2001, *A&A*, 374, 746